

May 2021

High Density Cement-Rock Interface Characterization

zahid farid

Follow this and additional works at: https://digitalcommons.lsu.edu/gradschool_theses



Part of the [Engineering Commons](#)

Recommended Citation

farid, zahid, "High Density Cement-Rock Interface Characterization" (2021). *LSU Master's Theses*. 5346.
https://digitalcommons.lsu.edu/gradschool_theses/5346

This Thesis is brought to you for free and open access by the Graduate School at LSU Digital Commons. It has been accepted for inclusion in LSU Master's Theses by an authorized graduate school editor of LSU Digital Commons. For more information, please contact gradetd@lsu.edu.

HIGH DENSITY CEMENT-ROCK INTERFACE CHARACTERIZATION

A Thesis

Submitted to the Graduate Faculty of the
Louisiana State University and
Agricultural and Mechanical College
in partial fulfillment of the
requirements for the degree of
Master of Science

in

The Craft and Hawkins Department of Petroleum Engineering

by
Zahid Ullah Farid
BS., Ghulam Ishaq Khan Institute of Science and Technology, 2015
August 2021

Acknowledgements

I would like to thank my advisor Dr. Ipsita Gupta for her guidance, motivation, mentorship, and supervision throughout the course of this study.

I am grateful for the help and assistance of my colleagues late Hope Asala and Cory Lautenschlager, as well as the Geofluids Modeling Group (GMG), led by Dr. Gupta.

Acknowledgments go out to the NASEM Gulf Research Program for sponsoring part of this work.

I would like to extend my gratitude towards Dr. Roderick Pernites and Mr. Jordan Clark at the BJ Services (Baker Hughes) for their time, providing the high-density cement samples and the research lab facility used in this thesis project.

I express my deepest appreciation to Dr. Dongmei Cao and Dr. Yang Mu at the LSU Shared Instrumentation Facility (SIF) for providing training on the Scanning Electron Microscope (SEM) and microhardness testing.

I gratefully acknowledge Mr. Jeremy Icenogle at the Louisiana Transportation Research Center, for his help with the Semi-Circular Bend test apparatus used to generate load-displacement curves.

I want to thank my committee members, Dr. Seung I. Kam and Dr. Yuanhang Chen, for their time and valuable feedback on this study.

Finally, I would like to thank my family and friends for their support and encouragement during my time at LSU.

Table of Contents

ACKNOWLEDGEMENTS	I
LIST OF TABLES	III
LIST OF FIGURES	V
ABSTRACT	IX
1. INTRODUCTION	1
1.1. PROBLEM STATEMENT	1
1.2. RESEARCH GOALS AND OBJECTIVES	3
2. BACKGROUND AND LITERATURE REVIEW	5
2.1. SHALE	6
2.2. PORTLAND CEMENT	11
2.3. SANDSTONE	21
2.4. LIMESTONE	23
2.5. CEMENT-ROCK INTERFACE IN THE WELLBORE	24
3. METHODOLOGY	27
3.1. PREPARING AND CURING CEMENT TO ROCK INTERFACES	27
3.2. SEMI CIRCULAR BEND TEST (SCBT) FOR MECHANICAL TESTING	30
3.3. ANALYZING THE CEMENT-ROCK INTERFACE USING SEM	33
3.4. HARDNESS TEST	45
4. RESULTS AND DISCUSSION	51
4.1. SCBT FOR FRACTURE TOUGHNESS CHARACTERIZATION	51
4.2. SEM IMAGES AND ANALYSIS	53
4.3. MICROHARNDNESS	95
4.4. DISCUSSION	103
5. CONCLUSION	104
REFERENCES	107
VITA	115

List of Tables

Table 2. 1. Mineralogical composition of shale and their general formula (Bregaya et al., 2013; Drever, 1982; Hussain et al., 1996; Yu et al., 2017)	7
Table 2. 2. Cement constituents and composition (Bentz et al., 2000; Lea. 1970; Taylor, 1989, 1997)	12
Table 2. 3. Hydrated cement products	13
Table 2. 4. The eight API groups of cement and their general percentage composition (Nelson, 1990).....	14
Table 2. 5. Use of cement classes as specified by API (Habrata et al., 1980; Raczkowski et al., 1978).....	15
Table 2. 6. The major cement constituents, their attributes and their hydration equation.....	18
Table 3. 1. The geometrical shape of the indenters and the indent as well as the range of applied loads for the different types of hardness testing methods.	46
Table 4. 1. Fracture toughness of bi-material samples	51
Table 4. 2. Mineralogical composition, total organic content and porosity percentage of two different kinds of shale from previous studies (Bourg, 2015; Amann et al., 2013; Bai et al., 2013; Busch et al., 2008; Chalmers et al., 2012; Josh et al., 2012; Swift et al., 2014; Nelson, 2009)	59
Table 4. 3. Cement Sandstone sample 1 Vickers microhardness values	98
Table 4. 4. Cement Sandstone sample 1 Vickers indent dimensions on sandstone and corresponding hardness value	98
Table 4. 5. Cement Sandstone sample 1 Vickers indent dimensions on cement and corresponding hardness value	98
Table 4. 6. Cement Sandstone sample 1 Vickers indent dimensions on interface and corresponding hardness value	98
Table 4. 7. Cement Sandstone sample 2 Vickers microhardness values	99

Table 4. 8. Cement Sandstone sample 2 Vickers indent dimensions on sandstone and corresponding hardness value	99
Table 4. 9. Cement Sandstone sample 2 Vickers indent dimensions on cement and corresponding hardness value	99
Table 4. 10. Cement Sandstone sample 2 Vickers indent dimensions on interface and corresponding hardness value	99
Table 4. 11. Cement Shale sample 1 Vickers microhardness values.....	100
Table 4. 12. Cement Shale sample 1 Vickers indent dimensions on shale and corresponding hardness value	100
Table 4. 13. Cement Shale sample 1 Vickers indent dimensions on cement and corresponding hardness value	100
Table 4. 14. Cement Shale sample 2 Vickers microhardness values.....	100
Table 4. 15. Cement Shale sample 2 Vickers indent dimensions on shale and corresponding hardness value	101
Table 4. 16. Cement Shale sample 2 Vickers indent dimensions on cement and corresponding hardness value	101
Table 4. 17. Cement Limestone sample 1 Vickers microhardness values.....	101
Table 4. 18. Cement Limestone sample 1 Vickers indent dimensions on limestone and corresponding hardness value	101
Table 4. 19. Cement Limestone sample 1 Vickers indent dimensions on cement and corresponding hardness value	102
Table 4. 20. Cement Limestone sample 2 Vickers microhardness values.....	102
Table 4. 21. Cement Limestone sample 2 Vickers indent dimensions on limestone and corresponding hardness value	102
Table 4. 22. Cement Limestone sample 2 Vickers indent dimensions on cement and corresponding hardness value	102

List of Figures

Figure 2. 1. Tetrahedron and Octahedron building blocks and layer structure in clay minerals (Figures redrawn from Nelson, 2015).....	9
Figure 2. 2. Diagram of three clay structures. a. (T-O) 1:1 layer (kaolinite) b. (T-O-T) 2:1 layer non-expandable (illite) c. (T-O-T) 2:1 layer expandable (smectite). (Figures redraw from Mitchel, 1993).....	10
Figure 2. 3. The different stages of hydration process (Zhang et al., 2005)	18
Figure 2. 4. Drawing of microstructure showing four elements of sandstone. Redrawn from Selley (2000).....	21
Figure 2. 5. Microstructure showing two different kinds of quartz grains. M is monocrystalline quartz. P is polycrystalline quartz (source: Geological Digressions)	22
Figure 3. 1. Semicircular custom-made brass molds	28
Figure 3. 2. Cement slurry with quarter rock samples in brass molds.....	28
Figure 3. 3. Cured bi-material samples a) b) c) d) before fracture e) f) cement-rock interface....	29
Figure 3. 4. Semi-Circular Bend custom made rig with compressive loading frame.....	31
Figure 3. 5. Three-point bend semi-circular bend test apparatus connected with laptop to generate load-displacement curves, and rig set up.....	31
Figure 3. 6. SCBT schematic loading arrangement and specimen geometry	33
Figure 3. 7. Equipment used in sample preparation a) Diamond bandsaw for cutting samples in thin sections b) Oven to dry the samples before SEM analysis c) Sputter Coater to coat the sample with conductive layer. d) Stub with a sample attached using carbon conductive tape.....	35
Figure 3. 8. Scanning Electron Microscope used to obtain micrographs in this study.....	36
Figure 3. 9. Schematic diagram of SEM showing all its components	37
Figure 3. 10. Approximate scale of spatial resolution for SE, BSE and X-rays in SEM.....	41

Figure 3. 11. Electron from the source removes an electron from the shell K of silicon atom. The created vacancy is filled by an electron from shell L, as a result, silicon Ka X-ray is produced. The difference between the K and L shell ionization energies is the energy of the X-ray generated.....	42
Figure 3. 12. Distribution map is put together for three elements (i.e., silicon, iron and aluminum) in a three-band image to distinguish the distinct phases mapped in the significant area.....	44
Figure 3. 13. Distribution map can be put together for three elements (i.e., silicon, iron and aluminum) in a three-band image. Primary colors are generated where distinct mixture of elements is present in the sample in distinct phases	45
Figure 3. 14. Micro-hardness specimen a) before epoxy resin b) after epoxy curing	48
Figure 3. 15. Equipment used in micro-hardness testing a) Grinder and polisher b) Micro-hardness tester	49
Figure 4. 1. Load-displacement curve for bi-material a) cement-sandstone b) cement-shale c) cement-limestone	52
Figure 4. 2. Pure cement a) Live map of pure cement at 2000x magnification obtained using FEI Quanta 3D FEG dual beam FIB/SEM at 20 kV b) Backscattered Electrons (BSE) micrograph at 2000x magnification c) EDS elemental map d) Distribution maps of fundamental elements	55
Figure 4. 3. Ca dominant phase in cement a) SEM EDS elemental spectrum b) quantification results	56
Figure 4. 4. Ca, Si and O dominant phase in cement a) SEM EDS elemental spectrum b) quantification results	57
Figure 4. 5. BSE micrographs of cement obtained at a) 500x b) 2000 x c) 5000x (d) 35000x magnification. The short networked fibrous structure of C-S-H and needle like structure of ettringite can be seen at different resolutions. IE is Iron Ettringite. CH is Portlandite. R is residual cement	58
Figure 4. 6. Pure shale a) Live map at 2000x magnification obtained using FEI Quanta 3D FEG dual beam FIB/SEM at 20 kV b) Backscattered Electrons (BSE) micrograph at 2000x magnification c) EDS elemental map d) Distribution maps of fundamental elements.....	62
Figure 4. 7. Ca, Mg, O and Si dominant phase in shale a) SEM EDS elemental spectrum b) quantification results	63

Figure 4. 8. Si, O and Al dominant phase in shale a) SEM EDS elemental spectrum b) quantification results	64
Figure 4. 9. Si, Al, K and O dominant phase in shale a) SEM EDS elemental spectrum b) quantification results	65
Figure 4. 10. SEM BSE image of pure shale at 2000x magnification. I is Illite (phyllosilicates i.e., clays). KF is K-Feldspar (tectosilicates). D is Dolomite. Q is quartz.....	66
Figure 4. 11. Pure Limestone a) Live map at 2000x magnification obtained using FEI Quanta 3D FEG dual beam FIB/SEM at 20 kV b) Backscattered Electrons (BSE) micrograph at 2000x magnification c) EDS elemental map d) Distribution maps of fundamental elements.....	67
Figure 4. 12. Ca and O dominant phase in limestone (a) SEM EDS elemental spectrum (b) quantification results	68
Figure 4. 13. SEM BSE image of pure limestone at 2000x magnification. SO is silicon oxide. CCO is calcium carbonate. There are traces of potassium oxide	69
Figure 4. 14. Pure Sandstone a) Live map at 2000x magnification obtained using FEI Quanta 3D FEG dual beam FIB/SEM at 20 kV b) Backscattered Electrons (BSE) micrograph at 2000x magnification c) EDS elemental map d) Distribution maps of fundamental elements.....	72
Figure 4. 15. Si, and O dominant phase in sandstone a) SEM EDS elemental spectrum b) quantification results	72
Figure 4. 16. Si, O and Al dominant phase in sandstone a) SEM EDS elemental spectrum b) quantification results	73
Figure 4. 17. SEM BSE image of pure sandstone at 2000x magnification. Pr is pyrite. K is K-feldspar. Q is Quartz. P is plagioclases. Kl is Kaolinite. C is Calcite. Traces of Zirconia also identified.....	74
Figure 4. 18. Cement-Limestone a) Live map at 2000x magnification obtained using FEI Quanta 3D FEG dual beam FIB/SEM at 20 kV b) Backscattered Electrons BSE micrograph at 2000x magnification c) EDS elemental map d) Distribution maps of fundamental elements..	78
Figure 4. 19. Ca, Si, O, S and Al dominant phase in cement-limestone interface a) SEM EDS elemental spectrum b) quantification results	79
Figure 4. 20. Ca and O dominant phase in cement-limestone interface a) SEM EDS elemental spectrum b) quantification results	80

Figure 4. 21. BSE SEM image of cement-limestone interface at 2000x magnification. E is Ettringite. CCO is Calcium Carbonate. R is Residual cement.....	80
Figure 4. 22. Cement-Sandstone a) Live map at 2000x magnification obtained using FEI Quanta 3D FEG dual beam FIB/SEM at 20 kV b) Backscattered Electrons (BSE) micrograph at 2000x magnification c) EDS elemental map d) Distribution maps of fundamental elements..	83
Figure 4. 23. Si, Al, O and Na dominant phase in cement-sandstone interface a) SEM EDS elemental spectrum b) quantification results	84
Figure 4. 24. Si, Al and O dominant phase in cement-sandstone interface a) SEM EDS elemental spectrum b) quantification results	85
Figure 4. 25. Si and O dominant phase in cement-sandstone interface a) SEM EDS elemental spectrum b) quantification results	86
Figure 4. 26. Ca, Si and O dominant phase in cement-sandstone interface a) SEM EDS elemental spectrum b) quantification results	87
Figure 4. 27. SEM BSE micrograph at a) 500x b) 2000x c) 2000x d) 10000x magnification. E is Ettringite. Q is Quartz. CSH. K is K-feldspar. Pl is Plagioclases.....	88
Figure 4. 28. Cement-Shale a) Live map at 2000x magnification obtained using FEI Quanta 3D FEG dual beam FIB/SEM at 20 kV b) Backscattered Electrons (BSE) micrograph at 2000x magnification c) EDS elemental map d) Distribution maps of fundamental elements.....	91
Figure 4. 29. Si, Al, O and K dominant phase in cement-shale interface a) SEM EDS elemental spectrum b) quantification results	92
Figure 4. 30. Ca, O, Si and Mg dominant phase in cement-shale interface a) SEM EDS elemental spectrum b) quantification results	93
Figure 4. 31. Si, Ca and O dominant phase in cement-shale interface a) SEM EDS elemental spectrum b) quantification results	94
Figure 4. 32. SEM BSE image of cement-shale interface at a) 250x b) 2000x magnification. D is Dolomite. Q is quartz. K is K-Feldspar.....	95

ABSTRACT

The strength and stability of a well depends primarily on the seal that is created between a geologic formation and a wellbore cement. To protect and maintain this well integrity during production and after well abandonment, fixed seals are installed in the wellbore. For this purpose, Portland cement of class H and G are used throughout the world as a plugging and sealing material for offshore oil and gas wells. The cement-rock interface is an area of vulnerability with a pathway that provides possible routes for leakage out into the wellbore environment and in proximity of the seals. Therefore, this plugging and abandonment process entails the need for understanding the bonding between subsurface rocks and cement.

The goal of this research work was to investigate and study the interface between high density class H cement and three different rock formations (sandstone, limestone and shale) and the effect of mineralogical composition on the interfacial bonding. In order to analyze the influence of the different lithologies and formation rocks' microstructure on wellbore cement–rock bonding, semi-circular bend test (SCBT) experiments were performed, indentation tests at μm scale were conducted and scanning electron microscopy (SEM) X-ray technique was used to map chemical and mineralogical compositions of the cement, rock and their interface. Microphotographs of the bi-material samples, prepared by curing cement to formation rock under high pressure and temperature, taken via back scattered electron and secondary electron modes helped in estimating the spatial chemical element distribution and microstructural properties of the samples.

Results from this study indicated 1) Cement-sandstone interface had the highest hardness values while cement-limestone interfacial zone showed ductile characteristics. The interface for both these bi-material samples were clearly visible under low resolution SEM images. 2) The cement-shale interface was brittle in nature and the boundary between the two composites was

indistinct in low resolution SEM images. 3. Cement-sandstone bi-material had the highest fracture toughness. Significant contrast was observed in the fracture toughness of cement-shale samples while the cement-limestone heterogenous material had fracture toughness lower than cement-sandstone but within the wide range of cement-shale fracture toughness.

This research work intends to fill the current research gap in the field by identifying any similarities or differences amongst the bonded bi-material samples studied for improved understanding of rock-cement interfaces using a combination of SCBT, SEM and indentation technique to monitor the interdependence of geochemical and geomechanical variations and microstructure characterization

1. INTRODUCTION

1.1. PROBLEM STATEMENT

When a well has produced to its full capacity and is considered to have reached its end of life, it becomes essential for it to be permanently plugged before it is abandoned. This process is generally comprised of installing numerous cement plugs inside the wellbore, in order to sequester the reservoir and other fluid-bearing formations from the wellbore (Vralstad et al., 2019). To permanently plug and abandon the wells has been a significant subject matter for many years, but due to a presence of many mature offshore wells in regions like the Gulf of Mexico and the North Sea, this focus has increased immensely in recent years.

An important aspect of plugging and abandonment (P&A) is the protection of well integrity after abandonment. In earlier years, regulations that described P&A processes were inadequate and vague, and thus, not enough attention was placed on ensuring proper well plugging (NPC, 2011). This has caused several old, plugged wells to leak after abandonment (Kaiser, 2017; Vielstädte et al., 2015; Watson et al., 2009). The 2010 BP Macondo accident and other succeeding critical oil spills like Little Buffalo oil spill and Northeast Brazil oil spill have pushed the petroleum industry in recent years towards making a few important modifications in their approach towards P&A through the new developments in technology and regulatory regimes (Smith et al., 2013). The main priority of P&A operations, in addition to cost efficiency, is now to impede ecological problems which includes preventing leakages.

In offshore settings, Portland cement class H and G of the American Petroleum Institute (API) is a frequently utilized plugging material (Vralstad et al., 2019). Cement is a product created by heating lime, alumina, silica and iron oxide in a kiln at high temperatures (Hewlett, 2003; Taylor, 1997; Lea, 1970). This amalgam contains four essential compounds: tricalcium silicate

(Ca_3SiO_5), tricalcium aluminate ($\text{Ca}_3\text{Al}_2\text{O}_6$), dicalcium silicate (Ca_2SiO_4), and tetra calcium aluminoferrite ($\text{Ca}_4\text{Al}_2\text{Fe}_2\text{O}_{10}$) (Taylor, 1997). The resulting product is incorporated with additives during the production of cement in order to enhance certain characteristics such as eco-friendly, lower price and more reliable setting (Carragher et al., 2018; Broni-Bediako et al., 2016). These additives are widely categorized into retarders, accelerators, extenders, dispersants, weighing agents, lost-circulation control agents, fluid-loss control agents, and special additives (Nelson, 1990).

When considering the process of plugging and abandonment, an important consideration for the subsurface is the interactivity between formation and cement. Understanding the chemical process of bonding to subsurface formations is critical for the evaluation and enhancement of cement performance in plugged and abandoned wells. An inadequate cement bond with the formation rock causes a zone of weakness at the interface leading to failure of the cement sheath, resulting in poor zonal isolation which is hazardous to the environment (Labus et al., 2016). Debonding is caused by several mechanisms, such as mechanical loads due to variable in-situ stresses, thermal stresses caused by thermal cycling (Lavrov et al., 2013), shrinkage during cement curing, or by inefficient mud removal during plug placement, or through a combination of both (Vralstad et al., 2019). With a few exceptions, comprehensive investigations of rock–cement interactions are scarce (Walsh et al., 2013). One example is the cement–rock–casing interaction studied on samples collected from a CO_2 injection well in the United States (Carey, 2007). In oil well P&A, interfaces between cement-rock-casing are a typical frail zone. Investigations into the cement bonding to a sandstone wall confirmed that a near-wall zone or interfacial transition zone grows along the cement-wall interface which eventually leads to debonding and fracturing (Torsæter et al., 2015).

The Scanning Electron Microscope (SEM) X-ray is an experimental tool used to determine the composition of the constituents of a cement (Bentz et al., 2000). As the technology of the electron microscope is advancing, the usefulness of the SEM is being recognized more and more (Wagner et al., 1993). The SEM generates an electron beam and focuses it over a specimen surface which then strikes it and produces signals detected as backscattered electrons (BSE) followed by secondary electrons (SE) and finally as X-rays. These signals help in estimating the spatial chemical element distribution and microstructural properties of the samples being tested. SEM X-Ray is a better technique than BSE or SE to determine the constituents in the sample because the results are more precise, reason being, the evaluation and measurements using this method is conducted from the mineral constituents itself (Bentz et al., 2000; Bentz et al., 1994; Taylor, 1989).

A significant amount of work is present in literature on the casing interface; however, the cement-rock interface is an aspect which has not been very commonly addressed in such interface studies. This calls for a need to investigate the effects of rock types and mineralogical composition on cement-rock interfacial bonding. This study aims to fill the current research gap in the field by using analytical techniques like scanning electron microscope to understand the interaction between plugging cement (provided by a service company, the chemical composition of which is not disclosed at this time) and three main formation rock types, such as sandstone, shale and limestone.

1.2. RESEARCH GOALS AND OBJECTIVES

The main goal of this research work is to investigate the interface between high density plugging cement and formation rocks. The research objectives are:

- a) To cure cement to rock under high temperature and pressure conditions;
- b) To map the chemical and mineralogical compositions of the cement and rock and their interface using SEM;

- c) To compare the mechanical property i.e., fracture toughness and micro-hardness, of the three different bonded bi-material samples; and
- d) To delineate any differences or similarities amongst the samples studied for improved understanding of rock-cement interfaces.

2. BACKGROUND AND LITERATURE REVIEW

Various studies have been done on different subsurface rocks that come in contact with the wellbore cement, namely siltstone (Fischer et al., 2013), basalt (Jung et al., 2013 and 2014), clay-rich argillite (Gherardi et al., 2013), granite (Soler et al., 2010), limestone (Duguid et al., 2010; Gherardi et al., 2012), shale and sandstone (Carroll et al., 2011). Reaction of carbon dioxide (CO_2) with cement-rock, at reservoir pressure and temperature, significantly alters the solution composition (Carroll et al., 2011). Wellbores, susceptible to CO_2 exposure lasting more than 30 years, lack stability. Therefore, the most important problem affecting the performance of a wellbore system in a CO_2 -sequestered reservoir is the casing–cement and cement–rock interface (Carey et al., 2007). While cement–sandstone reactions typically experience iron and amorphous silica precipitation, variations in shale structures in presence of CO_2 -rich brines are almost negligible (Carroll et al., 2011). However, studies show that alterations in cement by CO_2 and CO_2 -saturated water usually take place along the steel–cement and cement–rock (basalt) interfaces (Jung et al., 2013 and 2014). This signifies the vulnerability of the cement–host rock/steel casing interface to a CO_2 attack in a wellbore environment. Hence, additional investigation of cement degradation along such interfaces is critical.

Understanding the effect of the interfacial transition zone (ITZ) on the well cement stability can help identify the dependence of the bonding and fracturing of cement on the curvature of the rock-cement interface (Torsaeter, 2015). Autoclave reactor experiments help distinguish the textural and mineralogical alterations in the cement–rock. Rock and wellbore cement samples, both, react with and in presence of CO_2 -saturated brine (Labus et al., 2016 and Lorek et al., 2016) indicating the dependency of cement–rock interface performance on the rock lithology. Evidence of processes such as corrosion and dissolution are observed in most of the examined samples which

intensify over time, with anhydrite, gypsum, and calcite being the most vulnerable minerals to dissolution. Computer modeling is another method to understand reaction products that modify the interfaces between cement and rock. Studies show the presence of a highly carbonated and compacted layer within shale causing the occurrence of cement-shale separation. Furthermore, anhydrite dissolution has been identified in experimental studies to be the most important reaction observed in a cement-anhydrite interface. Higher porosity increases the susceptibility to mineral dissolution in a cement-rock interface. Experimental work into physical properties such as tensile and shear bond strength of rock-cement plugs indicate that under, both, direct tension and unconfined compression, structural failures occur in the rock-part rather than the cement-part or the interface itself (Cerasi, 2015).

2.1. SHALE

There are several types of sedimentary rocks including sandstone, limestone, siltstone, breccia etc. but the one existing in the largest abundance is shale. The formation and deposition of shale occurs after undergoing mineralogical alterations and compression of surplus formation water at differing pressures and temperatures. The primary two processes that give shale its abundant silt/clay quantity, laminated structure and fissile feature are transformation and neoformation. Transformation is a mechanism when a clay mineral, which is new, receives from the former existing material a portion of its silicate skeleton, while neoformation is when the previous mineral structure is not received and there is crystallization of a new mineral by precipitation from solution (Diaz-Perez et al., 2007). Clay minerals occur when older bigger continental rocks, soils and organic matter are eroded, and weathering takes place in an environment that supports formation of shale. Processes such as hydrothermal alterations, chemical weathering, creation and development of diagenetic and authigenic minerals leads to

formation of finer clay sized particles from bigger segments (Diaz-Perez et al., 2007; Du et al., 2017a).

Shale consists of carbonate- and silica-dominant minerals but the majority mineral that shale comprises is clay minerals. Carbonate (dolomite, calcite etc.) and silica-based minerals (quartz, plagioclase etc.) provide shale its geomechanical strength. The usual minerals that compose shale are categorized and listed in Table 2.1. Weaver and Shaw (1965) reported the mean percentage of different minerals that are present in shale. The study based on a sample size of three hundred rocks showed clay minerals as major constituent (60.9%) followed by quartz (30.8%), feldspar (4.5%), carbonate (3.6%) with trace amounts of organic material (1%), iron oxides (less than 0.5%) and other material (2%) (Shaw and Weaver, 1965). The suitable shale composition that makes it an incredible subsurface barrier material is the one with high clay quantity. This composition improves shale's absorption capacities and reduces dissolution and lowers permeability (Tournassat et al., 2015).

Table 2. 1. Mineralogical composition of shale and their general formula (Bregaya et al., 2013; Drever, 1982; Hussain et al., 1996; Yu et al., 2017)

Categories	Minerals	Generic Formulas
Tectosilicates	Quartz	SiO_2
	K-Feldspar	KAlSi_3O_8
	Plagioclase	$\text{NaAlSi}_3\text{O}_8 - \text{CaAl}_2\text{Si}_2\text{O}_8$
Phyllosilicates	Chlorite	$(\text{Mg,Fe})_3(\text{Si,Al})_4\text{O}_{10}(\text{OH})_2.(\text{Mg,Fe})_3(\text{OH})_6$
	Illite	$(\text{K,H}_3\text{O})(\text{Al,Mg,Fe})_2(\text{Si,Al})_4\text{O}_{10}((\text{OH})_2,(\text{H}_2))$
	Kaolinite	$\text{Al}_2\text{Si}_2\text{O}_5(\text{OH})_4$
	Smectite	$(\text{Na,Ca})_{0.33}(\text{Al,Mg})_2(\text{Si}_4\text{O}_{10})(\text{OH})_2.n\text{H}_2\text{O}$

(table cont'd)

(table cont'd)

Other Minerals (Primarily Carbonates)	Calcite	CaCO_3
	Dolomite	$\text{CaMg}(\text{CO}_3)_2$
	Pyrite	FeS_2
	Halite	NaCl
	Hematite	Fe_2O_3
	Ankerite	$\text{Ca}(\text{Fe}, \text{Mg}, \text{Mn})(\text{CO}_3)_2$
	Siderite	FeCO_3
	Fluorapatite	$\text{Ca}(\text{PO}_4)_3\text{F}$

The recent interest into the study and exploration of clay is because of two main reasons: it's remarkable properties and being the most abundant component in shale. The presence of greater oxygen than silicon, magnesium, or aluminum in natural clays' composition makes them heterogenous and is therefore deemed as hydroxides of Si, Al or Mg (Bergaya and Lagaly, 2013). Smectite, illite and kaolinite, all categorized as clay, are the main constituents of shale. The link between the usefulness of shale and its various composition was highlighted by Bourg (2015). The most important factor, clay mineral amount, was established as the feature that manages the material characteristics of these rocks. For operations such as nuclear waste storage and carbon capture and storage the ideal shale to act as a caprock or sealant is with clay quantity greater than 35%. High clay content in shale improves the resistance to creation of fracture and reduces the permeability (Du et al., 2017a.). The low clay content shale is preferable for drawing out unconventional oil and gas since hydraulic fracturing can be done to increase the permeability of the rock (Bourg, 2015).

The fundamental elements that form clay include silicon, aluminum, oxygen, hydrogen in addition to iron, magnesium, potassium and sodium. Tetrahedrons and Octahedrons are the two basic units that make majority of clay minerals (Figure 2.1). There are two proportions that tetrahedron and octahedron can be in, to make a layered structure, 1:1 and 2:1. Kaolinite has a 1:1 layer structure in which one tetrahedron and one octahedron are in a repeating pattern while in smectite there is one octahedron between two tetrahedrons making it a 2:1 proportion layer structure. Tetrahedrons and Octahedrons building blocks and the simplified version of the layer structure for both kaolinite (1:1) and smectite (2:2) can be seen in Figure 2.1.

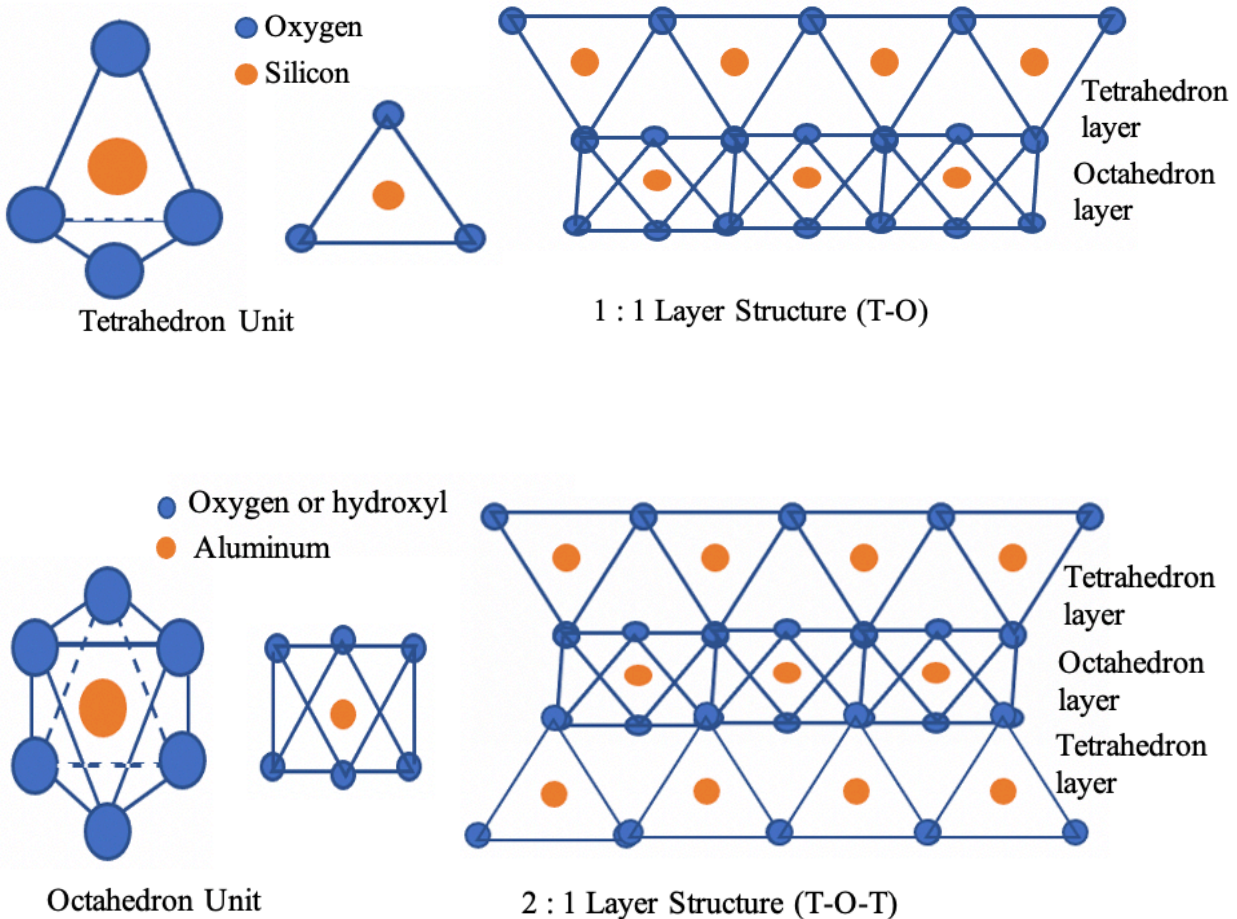


Figure 2. 1. Tetrahedron and Octahedron building blocks and layer structure in clay minerals (Figures redrawn from Nelson, 2015)

The clay particles are formed by these sheet arrangements and the positioning of these particles result in distinct shape, sizes and structures which include fibers minute tubular structure and plates. This is the primary reason why clay minerals have pores of different morphologies i.e., inter-particle, interlayer, inter aggregate pores) (Bergaya and Lagaly, 2013). The structure of the most usual clay particles: Smectite, Kaolinite and Illite be seen in Figure 2.2. As compared to other minerals, clay minerals due to their microstructure, have greater surface area (Van Olphen, 1963; Van Olphen and Fripiat, 1979; Drever, 1982). The clay is also compared to quartz because of its surface area. (Katsube et al., 2003; Bergaya and Lagaly, 2013; Ag Source Laboratories, 2017).

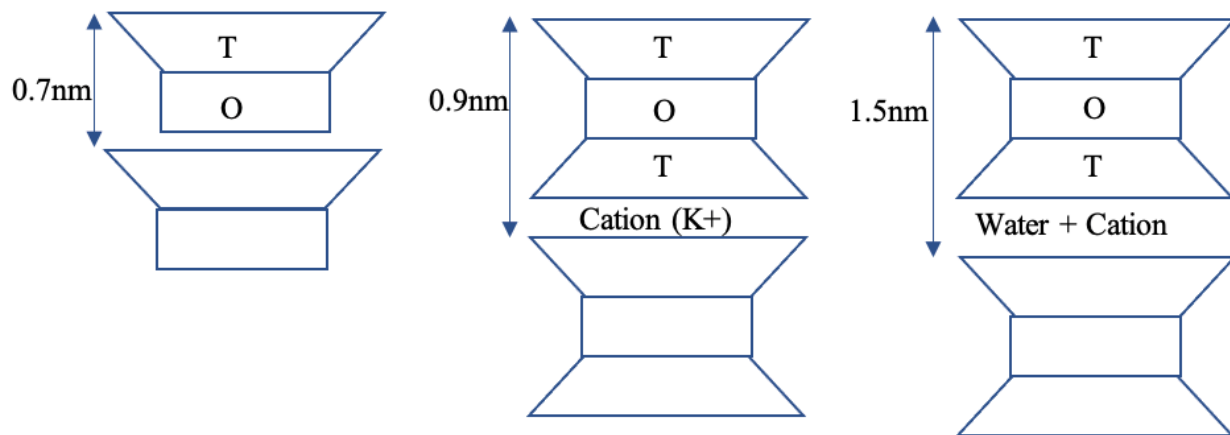


Figure 2. 2. Diagram of three clay structures. a. (T-O) 1:1 layer (kaolinite) b. (T-O-T) 2:1 layer non-expandable (illite) c. (T-O-T) 2:1 layer expandable (smectite). (Figures redraw from Mitchel, 1993)

The low permeability of shale is attributed to its process of diagenetic underground development which includes clay dehydration and staying buried under the pressure of overlying layers. The multi-scale and tight-packing structure identified in the rock is an outcome of tectonic compaction taking place for centuries. (Iverson et al., 2008; Jennings et al., 2007; Thomas and Jennings, 2003). Shale a compositionally heterogenous and multiple-phase rock has tiny interstitial spaces and particle size making it very hard for any fluid i.e., oil, gas or water to advance with in

or flow past the material structure. The ability of shale to withstand the exerted fluid pressure and restrict the movement of water and hydrocarbon makes it a good cap rock. Shale, a low permeable rock, has sufficiently large number of interstitial spaces that act as structures or traps to accumulate fluids, not allowing them to migrate. To increase the permeability and porosity of shale, the petroleum industry is making use of techniques like fracking and directional drilling to stimulate the flow of fluid by producing fractures to create interconnections or pathways inside the rock, hence overcoming shale limitations (King, 2019).

2.2. PORTLAND CEMENT

In the oil and gas industry all over the world, the most widely used subsurface cement for cement slurries is Portland cement (Nelson, 1990). The main application of Portland cement, in petroleum industry, can be divided into three areas: plug and abandonment, remedial wellbore cementing and primary cementing. The primary function of cement is to restrict the flow and movement of underground fluids to the surface by acting as a barrier to isolate zones.

The four unhydrated minerals that Portland cement is composed of are tricalcium silicate (C3S), dicalcium silicate (C2S), tricalcium aluminate (C3A) and tetracalcium aluminoferrite (C4AF) (Nelson, 1990). The two silicate phases constitute 75 to 85 percent of the cement. Table 2.2 shows the mineralogical composition of Portland cement.

Table 2. 2. Cement constituents and composition (Bentz et al., 2000; Lea. 1970; Taylor, 1989, 1997)

Constituents	General Compositions (%)		
	Standard Bogue	Modified Bogue	SEM X-Ray
Tricalcium Silicate	55.4	64.7	62.1
Dicalcium Silicate	19.76	14.4	16.4
Tricalcium Aluminate	6.6	3.47	6.2
Tetracalcium Aluminoferrite	9.3	10.8	8.6
Insoluble Residue	0.16	0.16	0.16
Sulphur trioxide	1.9 – 3	1.9 – 3	1.9 – 3
Magnesia	0.69 – 6	0.69 – 6	0.69 – 6
Alkali	0.3 – 0.75	0.3 – 0.75	0.3 – 0.75
Free Lime	0.64	0.64	0.64
Gypsum	2	2	2
Loss on Ignition	0.81	0.81	0.81

The two reactants, limestone and clay, react at a temperature of 1480⁰C to form the Anhydrous cement clinker. These are anhydrous compounds and result in hydrated compounds after their reaction with water. The exothermic reaction of cement with water results in the formation of slurry, however, there still remains cement particles that are anhydrous after the hardening of cement paste and after a period of 28 days the extent of hydrations is unchanged (Hewlett, 2004). The cement hardening can take place in different environments i.e., in air or

undersea, generating heat in the process. The products of the exothermic reaction are calcium hydroxide i.e., approximately 20 percent and calcium silicate hydrate i.e., roughly 70 percent, as well as small amount of ettringite seen in table 2.3.

Table 2. 3. Hydrated cement products

Hydrated Products	Notation	Mineral Name	Chemical Formula	Concentration
Calcium Silicate Hydrate	CSH	Jennite Tobermorite	$3\text{CaO} \cdot 2\text{SiO}_2 \cdot 3\text{H}_2\text{O}$	50 – 70
Calcium Hydroxide	CH	Portlandite	$\text{Ca}(\text{OH})_2$	15 – 25
Ettringite			$\text{Ca}_6\text{Al}_2(\text{SO}_4)_3(\text{OH})_{12} \cdot 26\text{H}_2\text{O}$	

Among the two primary products, non-crystalline calcium silicate hydrate, is the compound that determines the strength of the hardened paste since it is the phase that binds the matrix (Taylor, 1997). Ettringite is also one of the products of the cement water reaction and plays a vital role during the reaction in connecting various minerals. The calcium hydroxide in the final product is maintained by the alkalinity of the material, while the water-cement ratio in the cement controls its alkalinity. The pore water present in the cement makes it alkaline in nature with a pH of roughly 13.

Three very important properties of the hydrated cement dependents on several factors that include curing conditions, cement type and its fineness, additives and the water cement ratio. The strength of the cement is indirectly proportional to the porosity and permeability of the cement during the hydration process, i.e., towards the completion of the reaction the strength of the material increases while the porosity and permeability decrease. For cement, the extent of

hydration, with the usual water-cement ratio, in the range of 0.3 to 0.6 does not change after a month, however, at high temperatures this stage attained in a shorter time (Taylor, 1997).

The Portland cement is used in the oil and gas industry with various formulations depending on the subsurface conditions and requirements. The American Petroleum Institute categories the Portland cement into 8 different classes in API RP-10B. This classification is based primarily on the level of cement's resistance to sulfate and cement rate of hydration (Recommended Practice for Testing Oil-Well Cements and Cement Additives, 1977). Table 2.4 shows the different groups of cement and their composition. Cement class G and H, both, in the absence of additives can be utilized in cementing jobs up to 8,000 ft and after the addition of additives greater wellbore depths can be reached. The grain size of the cement determines the amount of water required for cement slurry formation i.e., when the grain size is very fine the surface area of the material increases and as a result higher water-cement ratio is required for hydrated cement. Class H cement grain size is coarser as compared to class G making the surface area of class H cement smaller ($1600 \text{ cm}^2/\text{gr}$) than class G ($1800 \text{ cm}^2/\text{gr}$). This results in the water-cement ratio of class G higher (0.44) than class H cement (0.38). To address the extreme subsurface conditions (i.e., high pressure high temperature (HPHT)) there have been a few other types of cement introduced as well (Nelson et al., 2006).

Table 2. 4. The eight API groups of cement and their general percentage composition (Nelson, 1990)

Class	C ₃ S	C ₂ S	C ₃ A	C ₄ A
A	53	24	8	8
B	47	32	5	12
C	58	16	8	8

(table cont'd)

(table cont'd)

D, E	26	54	2	12
G, H	50	30	5	12

Table 2. 5. Use of cement classes as specified by API (Habrate et al., 1980; Raczkowski et al., 1978)

Class	Application of Depth (m)	Temperature (°C)
A	0 – 1830	44 – 94
B	0 – 1830	44 – 94
C	0 – 1830	44 – 94
D	1830 – 3050	94 – 144
E	1830 – 3050	94 – 144
F	3050 – 4880	127 – 167
G	0 – 2440	44 – 111
H	0 – 2440	44 – 111

The cement hydration process is categorized into five stages (Locher et al., 2000; Stark et al., 2000) and each step is explained more in detail below.

1. Pre-induction
2. Induction also referred to as Dormant
3. Acceleration
4. Deceleration
5. Steady state or Diffusion stage

Pre-induction stage

The cement compounds, primarily silicates i.e., tricalcium silicate and di calcium silicate and sulphates start to dissolve upon interaction with water. These compounds release calcium, sulphate and aluminum hydroxide ions. This dissolution in the early-stage releases heat. Briefly after the formation of the non-crystalline calcium silicate hydrate (C-S-H) gel, the tricalcium silicate stops dissolving. The reason for the stoppage of hydration of tricalcium silicate is because the production of calcium silicate hydrate leaves a low permeable sheet on its surface. Among the silicate compounds only a small part (i.e., 2 to 10 percent) of tricalcium silicate is hydrated while the dicalcium remains unreactive. The pre-induction period also witnesses the formation of ettringite after the hydration of calcium aluminate (i.e., in the range of 5 to 25 percent) (Odler, 1998; Stark et al., 2000).

Induction stage

The quick buildup of hydrate compounds on anhydrous materials impedes the dissolving of silicate and sulfate phases as a result the hydration process slacks off and there is a decline in the heat release. During this stage, the amount of calcium hydroxide ions in the solution is the highest and after a short time starts to drop. In contrast, the relative amount of sulphate ions remains unchanged, the reason for which is, as soon as the concentration of sulphate ions is reduced due to the production of ettringite, calcium sulphate starts to dissolve, maintaining the quantity of sulphate ions in the water. (Locher, 2000; Odler, 1998)

Acceleration stage

The initiation of this phase occurs as the hydrated products deposited on the anhydrous material starts to break down due to osmosis (Locher, 2000). The process of hydration for both the

silicate compounds, tricalcium silicate and dicalcium silicate, speeds up leading to the production of a 'second stage' hydrated calcium silicate. The result of this exothermic reaction causes the highest amount of heats release. When compared, the reactivity of both silicate compounds, tricalcium silicate still dominates dicalcium silicate. The products formed in this stage are hydrated calcium silicate, notable quantity of calcium hydroxide also known as portlandite and ettringite. The formation of ettringite continues until calcium sulfate dissipates completely and the quantity of sulphate ions decline (Locher, 2000; Odler, 1998).

Deceleration stage

During this phase, the hydration process of cement starts to fall as the quantity of remaining anhydrous cement compounds reduce. This causes the heat generated to drop as well. In this period, the reactivity of dicalcium silicates is dominant over tricalcium silicate and contributes more towards the production of hydrated calcium silicate. The recrystallization of existing ettringite with the remaining two cement compounds, tricalcium aluminate and tetra aluminate ferrite, generates monosulfate. This occurs due to the reduced amount of available sulfate ion in the solution (Odler, 1998).

Steady State stage

In comparison, the first phase where the quick surface reaction is dominant in the hydration process, in the last phase reactions are predominantly diffusion based. The reason is the covering of cement clinker by the high-density hydrated products. Once the cement hydration is finished, chances are that the ageing of the already produced hydrate initiates which results in the augmentation of hydrated calcium silicate chain length (Stark et al., 2000).

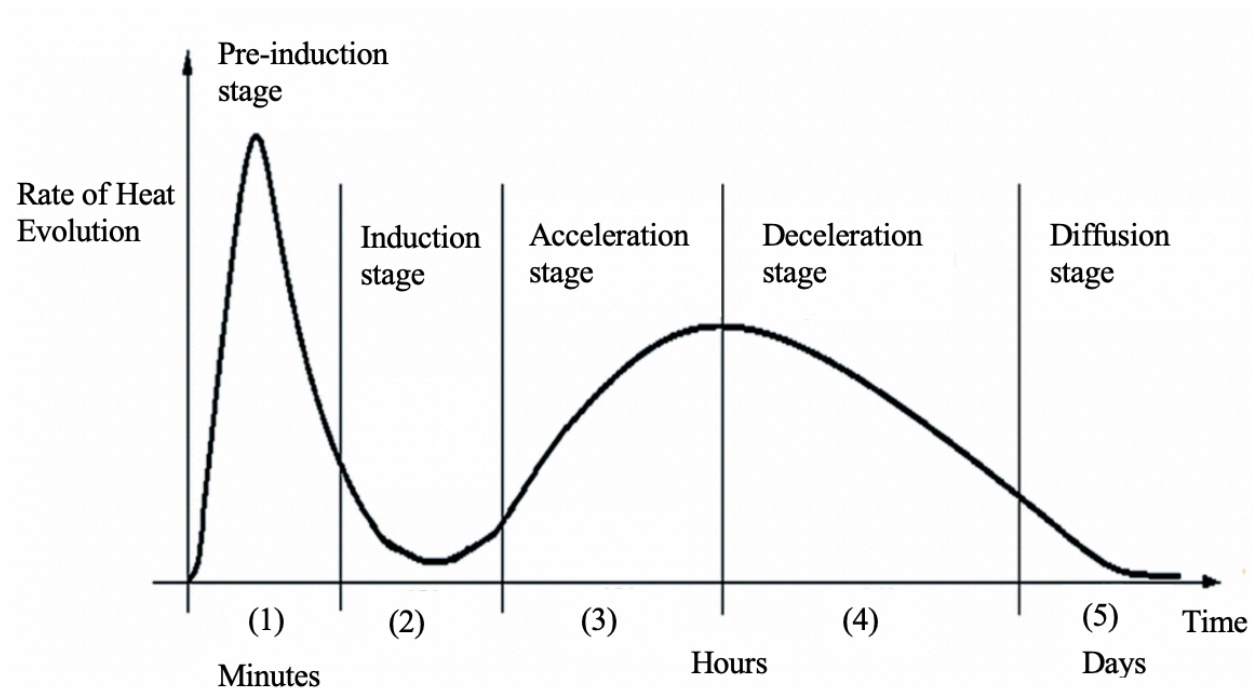


Figure 2. 3. The different stages of hydration process (Zhang et al., 2005)

Table 2. 6. The major cement constituents, their attributes and their hydration equation

Chemical Name/Mineral Name/ Notation/Chemical Formula	Attributes	Hydration Equation
Tricalcium Silicate Alite C_3S $Ca_3(SiO_4)O$	<ul style="list-style-type: none"> Primary compound in cement Contributes to strength development, especially in the initial period 	$3 CaO \cdot SiO_2 + x H_2O \rightarrow y CaO \cdot SiO_2 \cdot (y-(3-x)) H_2O + (3-y) Ca(OH)_2$ Reaction of C_3S with water gives C-S-H (gel phase) and Portlandite
Dicalcium Silicate Belite	<ul style="list-style-type: none"> Slower hydrating compound than C_3S 	$2 CaO \cdot SiO_2 + x H_2O \rightarrow y CaO \cdot SiO_2 \cdot (y-(2-x)) H_2O + (2-y) Ca(OH)_2$

(table cont'd)

(table cont'd)

C_2S $Ca_2(SiO_4)$	<ul style="list-style-type: none"> Contributed to gradual increase in strength, over longer period 	Reaction of C_2S with water gives C-S-H (gel phase) and Portlandite
Tricalcium Aluminate Aluminate C_3A $Ca_9(Al_6O_{18})$	<ul style="list-style-type: none"> Stimulate fast cement hydration Control cement settling time Manage cements resistance to sulfate attack Gypsum added manage hydration and flash setting Generates most heat in the initial stage 	$C_3A + 3 CaSO_4 + 26 H \rightarrow C_3A \cdot 3 CaSO_4 \cdot 32 H$ Reaction of C_3A with gypsum (Calcium Sulphate) and water gives Ettringite
Tetracalcium Alumino Ferrite Ferrite C_4AF $Ca_4Al_2Fe_2O_{10}$	<ul style="list-style-type: none"> Promotes low heat of hydration 	$3 C_4AF + 12 CaSO_4 + 110 H \rightarrow 4 (C_3(A,F) \cdot 3 CaSO_4 \cdot 32) + 2 ((A,F) \cdot 3 H)$ Reaction of C_4AF with gypsum and water gives Iron ettringite

The use of additives in the cement to improve qualities like low permeability, developing strength swiftly enforces its feature to act as a strong barrier, hence providing the necessary isolation needed between zones. To deal with the subsurface conditions (i.e., corrosive fluids, high pressure formation fluids), the need for additives in cement becomes vital in order to adjust to the harsh underground environment. Currently, there are over one hundred additives present that fall under the main categories, mentioned below (Nelson et al., 2006):

Extenders lower the slurry density which is required in weaker formations. Some examples of

extender include bentonite, pozzolans, both of which contribute to increase the yield point (i.e., increased resistance to stress required to gas, water oil flow). Its percentage in cement composition is between 1 to 16.

- Retarders do not allow quick cement hardening rather increase the setting time. Common examples include lignosulfonates and hydroxycarboxylic acid;
- Accelerators perform the opposite function of retarder, which means that they accelerate the reaction rate and, as a result, lower the cement slurry settling time. Chloride salts, carbonates, silicates alkaline bases are all examples of accelerators;
- Dispersants (like polynaphthalene sulfonate) change the rheological properties of cement hence allowing the cement to adjust its attribute to flow as well as its viscosity; and
- Weighting agents are extremely important in conditions where the pore pressure is high, or wellbore is not stable because they increase the slurry density.
- Other additives include fluid loss control agents and lost circulation control agents.

The required cement characteristics like resistance to fracture due to thermal differential, maintaining strength and restrict the dissolution of calcium hydroxide can be achieved by additives like silica flour, pozzolan and steel/polymer fiber. The factors that influence the final behavior of additives are pressure, temperature, water cement ratio, mixing energy and order and additives amount. The chemical properties of cement (such as sulfate content, aluminate and silicate arrangement, reactivity of hydrating phase, ration of gypsum) and physical properties (like particle size and surface area of hydration products), all influence the additive performance. All of these various aspects reinforce the importance of testing in labs before formation of the cement product for field operation (Nelson et al., 2006).

2.3. SANDSTONE

An estimated 40% of the hydrocarbon reservoirs, globally, is dominated by siliciclastic sandstone (Bagrintseva, 2015). The pore space present in sandstone allows it to, both, accumulate hydrocarbon, which can be gas or liquid, and discharge under different subsurface conditions i.e., pressure and temperature. This is one of the reasons for the presence of formation fluids in the sandstone rocks (Adepehin, 2014).

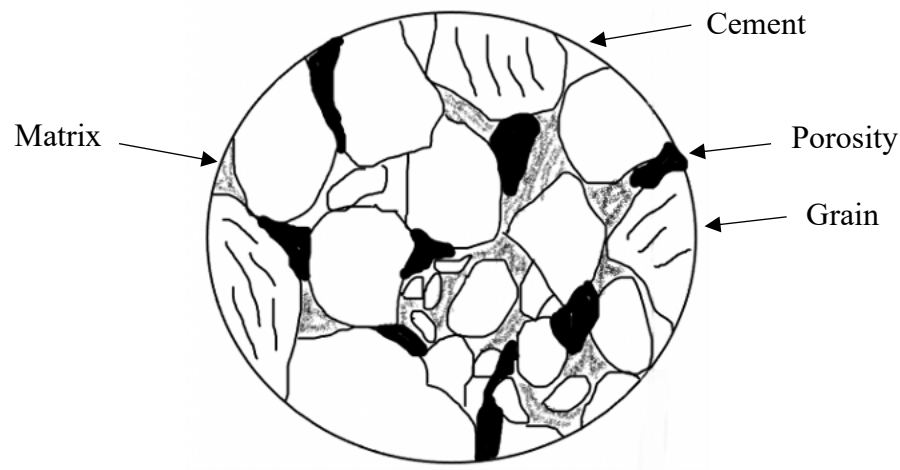


Figure 2. 4. Drawing of microstructure showing four elements of sandstone. Redrawn from Selley (2000)

The sandstone rock is composed of four main elements: matrix, grains, cement and porosity as shown in Figure 2.4. The particles size of the rock is in the range of 0.06 mm to 2 mm in diameter. The grains in the rock make up the framework of sandstone, hence called the framework grains. The deposition of the matrix constituent of the rock and framework grains is done in the same time period; however, the size of the matrix particles is much smaller and may fall between the voids and the framework grains. Sandstones with less or no matrix are classified as texturally clean sandstone, while sandstone with decent matrix quantity is identified as texturally dirt sandstone. The third component, cement, ties the framework grains together in a structure. Cement

gets precipitated, once the framework grains and cement have deposited. Therefore, cement is secondary or postdepositional, while matrix is syndepositional. The syndepositional and postdepositional conditions have an impact on the sandstone formation properties (Morad et al., 2012; Herlinger Jr et al., 2017). The properties influenced by syndepositional conditions include texture and petrology, while sandstone's intrinsic properties, that are vital in the production of hydrocarbons present in formation pore spaces, are impacted by postdepositional conditions (Lai et al., 2015; 2016).

The three primary materials that provide the sandstone framework and are classified under framework grain are quartz, feldspar and rock fragments. Quartz framework grains exist in three kinds such as monocrystalline, polycrystalline and chert. Figure 2.5 shows monocrystalline and polycrystalline quartz.

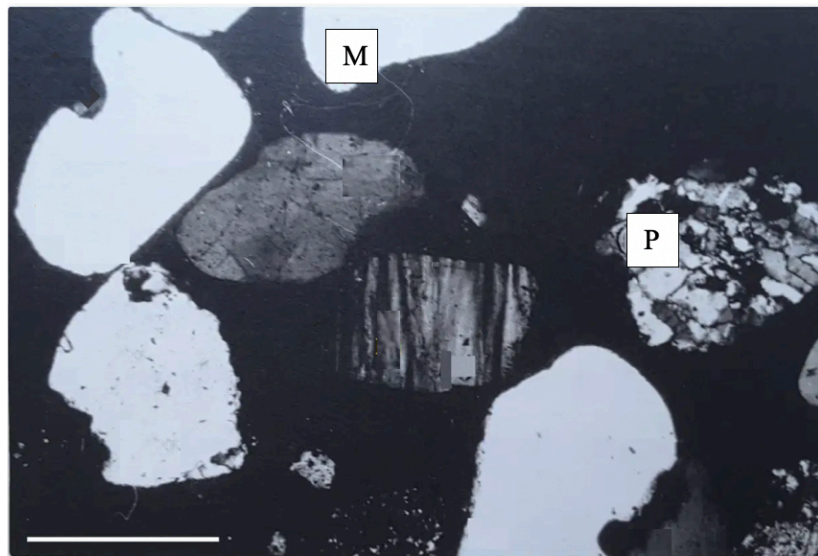


Figure 2. 5. Microstructure showing two different kinds of quartz grains. M is monocrystalline quartz. P is polycrystalline quartz (source: Geological Digressions)

The two kinds of feldspar framework grains present in sandstone are plagioclases and K feldspar. The chemical composition of plagioclases feldspar is between $\text{NaAlSi}_3\text{O}_8$ and $\text{CaAl}_2\text{Si}_2\text{O}_8$ range i.e., the mineral composition is based on sodium and calcium proportions. Sodium dominant

plagioclase are referred to as albite, whereas the calcium dominant types are called anorthite. The K-feldspar composition is in KAlSi_3O_8 to $\text{NaAlSi}_3\text{O}_8$ range (i.e., all of its mineral composition is based on potassium and sodium). Feldspar easily converts to calcite and clay (i.e., kaolinite).

The framework grains may also contain accessory minerals. There are grains present in sandstone in a minute amount. Minerals that come under accessory grains include mica (i.e., muscovite and biotite) and pyroxene olivine. The density of these minerals is higher than the silicate minerals. Garnet, zircon and magnetite are examples of these heavy minerals. The mixture of clay with feldspar and fine quartz sized particles forms the matrix component of sandstone. Common cements observed in sandstone include quartz, calcite dolomite, siderite, hematite, limonite, pyrite, gypsum and barite.

2.4. LIMESTONE

Carbonate rocks, classified under sedimentary rocks, primarily consist of carbonate minerals and are divided into two major groups: limestone and dolomite. (Ham et al., 1962; Leighton et al., 1962., Zhao et al., 2016). Carbonate rocks contribute to a majority of oil and gas reservoirs, while some fine grained carbonate rocks that developed under low-energy environments (slow moving currents) are considered hydrocarbon source rocks (Tissot et al., 1984; Katz et al., 2000; Xie et al., 2016). The composition of modern carbonate rocks include aragonite (i.e., CaCO_3 , a metastable mineral), and calcite dominant in magnesium. These two minerals during the process of diagenesis promptly recrystallize to calcite. In contrast, ancient carbonate rocks, in addition to calcite and dolomite, also include magnesite (i.e., MgCO_3) and siderite (i.e., FeCO_3).

Limestone is a non-siliciclastic sedimentary rock formed by either, chemical precipitation or accumulation of pre-existent calcite. The composition of limestone includes predominantly

calcite (more than 50 percent) along with metal oxides, silicates and traces of other impurities. Limestone, mineralogically, can be considered as magnesian calcite, pure calcite, dolomite or combination of all these minerals in different quantities. The porosity and permeability of limestone are greatly influenced by the size of sediments, and very fine limestone sediments lead to the formation of a low permeability and dense rock. Limestones formed by chemical precipitation create a granular structure. The texture of limestone can be transformed when there is flow of water through its pores which leads to generation of vugs due to leaching of sediments. The interconnection of these vugs can cause the porosity and permeability to be significantly increased. However, the porosity and permeability can be minimized with calcite deposition. The structure of calcite crystals (i.e., calcium carbonate), exists as a rhombohedral unit. The partial replacement of calcium with magnesium by water may lead to the formation of magnesium-calcium carbonate and, as a result, development of dolomite. The structure of dolomite, similar to calcite, is rhombohedral although the strength of lattice is enhanced with the incorporation of magnesium. Dolomite as compared to pure calcite is more thermodynamically stable, but the process of dolomitization causes higher porosity since the calcite unit cell, which gets replaced by dolomite unit cell, is less compact. The range of porosity for carbonate rocks is between 5 percent to 35 percent depending on the extent of dolomitization.

2.5. CEMENT-ROCK INTERFACE IN THE WELLBORE

The importance of cement-rock bond has a vital role in providing subsurface zonal isolation and preventing any wellbore breakouts, but little focus has been put into comprehension of the cement-rock bond (Carey et al., 2007; Ladva et al., 2005). As compared to the oil and gas engineering, the civil engineering has shown more interest in understanding the bonding mechanism between cement and rock. According to these research studies, two primary factors are

responsible for the bond between cement and formation: the mechanical interlocking between the hydrated cement compounds and the formation particles and cement-rock chemical reaction (Tasong et al., 1998; Ollivier et al., 1995). The relationship with between the surface roughness of the interface and mechanical interlocking bonding mechanism are directly proportional (i.e., the greater the surface roughness, the more the mechanical bonding). The surface area is another feature that is increased upon enhancing the surface roughness as a result improving the bonding (Tasong et al., 1998). This implies that the cement-rock bond can be stronger when the wellbore wall has increased roughness. The different kind of subsurface rocks with distinct material compositions upon interaction with the cement paste makes the chemical reaction, second factor behind the cement-rock bonding, a lot more complex to analyze.

The interfacial transition zone (ITZ) also known as the transition zone is defined as the high porosity zone that prevails between the cement-rock interface therefore the boundary of this zone is not explicitly identified or outlined. The size disparity between cement and rock particles gives rise to the wall effect, the phenomenon behind the creation of transition zone. The rock particle size is in the range of 70 to 2000 μm whereas the cement is in 5 to 60 μm range (Caenn et al., 2011; Hewlett, 2004;). The grains' size difference between the two materials makes the rock particles seem like a wall in comparison to cement particles. This leads to higher porosity and pile up of water at the transition zone. The phenomenon of wall effect is more prominent in 15 to 20 μm of rock particles. In the beginning, the porosity of transition zone in contrast to bulk cement is approximately 40 percent greater which causes the calcium ions to convert to calcium hydroxide at the transition zone after migrating from the cement zone. The sand particles experience a formation of calcium hydroxide layer after the conversion of calcium ions. After a period of time, the porosity difference between transition zone and bulk cement falls from 40 percent, initially, to

10 to 20 percent because of the formation of compounds like ettringite and calcium silicate hydrate (Scrivener et al., 2004).

The elements that have an impact of the cement-rock interfacial bonding are stress caused by temperature and pressure variations over the well life cycle, improper drilling mud displacement, and geologic disturbances underground. Plate tectonic is mostly the reason for underground geologic discontinuities (Duguid et al., 2010). The interfacial bond between cement and rock deteriorates because of all of these events, thus allowing formation of channels for fluid movement.

3. METHODOLOGY

The primary framework for conducting this research encompasses following three steps:

- I. Preparing and curing cement-rock interfaces
- II. Analyzing the cement-rock interface using SEM
- III. Hardness test of cement, rock and interface

3.1. PREPARING AND CURING CEMENT TO ROCK INTERFACES

Portland cement was donated by BJ Services company, and rock samples were obtained from Kocurek. The bonded bi-material samples, three different reservoir rocks, sandstone, limestone and shale supplemented with high density cement, cured at reservoir pressure and temperature, were fabricated at the service company facility.

The quarter cement cores were created from class H cement with water-cement (w/c) ratio of 0.38 in accordance with American Petroleum Institute (API) guidelines (API. Recommended Practice 10B-2, 2013) which made the cement density 17 ppg. The cement and water, in required quantiles, were mixed at 4000 RPM for a time span of 15 seconds and then again at 12000 RPM for 35 seconds. After preparing the cement slurry, curing was done in a temperature range of 135 to 170°C and pressure between 1500 to 3000psi using high pressure high temperature curing chamber. Curing was done after pouring the cement in custom made semicircular brass molds (Figure 3.1 and 3.2) with a quarter circle formation rock for 24 hours as per the API standards, to simulate cement setting under high pressure high temperature conditions. It was ensured that the cement and rock were properly bonded and there was an adequate contact between the two. Cement cured with rock and cement-rock can be seen in the Figure 3.3.



Figure 3. 1. Semicircular custom-made brass molds

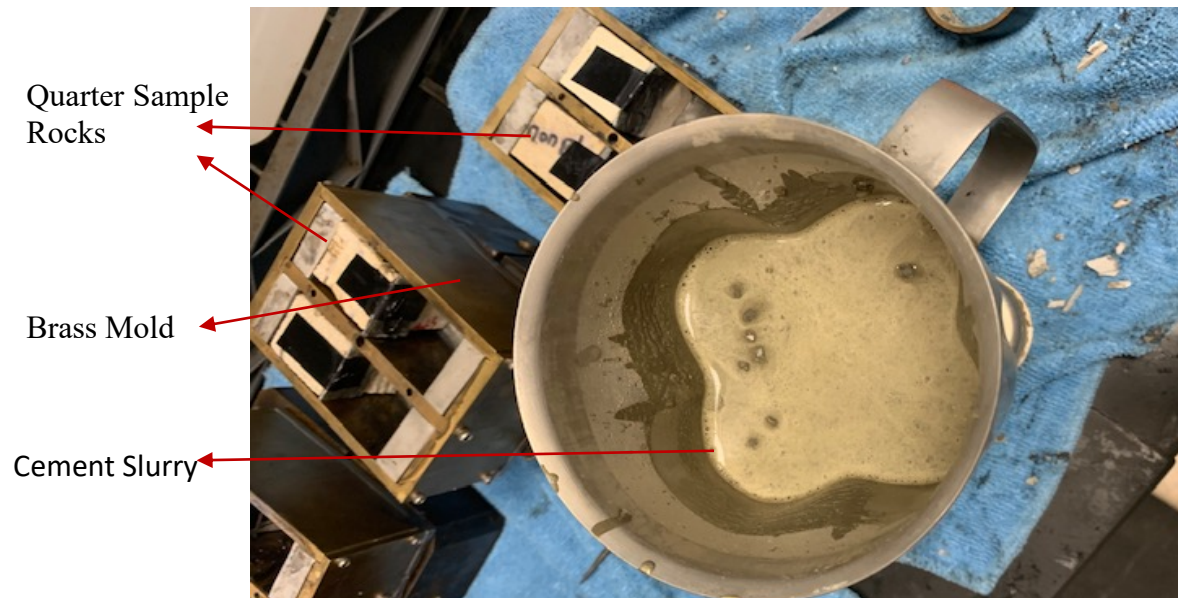


Figure 3. 2. Cement slurry with quarter rock samples in brass molds

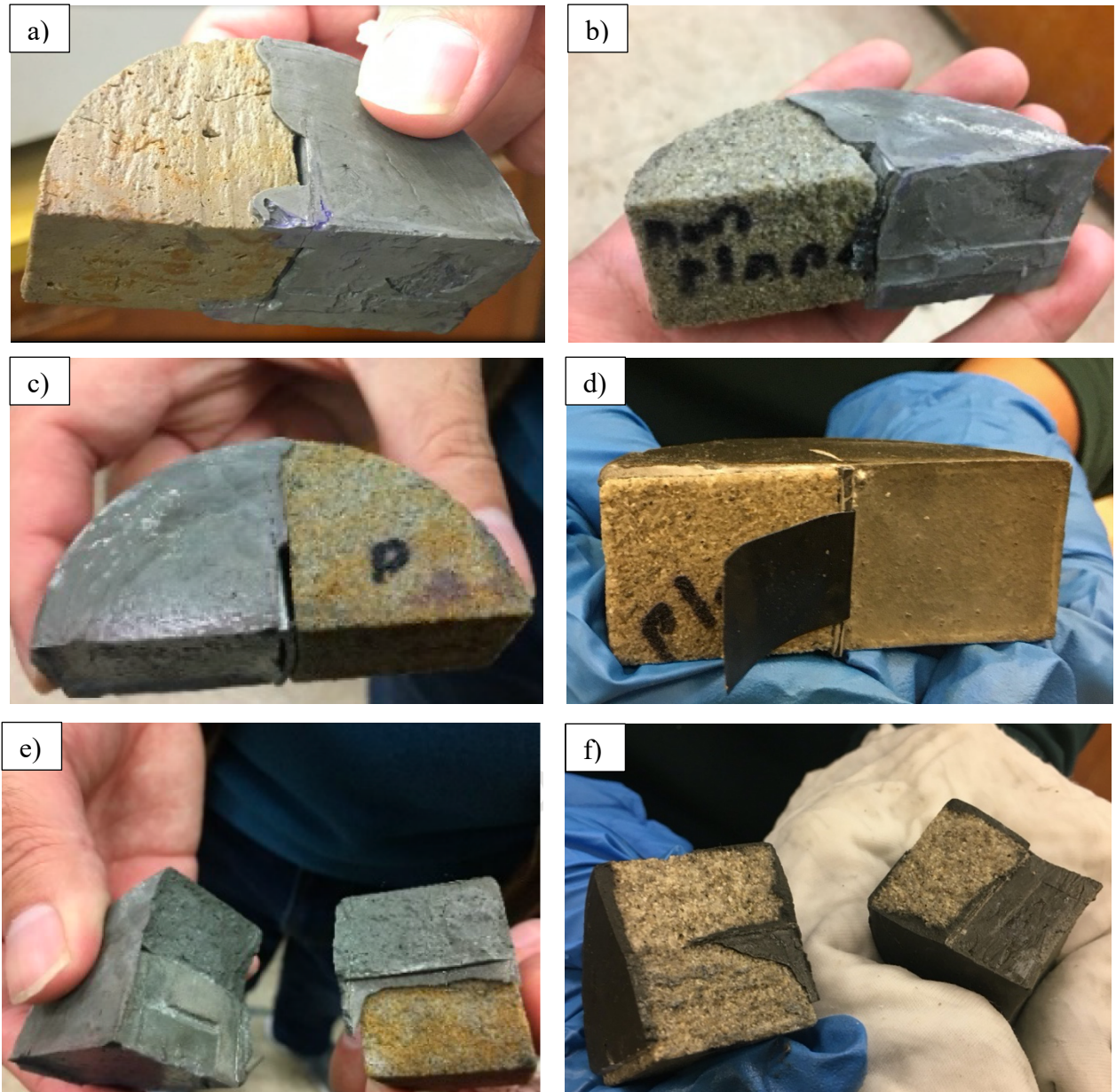


Figure 3. 3. Cured bi-material samples a) b) c) d) before fracture e) f) cement-rock interface

3.2. SEMI CIRCULAR BEND TEST (SCBT) FOR MECHANICAL TESTING

The Semi-Circular Bend test (SCBT), which is a laboratory mechanical experiment and establishes when a material will fracture under applied load, was used to calculate the fracture toughness of the bi-material cement-rock samples. Fracture toughness can be defined as the resistance of the cement-rock sample to the growth of a preceding crack. The SCBT experiments were performed at the Louisiana Transportation Research Center (LTRC).

In this study, for the SCBT experiments in order to imitate the underground hydraulic fracturing, only mode I was considered. The loading occurs mostly in mode I, and the damage produced is the highest. Mode I, also known as the Opening mode, is where the tensile stress is perpendicular to the plane of crack. In the three-point bend SCBT configuration, a monotonic load, which is a single time loading process, was applied vertically on the top of the bonded, quarter cement-quarter rock, bi material sample. For obtaining mode I properties, the force was applied, normal to and directly above the vertical notch, between the two materials i.e., cement and rock, interface.

The three-point bending configuration involves sample support on two ends with one point of deflection coming from the top center of the material. To subject bi-material samples to three-point SCBT, custom-made SCB rig combined with compressive loading frames were used (Figure 3.4). The bi-material samples were supported by two rods during the loading process and the load and displacement were continuously recorded during the test until the sample failed. Upon the application of large enough force, the crack conceivably starts to grow in the direction of the predefined fracture i.e., notch. The custom-made rig was set up on the apparatus, Humboldt Master Loader HM-300, used for conducting the SCPT experiments (Figure 3.5).

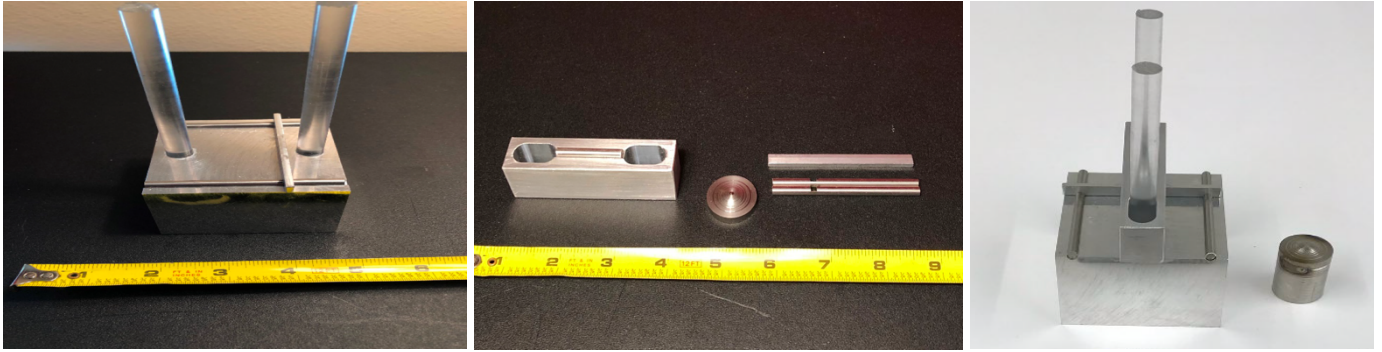


Figure 3. 4. Semi-Circular Bend custom made rig with compressive loading frame



Figure 3. 5. Three-point bend semi-circular bend test apparatus connected with laptop to generate load-displacement curves, and rig set up

The fracture toughness for the bi-material samples was calculated using the critical stress intensity factor and the peak load observed to fracture the sample. The fracture toughness was calculated using the following equation (Chong and Kuruppu, 1984)

$$K_I = \frac{P_{max} \sqrt{\pi a}}{2RB} Y_I \quad (1)$$

where,

K_I is the fracture toughness

P_{max} is maximum load at which the sample fails

a is the notch length

R and B are the sample radius and thickness, respectively

Y_I is the non-dimensional stress intensity factor

The following equation was used to calculate the non-dimensional stress intensity factor

$$Y_I = -1.297 + 9.516 \left(\frac{s}{2R} \right) - \left(0.47 + 16.457 \left(\frac{s}{2R} \right) \right) \beta + (1.071 + 34.401 \left(\frac{s}{2R} \right)) \beta^2 \quad (2)$$

where,

s is the distance between the two rollers, also known as, span length

b is the ratio of notch length, a , to sample radius, R , or a/R

The SCBT sample geometry and force arrangements can be seen in Figure 3.6.

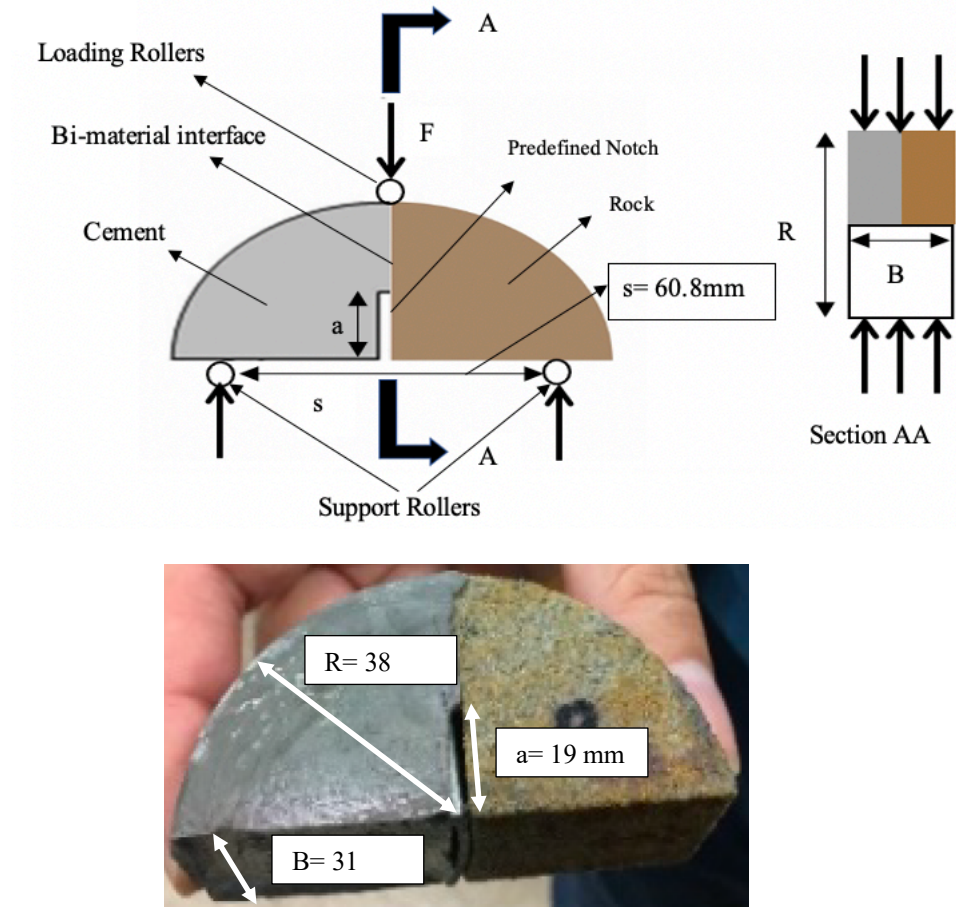


Figure 3. 6. SCBT schematic loading arrangement and specimen geometry

3.3.ANALYZING THE CEMENT-ROCK INTERFACE USING SEM

3.3.1. SPECIMEN PREPARATION

Samples for SEM analysis were prepared in four major steps: (a) thin section preparation, (b) sample drying, (c) sputter coating with conductive material and (d) mounting on a stub.

Thin Section Preparation

The first stage of sample preparation was creating thin section cuts. Diamond bandsaw

was used along with water as a coolant to obtain the rock cement interface region. To cause a minimum amount of material deformation to sample, materials' true microstructure was preserved while cutting, and additional steps needed for the sample preparation process were minimized.

Sample Drying

A high vacuum environment is required for image formation in an electron microscope. Therefore, to view and obtain good images in a normal high vacuum SEM system, drying of samples becomes a prerequisite step. Pre-baking involved cleaning and degreasing the sample with alcohol (100% ethanol) after which it was oven dried at 60°C for 10 minutes.

Sputter Coating with Conductive Material

The sample being nonconductive causes image distortion due to charge effect and therefore, coating of samples is required to improve the imaging of samples. A conductive layer of platinum was coated on the sample to prevent charging of specimen, reduce thermal damage and improves the electron signal required for examination in the SEM. Argon gas was used as a sputter gas and a 5-10nm thickness of platinum was coated at a vacuum level of 2×10^{-2} mbar.

Mounting on a Stub

Sample were mounted on the stubs using double-sided vacuum compatible carbon conductive tapes before their placement in the SEM chamber to prevent any vibrations or movement.

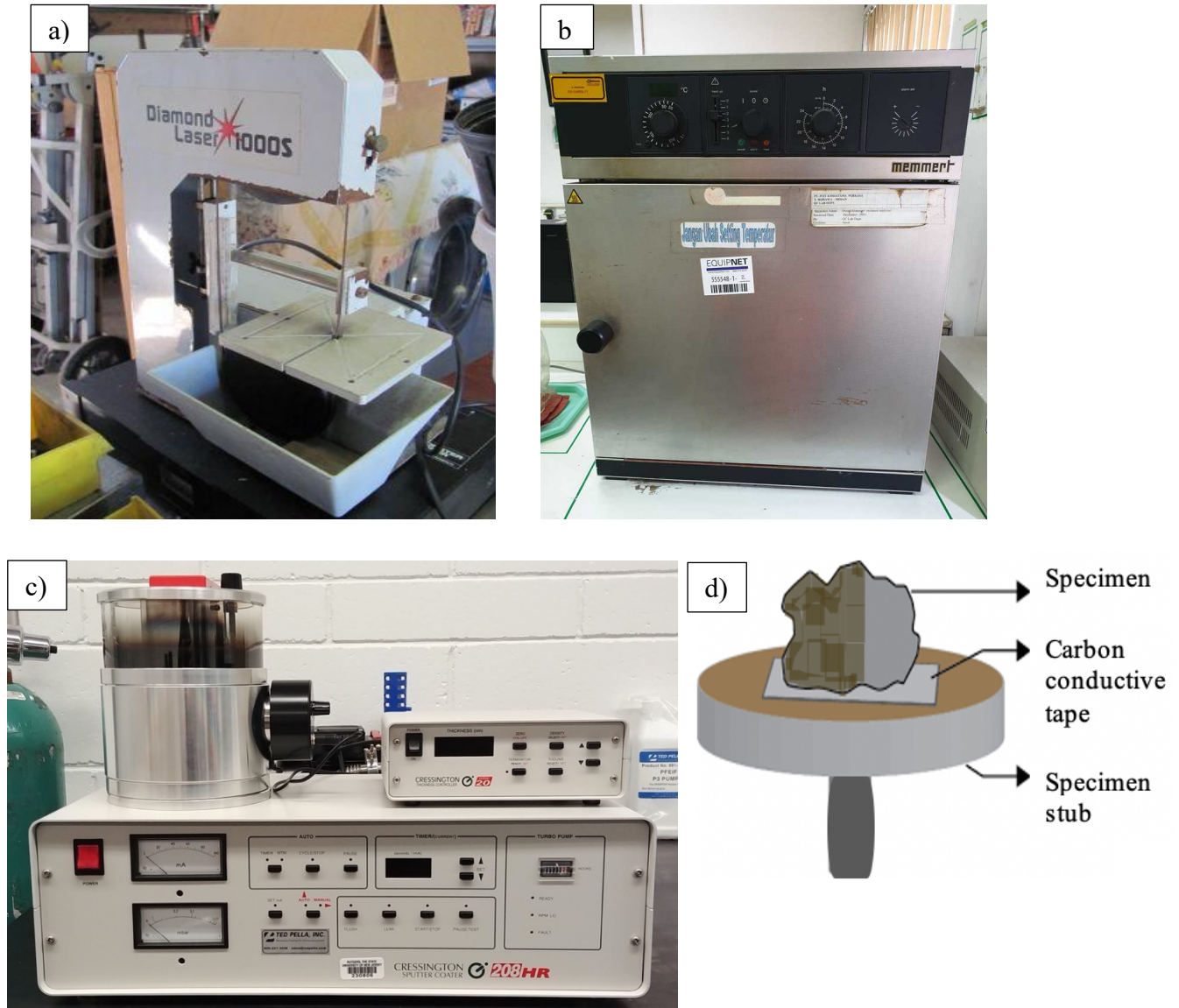


Figure 3. 7. Equipment used in sample preparation a) Diamond bandsaw for cutting samples in thin sections b) Oven to dry the samples before SEM analysis c) Sputter Coater to coat the sample with conductive layer. d) Stub with a sample attached using carbon conductive tape

3.3.2. SCANNING ELECTRON MICROSCOPE (SEM)

The SEM imaging of the three bi-material samples was performed at LSU Shared Instrumentation Facility (SIF). Quanta 3D DualBeam FEG FIB-SEM (combination of a Focused Ion Beam (FIB) with a high-resolution Field Emission Gun Scanning Electron Microscope (FEG-SEM)) (Figure 3.8), 500V-30kV accelerating voltage, probes current up to 36n, and 1.3nm in

second electron imaging (SEI) resolution was used to analyze microstructures. Microphotographs were obtained using two imaging modes, back scattered electron (BSE) and secondary electron (SE) imaging at 250-35000 \times magnifications, to understand microstructural properties of the samples. Elemental mapping at the microstructural level and collecting spectrum was performed by EDAX energy dispersive spectrometer (EDS) spectrum viewer software to identify chemical element distribution. Microstructures of pure cement, pure rock and rock-cement interface were analyzed for the three bi-material samples.

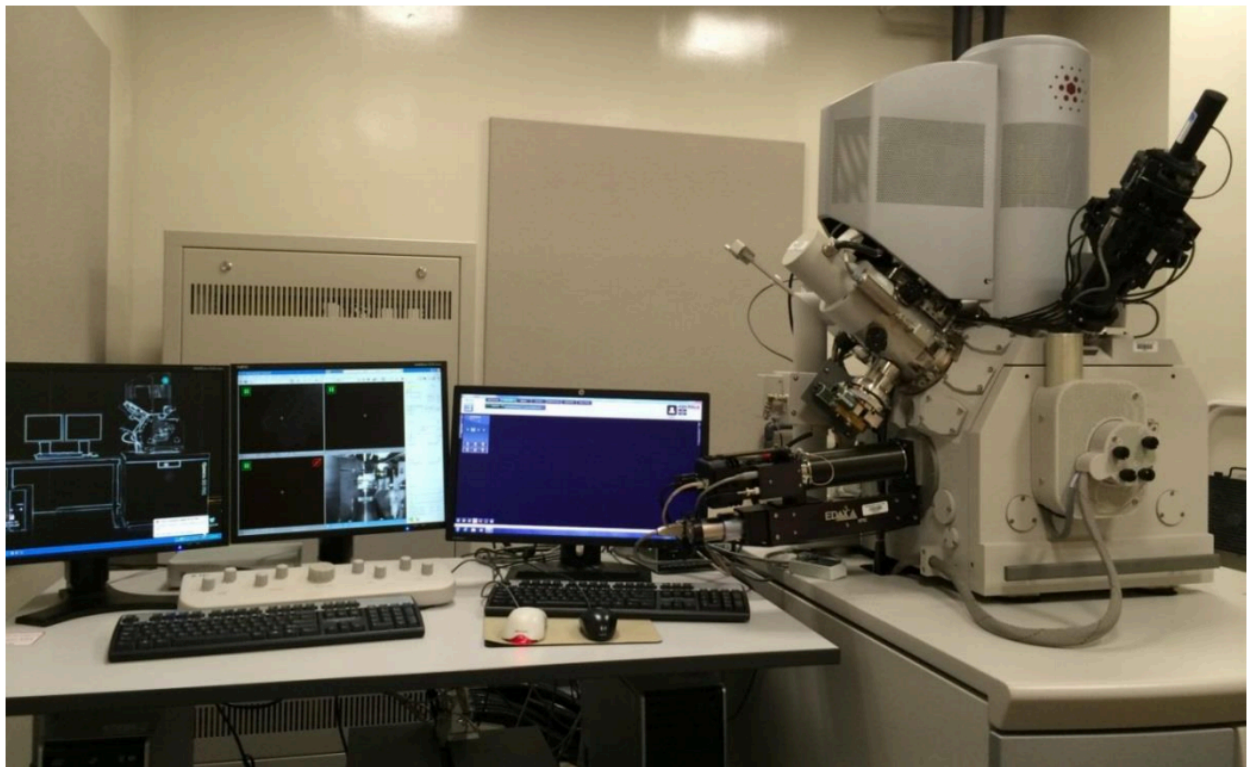


Figure 3. 8. Scanning Electron Microscope used to obtain micrographs in this study

The principal parts of SEM include an electron source (a downward column which has electromagnetic lenses that direct movement of electrons), an electron detector (a sample chamber to hold the sample under vacuum, and connected with), is a computer see the microphotographs and results. Electron source at the upper end of the column generates electrons, which are

converted into a directed ray after passing through a series of aperture and lens. This focused beam then reaches the chamber area where it strikes the top of the sample. The more advanced EDAX Pegasus EDS & EBSD system further allows the study of a more precise composition analysis, crystallographic orientation, element distribution, and grain size distribution.

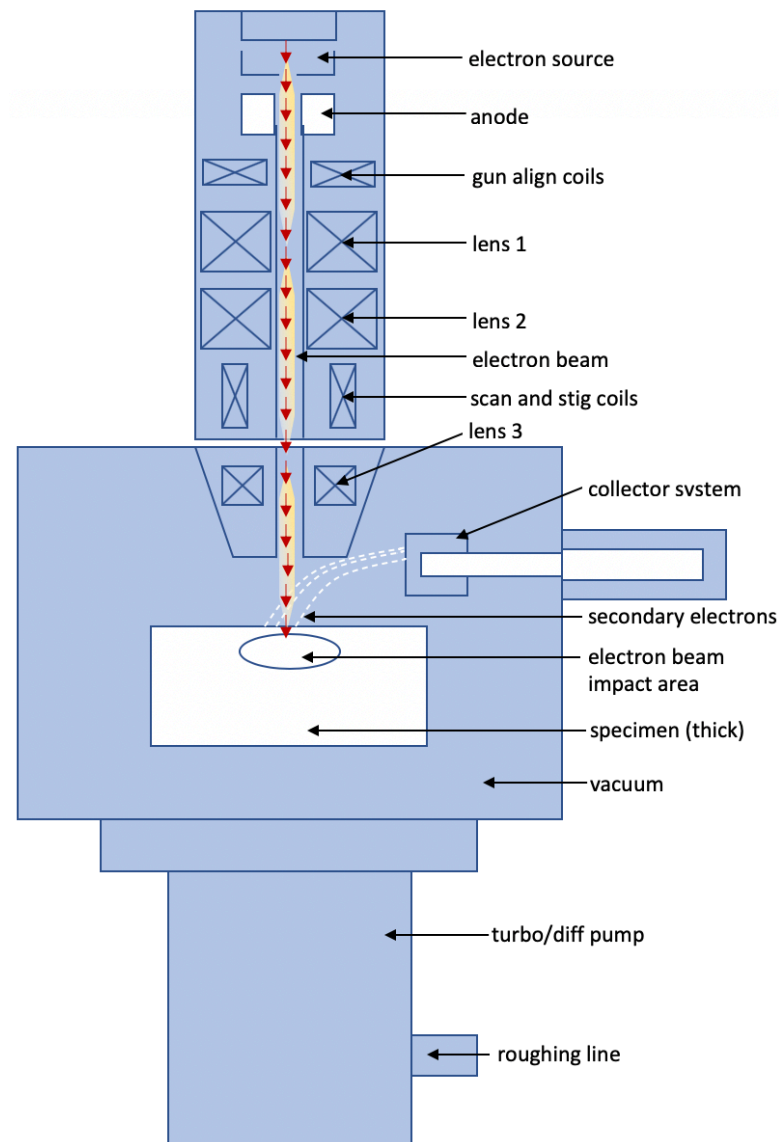


Figure 3. 9. Schematic diagram of SEM showing all its components

The interaction of the sample electron with the focused electron ray results in secondary electrons (SE), which gets easily subsumed, because these electrons have less energy. Electrons

generated closer to surface that have enough energy to break free, result in a comprehensive image of surface topography. The appearance of shadow in the microphotographs occurs because the SEs cannot escape the surface and get absorbed by the specimen. Depending on the beam accelerating voltage, the maximum depth of secondary electron emission appears to be approximately 1 nm (nanometer) for metallic compounds and 10 nm for insulating materials. Samples were aimed to be used for the benefit of secondary imaging through a conductive layer of a heavy metal such as platinum to improve secondary electron-flux, hence, enhancing the signal image. Images of SE are aimed to investigate particle dimension, shape, surface ruggedness, and fractured surfaces. The SE signal is the most commonly used signal, and it changes with the specimen surface topography in ways analogous to an airborne imagery. The boundaries of the microphotograph are bright, while the area inside is dull. The ratio of the size of the microphotograph to the scanned area of the sample gives the magnification.

Backscattered electrons (BSE) are electrons that have an energy of 50 electron volts or greater and go through numerous elastic collisions within a sample. This greater energy gives room for an even greater interaction volume, however, with a reduced spatial resolution in comparison to a SE image. On the contrary, the BE image contrast is created in relation to the average atomic number of the different phase compositions and is indicated by the distinctive brightness of the image.

X-rays are produced through the bombardment of high-energy electrons on a specimen. The electron beam ejects electrons in the inner-shell which are later replaced by electrons in the outer-shell. This substitution of electrons consequently leads to an X-ray beam discharge specific of that element. The X-ray energy level is produced in the form of peaks, commonly known as the Energy Dispersive X-ray spectrum (EDX). These peaks are shown at each energy interval as the

number of counts. The position of each peak is distinctive to a specific element and its height/intensity changes proportionally to the element's relative abundance. Peak positions are unique to a distinctive element and are labelled as k, l, or m which help in the identification of a phase through the examination of a peak's position and its relative intensity. An X-ray signal can primarily be used for: (1) plotting the respective concentration of the designated elements across a line through the analysis of a line scan, (2) analyzing spectrum for quantitative and qualitative chemical analyses, (3) X-ray imaging of element's relative concentrations and spatial distribution, and (4) helping in phase identification through the element's chemical signature. Combining criteria, such as brightness of BE signals, relation with other components, chemical composition, and morphology provides a procedure for identifying phase. The peaks and relative intensities of each element are influenced by the escalating voltage of a microscope beam. A too low voltage value makes the beam energy incapable of producing the distinct radiation. The K-line of iron, for example, is generated at 6.4 keV and so, requires almost 11 keV for sufficient electron excitation. Linearly increasing voltages within the range of 12 and 15 keV provides a reasonable space for BE and x-ray imaging. A lower voltage acceleration increases resolution and decreases the volume of interaction, but with a loss in high-energy X-ray generation efficiency with lower beam energies. This leads to a reduced absorption of X-rays and further highlights the low-energy x-rays. High-beam energies, on the other hand, cause increased absorption in the low-energy range. A voltage acceleration of 12 to 15 keV neutralizes the necessity of a sufficient beam energy for cements. Greater beam energies cause greater depth-of-field, greater resolution, and smaller beam diameter size, thus, are favorable for SE imaging.

3.3.3. ENERGY DISPERSIVE SPECTROMETRY (EDS)

The output of the X-ray microanalytical technique, Energy Dispersive

Spectroscopy contains both quantitative and qualitative chemical composition information for elements of a sample that have an atomic number more than three. X-rays produced after the electrons in the electron beam from the source encounter the atoms of the sample are recognized by the Energy Dispersive detector. The outcome of the detector is a histogram or a spectrum of intensity which shows the count i.e., number of X-rays on the y-axis and Energy on the x-axis. Characteristic X-rays', one of the two types of produced X-rays, intensities quantify the elements' concentration in the sample whereas the characteristic X-rays' energies help determine the elements composing the sample.

Outcomes from EDS analysis are of three types: map, spectrum and quantitative analysis. Map is an image that shows the varying concentration of a single element throughout a specific region of a sample. Spectrum helps find the elements making up the sample and is a plot with X-ray count rate and energies on x and y axis, respectively. The calculation of weight percentage or concentration of elements, both, major and minor in multiple phases of a sample can be done by comparing them with reference standard materials falls under quantitative analysis.

In SEM, X-ray microanalysis' spatial resolution is a few microns, reason being the interaction volume is whole between sources electrons and the sample. On the contrary, the interaction volume for generation of secondary electrons is the upper most part of the sample and for backscattered it is just the top half.

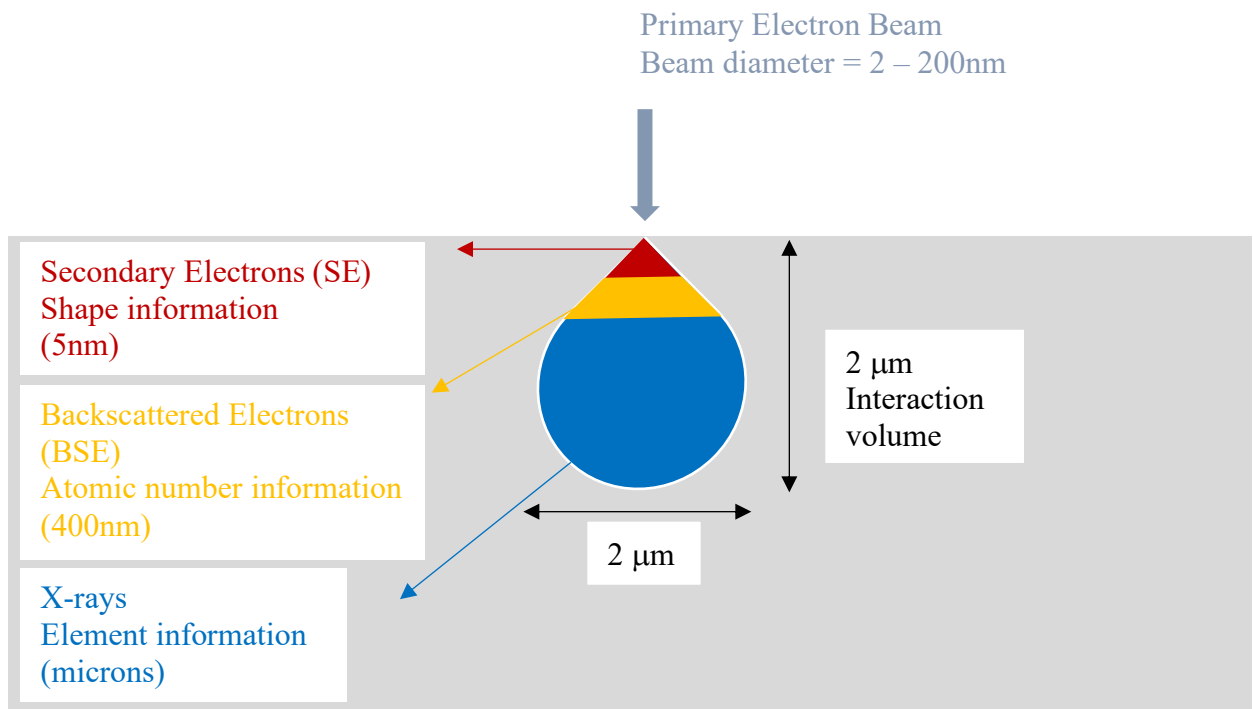


Figure 3. 10. Approximate scale of spatial resolution for SE, BSE and X-rays in SEM

Characteristic and Bremsstrahlung X-rays are the two different kinds of X-rays generated after the interaction of source electrons with the sample. The cause for the production of Bremsstrahlung X-rays is the electric field of the sample atoms' nuclei, curtailing the source electrons. The slowing down of electrons is due to inelastic scattering that takes place in the sample and X-rays are produced due to conversion of this lost energy. The process that results in Characteristic X-rays production is in two stages. First stage is the ionization where the electron beam ejects an electron in the inner shell, leaving the atom in an unstable and ionized state. Relaxation is the second stage, where an X-ray photon is emitted after a vacancy in the inner shell is filled by an electron from the outer shell which causes the atom to regain stability.

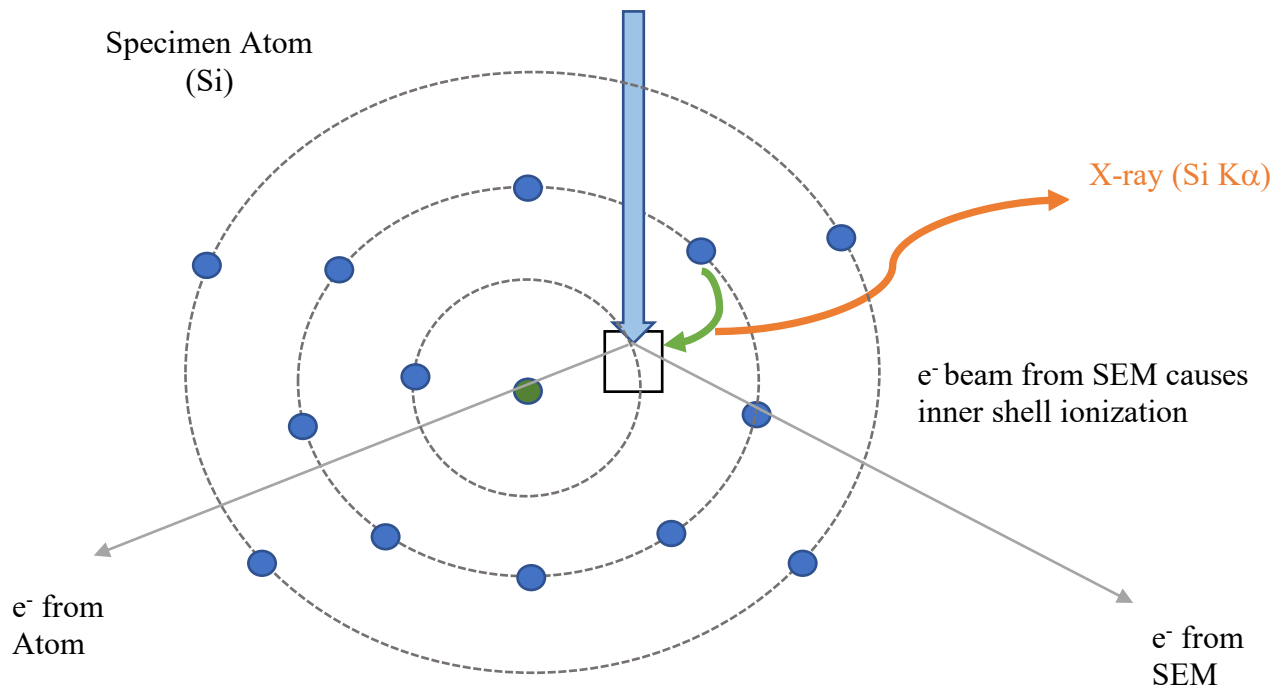


Figure 3. 11. Electron from the source removes an electron from the shell K of silicon atom. The created vacancy is filled by an electron from shell L, as a result, silicon K α X-ray is produced. The difference between the K and L shell ionization energies is the energy of the X-ray generated.

The energies required to ionize K, L and M shell increase moving from M to K shell. The energies of X-rays line for every element of M family are the lowest, K family requires the most energy followed by L family. For each element the energies for the three shells are: $K > L > M$. The relationship between atomic number of every element and its corresponding energy of Characteristic X-ray lines is defined by Moseley's Law. The law states, Z , the atomic number is proportional to the square root of the energy. According to the law on the energy dispersive spectrum (EDS), the K α X-ray line for higher atomic numbers plots on larger energies, as compared to elements with smaller atomic numbers.

The characteristic X-ray intensity or the height of the peaks is affected by a few different things like the detector that measures the X-ray spectrum, the system which produces the X-rays

and also factors related to the sample. The X-ray intensity or the height of the peaks is measured in cps (or count per second) which is the count rate or X-ray counts. The concentration or the relative abundance of the element also affects the X-ray intensity but there is not direction relation between the two. The spectrum shows prominent peaks for major elements in the sample having weight percent greater than 10 while minor elements that have weight percent between 1 to 10 or less than 1 will have short and indistinct peaks.

There are two types of X-ray microanalysis, quantitative and qualitative. Quantitative microanalysis provides the calculation of the weight percent or mass fractions of the elements while the qualitative microanalysis is the identification of elements from their respective characteristic X-ray peaks, however, it does not help in determining the relative abundance of the elements in the sample.

In a sample the elemental distribution is provided by X-ray Mapping in the form of images. Although the compositional variation in a sample is identified in back scattered electrons, the X-ray mapping is responsible for recognizing the elements causing the variation in the composition of a sample. X-ray mapping often eliminates need of quantitative point analysis by providing details that can be easily integrated and understood which in turn helps seeing the distribution of different elements in a sample. To generate the elemental X-ray maps a rectangular area is scanned side to side and top to bottom in parallel lines with an electron beam, while over a fixed counting time the amount of X-ray photons generated from every point of specified energy are recorded. For a pixel, on digital image, its brightness value is the conversion of the detected X-ray photons with specified energy at a particular point. The conversion of these photons to a brightness value generates the image. The counted number of X-rays correspond to a matrix of numerical digits which is an image's source or primary data. These counted X-rays at every point are associated to

single-band image with range of values from 0-255. The image, on the basis of look-up table can either be allocated false colors or be shown as grayscale. Multiple-band color image can be generated by integrating various single band images, corresponding to maps of various distinct elements. Discrete phases present in the scanned area can be made visible and spotted by integration of X-ray maps from various images. Phases that are composed of a union of multiple elements being mapped generates maps having composite colors.

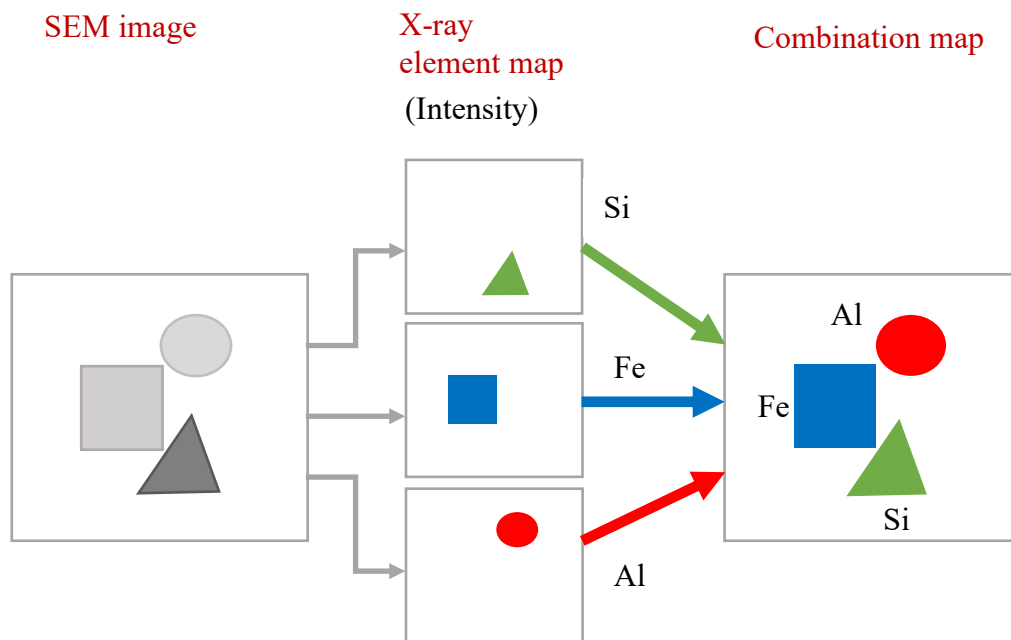


Figure 3. 12. Distribution map is put together for three elements (i.e., silicon, iron and aluminum) in a three-band image to distinguish the distinct phases mapped in the significant area

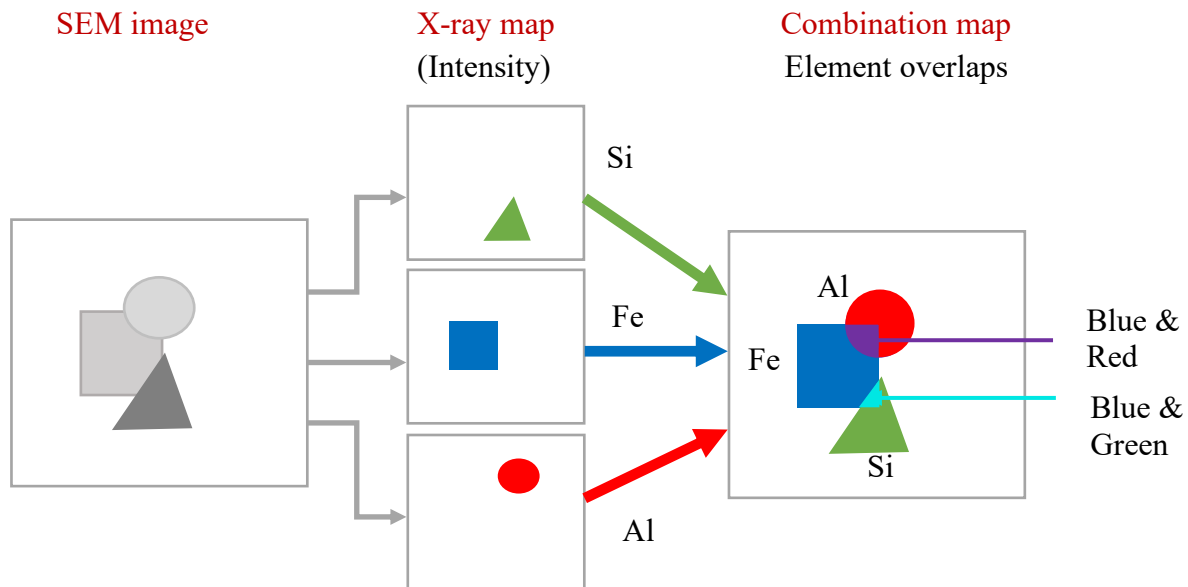


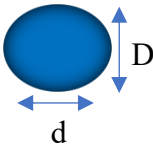
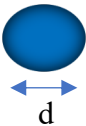
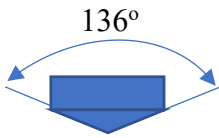
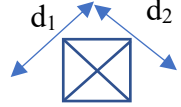
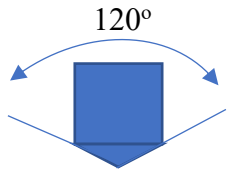


Figure 3. 13. Distribution map can be put together for three elements (i.e., silicon, iron and aluminum) in a three-band image. Primary colors are generated where distinct mixture of elements is present in the sample in distinct phases

3.4. HARDNESS TEST

The capability of a substance to resist plastic deformation is the commonly known definition of hardness; however, the dictionary definition of hardness in Metallurgy is a material's resistance to indentation. The primary reason for performing a hardness test on a material is to learn its appropriateness for a specific application or its suitability for the certain treatment to which it has been exposed. The hardness test is a preferred mechanical test for inspection of materials and their properties because it is relatively non destructible. The three scales (macro, micro and nano scale corresponding to the displacement induced on the sample due to the force applied), define the hardness measurement. Macro-hardness is a faster and simpler testing method which is used to attain the mechanical properties for bulk materials. The three most widely used

test techniques that fall under macro-hardness are: Rockwell, Brinell and Vickers. The loads applied in macro-hardness on the indenter are greater than 1 kg and mostly used to test heavy gauge materials in dies, sheet materials and tools mostly to perform quality check on surface treatment processes. The need for all these various hardness tests is because of the broad spectrum of hardness ranging from hard and brittle ceramics to soft polymers.

Table 3. 1. The geometrical shape of the indenters and the indent as well as the range of applied loads for the different types of hardness testing methods.

Test	Indenter	Side View	Top View	Load
Brinell	10-mm steel or tungsten-carbide ball			500 kg
				1500 kg
				3000 kg
Vickers	Diamond Pyramid			1 – 120 kg < 1 kg (micro hardness)
Rockwell <div><div>A</div><div>C</div><div>D</div><div>B</div><div>F</div><div>G</div><div>E</div><div></div></div>	Diamond cone			
				60 kg
				150 kg
		100 kg		
	0.06 in diameter steel ball indenter			100 kg
				60 kg
				150 kg
	0.12 in diameter steel ball indenter			100 kg

3.4.1 MICRO-HARDNESS

The appropriate method to obtain the hardness value of a sample on microscopic scale is micro-hardness or micro-indentation hardness testing. Conventional mechanical characterization of rock requires retrieving core plugs which can be technically demanding and costly or even impossible (Liu et al., 2016; Xu et al., 2018). For materials that are non-homogenous, multi-phase, susceptible to fracture or have a fine microstructure, hardness values obtained from macro-hardness testing is irregular and does not recognize true individual surface characteristics. For such materials and samples micro-hardness method is most suitable. Knoop and Vickers are the two different types of indenter used for micro-hardness testing, both made of diamond. Knoop indenter is a rhombohedral, elongated in shape, while Vickers has a square base with a right pyramid. For both the indenters the load applied to make an indent ranges from 1g to 1 kg for 10 – 15 seconds and an optical microscope is normally used to measure the indentations.

In the micro-hardness testing process before a diamond indenter was used to make an indent, the sample was metallographically mounted and polished. Typically, the dimensions of the specimen are approximately 1 inch by 1 inch with $\frac{1}{2}$ inch in thickness so they can fit the sample stage. The cement rock samples of the required dimensions were cut using diamond bandsaw. The cut samples were mounted in a resin puck to get reliable analytical micro-hardness values. The epoxy resin and epoxy harder mixture were 2:1 ratio respectively and allowed to cure at room temperature for 9 hours. The quality of the micro-hardness values highly depends on the surface of the sample. The specimen surface was grinded and polished by abrasion material of varying grit sizes (i.e., ANSI grit 240, 400, 600 and 800) using SBT model 900 grinder and polisher. A rough surface is unfavorable in identifying the diamond shaped indentation hence minimizing the validity

of the indentation data. For accurate micro-hardness values the specimen were perpendicular to the indenter tip and the micro-hardness testing equipment was isolated from any vibrations to ensure the testing conditions were vibration free. The polished cement-rock specimens, before and after curing of epoxy can be seen in Figure 3.14.

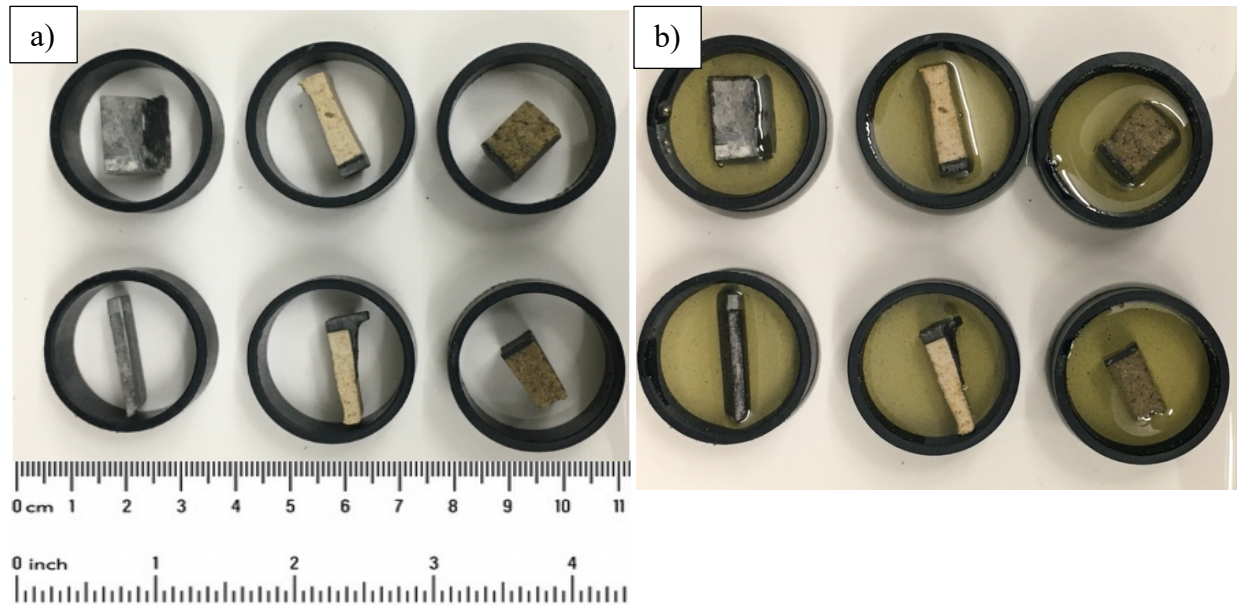


Figure 3. 14. Micro-hardness specimen a) before epoxy resin b) after epoxy curing

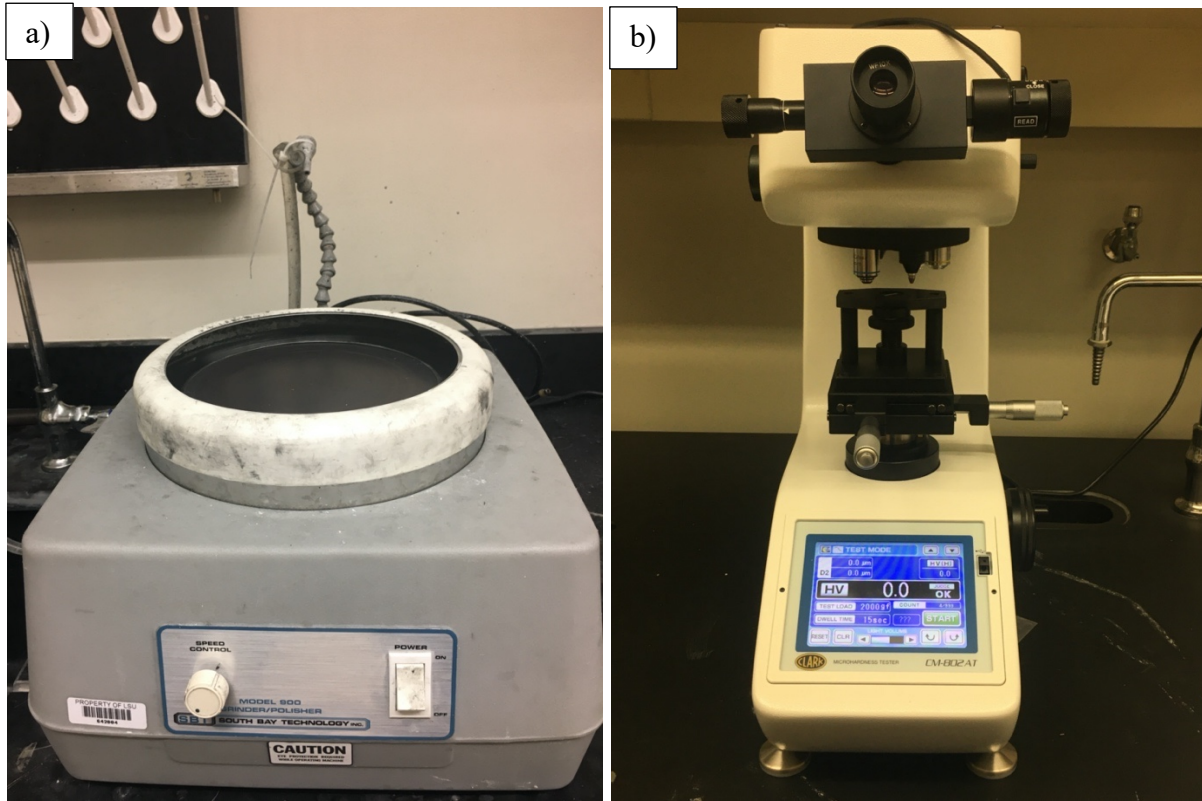


Figure 3. 15. Equipment used in micro-hardness testing a) Grinder and polisher b) Micro-hardness tester

The micro-hardness tester CM-802 AT was used to determine the hardness values. The Vickers diamond indenter lowered at a rate of less than 1 mm per minute produced an indentation on the surface of the specimen by application of a selected load. The time for which the load is applied is the dwell time, after which the indenter withdraws from the specimen leaving a square shaped indent. To obtain a micro-hardness value the measured lengths in μm of the resultant indentation i.e., two diagonals, are converted to hardness values using equations. The Vickers hardness (H_v) values were acquired using the following equation.

$$H_v = 0.1891 * \{F(N) / d_1(\text{mm}) * d_2(\text{mm})\} \quad (3)$$

where,

F is the load applied by the indenter to make an indent

d_1 and d_2 are the two diagonal lengths

4. RESULTS AND DISCUSSION

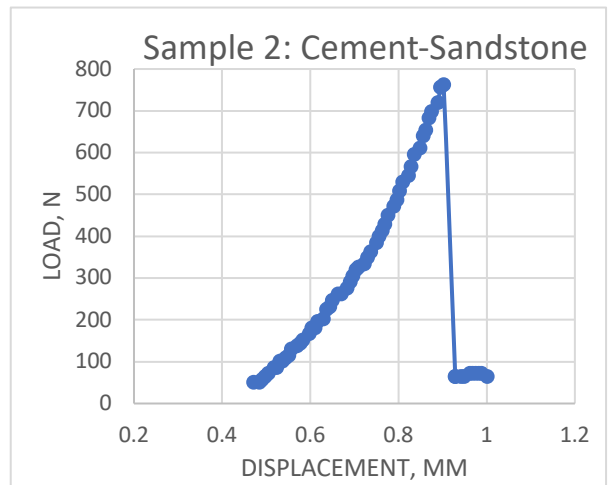
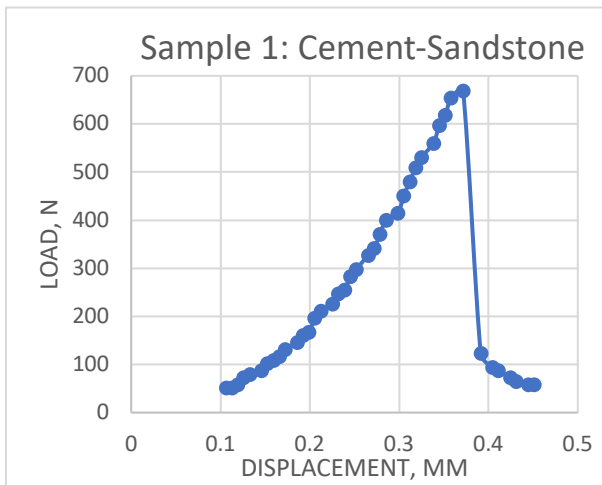
4.1.SCBT FOR FRACTURE TOUGHNESS CHARACTERIZATION

This section highlights the mode I fracture toughness for three kinds of heterogenous samples i.e., cement-sandstone, cement-shale and cement limestone, calculated using three-point bend test. The specimen geometry and peak load values, obtained from the load-displacement curves (Figure 4.1), were used in the Chong and Kuruppu, 1984, equation to calculate the fracture toughness.

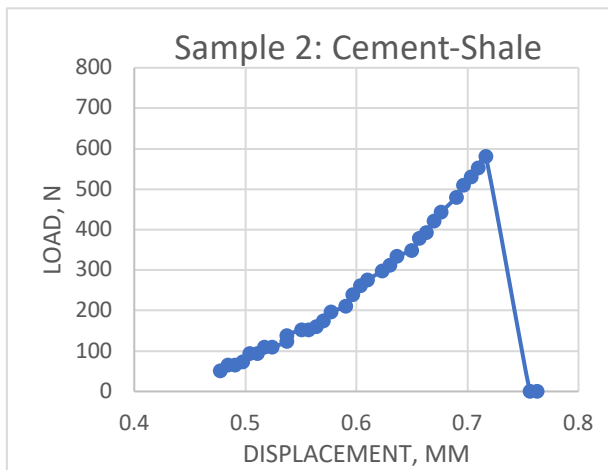
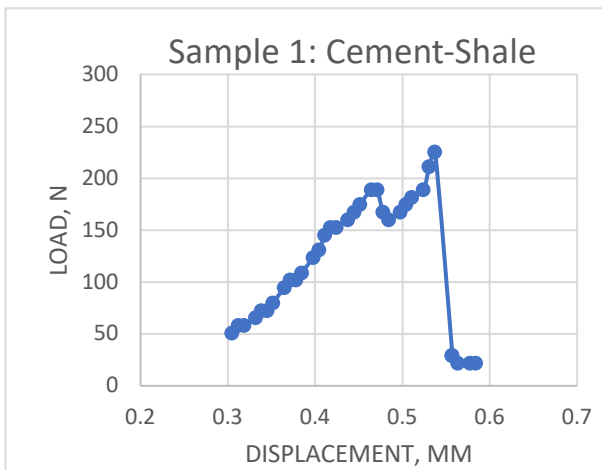
The fracture toughness recorded for the cement-sandstone was higher than the fracture toughness of cement-shale and cement-limestone samples. The range of for cement-sandstone fracture toughness is 448.78 to 512 kPa \sqrt{m} as indicated in Table 4.1. The difference in the two peak load values, 669.12N and 763.76N, that fractured the cement-sandstone samples is insignificant while there is a substantial difference in the peak loads that fractured the two cement-shale samples, 225.47N and 581.85N. The contrasting peak loads recorded for cement-shale result in a significant variation and wide range of the fracture toughness i.e., 151.22 to 390.25 kPa \sqrt{m} . The peak load for cement-limestone was in between the cement-sandstone and cement-shale with a fracture toughness of 263 kPa \sqrt{m} .

Table 4. 1. Fracture toughness of bi-material samples

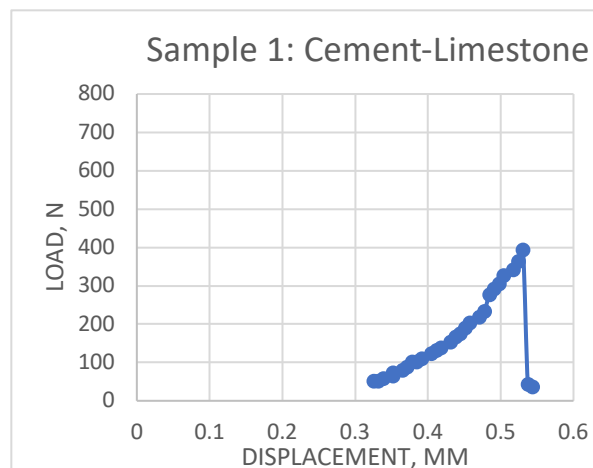
Bi-material sample	Maximum load (N)	Fracture toughness (kPa \sqrt{m})
Sample 1 Cement-sandstone	669.12	448.78
Sample 2 Cement-Sandstone	763.67	512.2
Sample 1 Cement-Shale	225.47	151.22
Sample 2 Cement-Shale	581.85	390.25
Sample 1 Cement-Limestone	392.75	263.42



a)



b)



c)

Figure 4. 1. Load-displacement curve for bi-material a) cement-sandstone b) cement-shale c) cement-limestone

4.2.SEM IMAGES AND ANALYSIS

This section reports the SEM results that includes: live maps for phases analysis, SEM backscattered images, EDS elemental maps, distribution maps of fundamental elements, EDS elemental spectrum of dominant phases and quantification results of cement, shale, limestone, sandstone and cement-rock interfaces.

4.2.1. CEMENT

Portland cement comprises of silica dominant compounds and the products of calcium hydration reaction. Calcium silicate hydrate (C-S-H), a non-porous semicrystalline composite, is one of the hydration reaction products of calcium. It is a significant phase within hydrated Portland cement and is majority of the volume as shown in SEM live map (Figure 4.4a). The C-S-H gel has large surface area and controls the strength of hydrated cement. The second prominent product of calcium hydration reaction is calcium hydroxide also known as portlandite, makes up around 25 percent of the hydrated cement paste. This calcium hydroxide has crystals that form hexagonal plates of medium shape that can be inter grown with the first product of hydration, C-S-H (Taylor, 1997). Aluminoferrite is the third major mineral group in hydrated Portland cement.

Ettringite is the primary mineral of the aluminoferrite group and accounts for 20 percent of the volume. Ettringite developed during the initial stages of the hydration process exist in the shape of hexagonal rods and can be seen in the SEM backscattered micrograph at a magnification of 2000x (Figure 4.4b), along with the poor crystallinity and irregular small grains of C-S-H. The SEM EDS elemental map and distribution maps of fundamental elements (Figure 4.4c and 4.4d, respectively) aid in the phase analyses of the hydrated Portland cement. The SEM EDS elemental spectrum and quantification results (Figure 4.5 and Figure 4.6) show the elemental composition, in terms of weight and atomic percent, of the two phases, that make the majority of the volume of

the matrix i.e., calcium, oxygen and calcium, silicon, oxygen rich phases. The BSE images of hydrated Portland cement obtained at different magnifications (Figure 4.7) show the distinct phases of the hydration process along with fractures, porosities and residual cement. Portlandite, the short networked fibrous structure of C-S-H and the long crystals of ettringite are also identified in the BSE image obtained at 20um resolution.

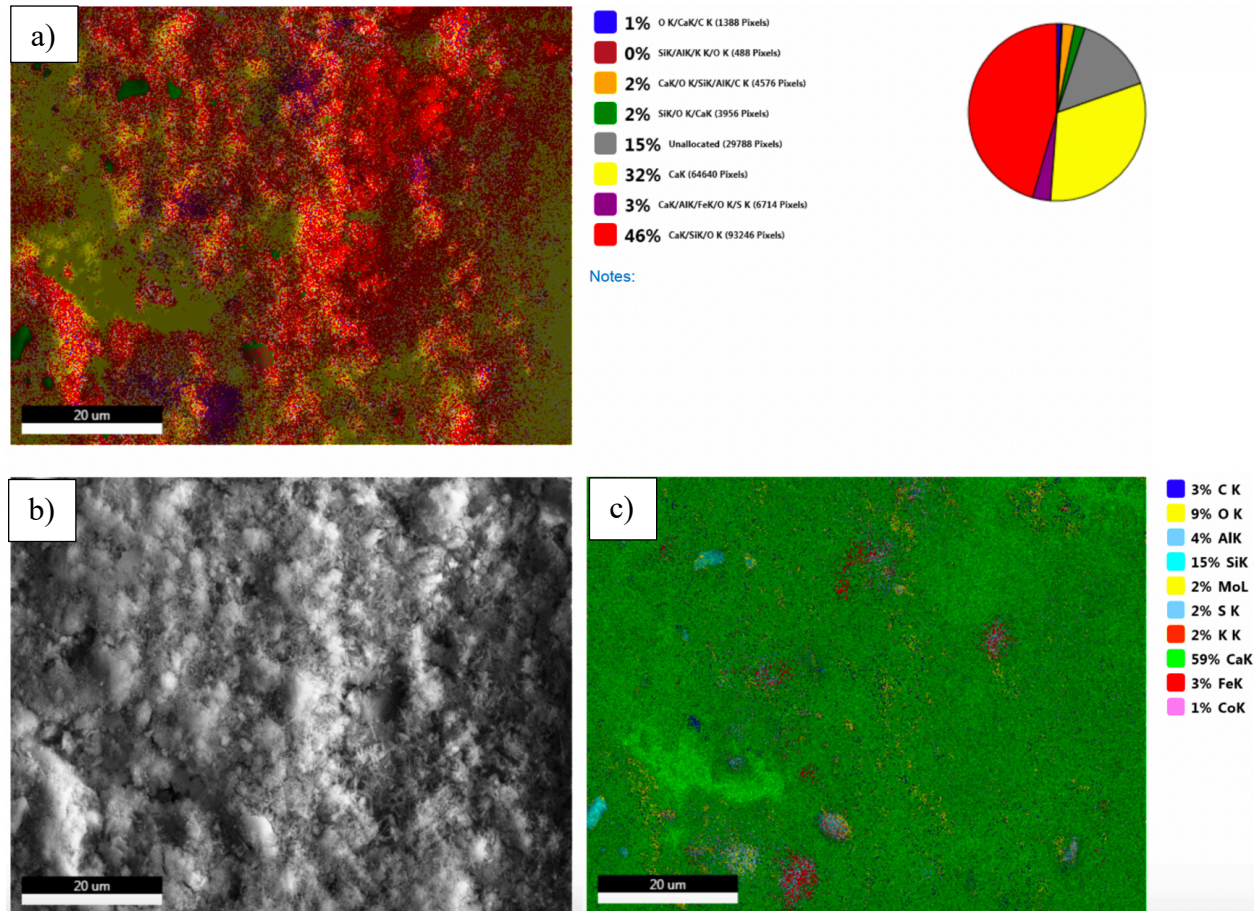


(figure cont'd)

(figure cont'd)

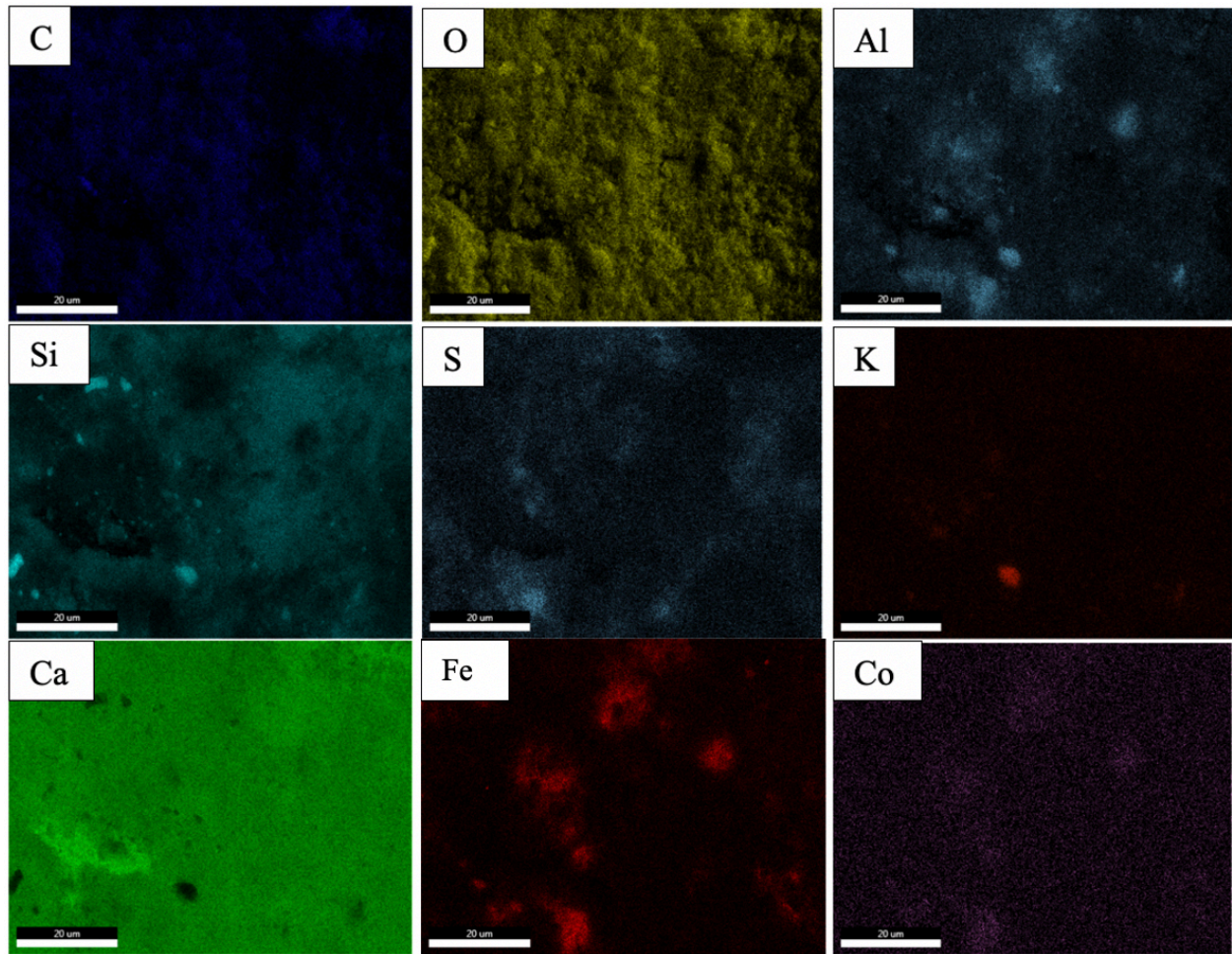
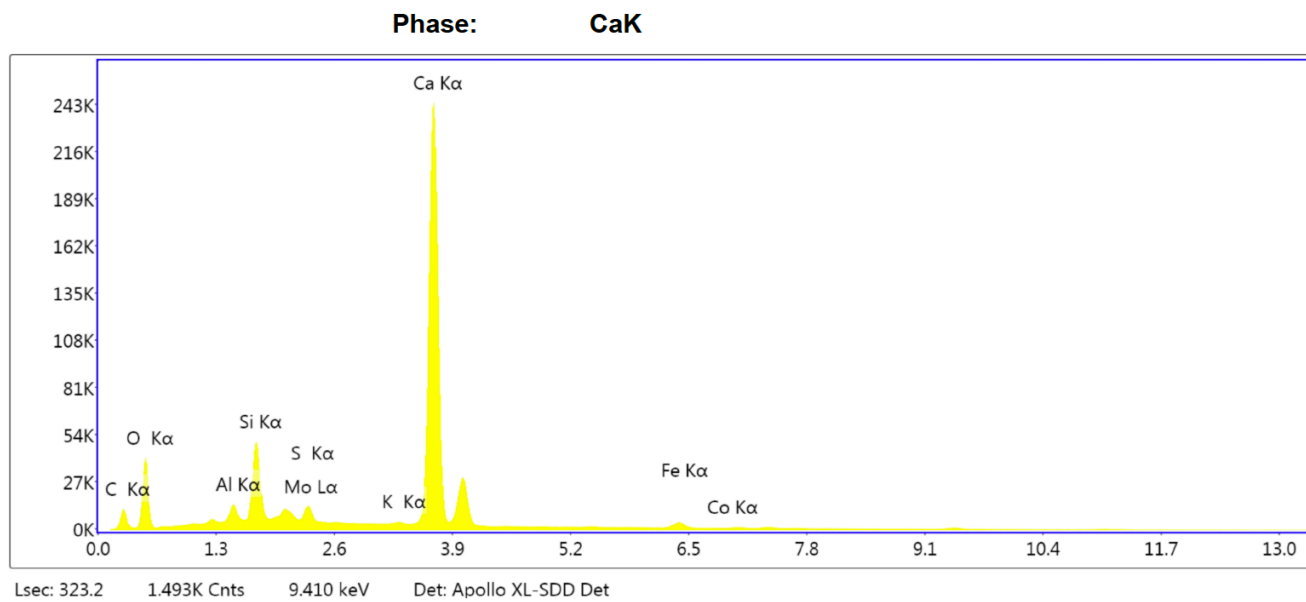
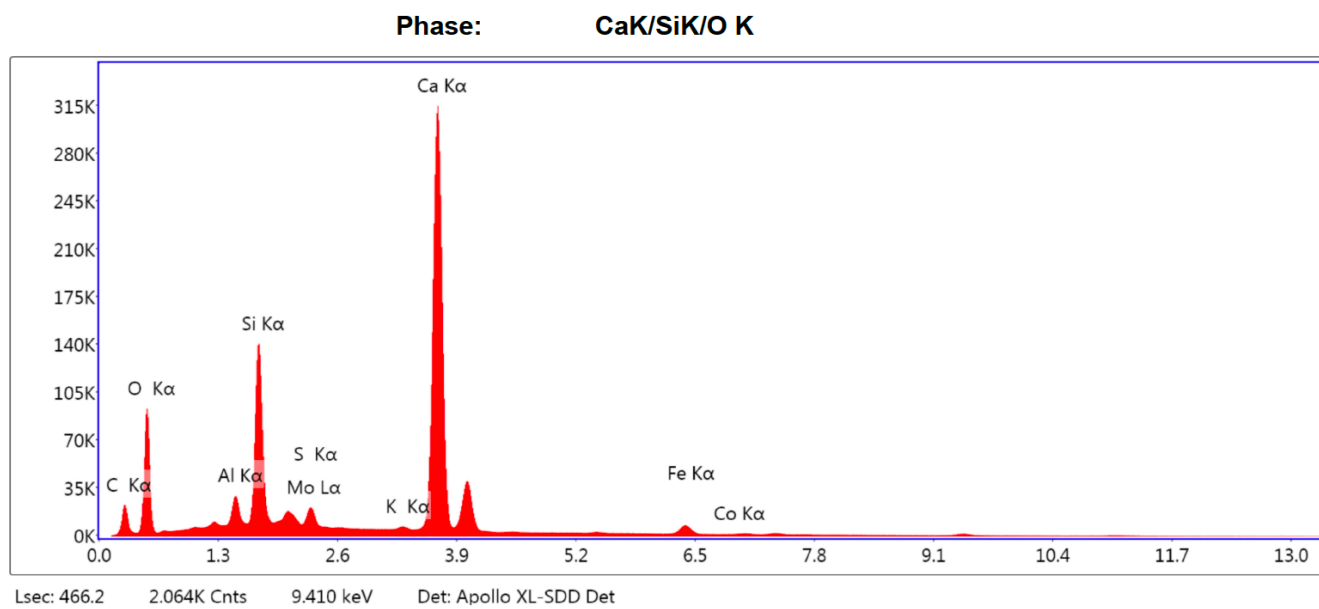


Figure 4. 2. Pure cement a) Live map of pure cement at 2000x magnification obtained using FEI Quanta 3D FEG dual beam FIB/SEM at 20 kV b) Backscattered Electrons (BSE) micrograph at 2000x magnification c) EDS elemental map d) Distribution maps of fundamental elements



Element	Weight %	Atomic %	Net Int.
C K	3.65	8.60	204.80
O K	21.59	38.20	898.70
AlK	0.88	0.92	190.10
SiK	5.30	5.34	1269.70
MoL	2.48	0.73	274.80
S K	0.00	0.00	0.00
K K	0.18	0.13	33.60
CaK	63.62	44.92	8752.10
FeK	2.13	1.08	139.80
CoK	0.18	0.08	10.00

Figure 4. 3. Ca dominant phase in cement a) SEM EDS elemental spectrum b) quantification results



Element	Weight %	Atomic %	Net Int.
C K	4.97	10.73	272.60
O K	26.85	43.52	1404.70
AlK	1.51	1.45	374.00
SiK	9.71	8.96	2618.30
MoL	2.74	0.74	330.60
S K	0.00	0.00	0.00
K K	0.30	0.20	60.70
CaK	51.18	33.12	7869.30
FeK	2.59	1.20	192.90
CoK	0.15	0.07	9.80

Figure 4. 4. Ca, Si and O dominant phase in cement a) SEM EDS elemental spectrum b) quantification results

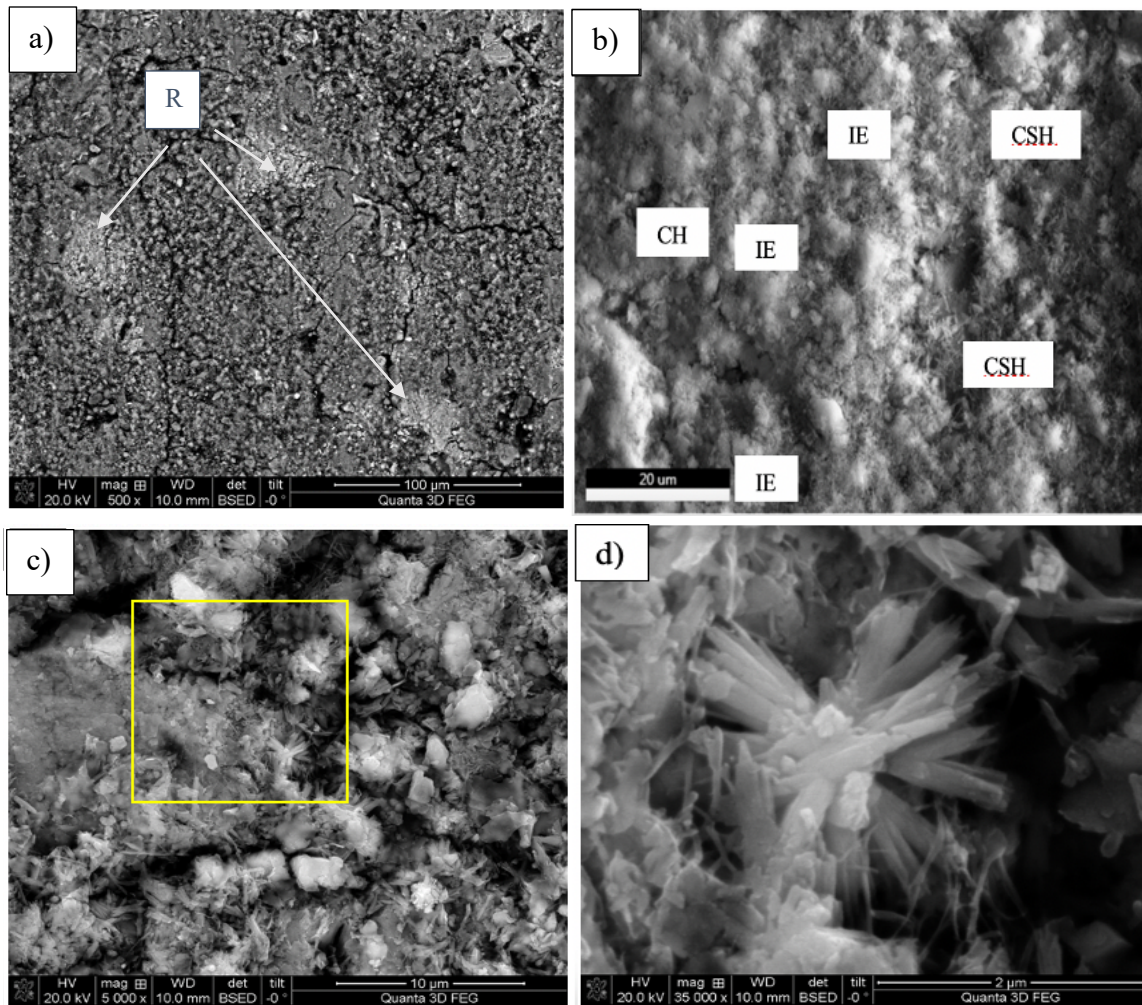


Figure 4. 5. BSE micrographs of cement obtained at a) 500x b) 2000 x c) 5000x (d) 35000x magnification. The short networked fibrous structure of C-S-H and needle like structure of ettringite can be seen at different resolutions. IE is Iron Ettringite. CH is Portlandite. R is residual cement

4.2.2. SHALE

Shales present even in the same location can have varying microstructure and composition, and are therefore referred to as naturally occurring multiphase composites. The primary minerals that compose shale rock are divided into three main groups based on the microstructure of the minerals. The first group, tectosilicates, includes quartz, K-feldspar and plagioclase while the phyllosilicates or clay category mainly comprises of illite, chlorite, kaolinite, chlorite and smectite. Dolomite, calcite, pyrite, hematite, siderite, ankerite and halite fall under the carbonates and other

minerals group. The clay minerals play a vital role in determining shale properties (Du et al., 2017a). The mineralogical composition, including clay content, quartz and feldspar percentage, carbonates, total organic content and porosity proportions as a percentage of total mineral content from previous studies (Bourg, 2015; Amann et al., 2013; Bai et al., 2013; Busch et al., 2008; Chalmers et al., 2012; Josh et al., 2012; Swift et al., 2014; Nelson, 2009) can be seen in Table 4.2. The results show that shales with lower clay content have higher total organic content and act as a source of hydrocarbon whereas shale with higher clay content have lower total organic content and have better sealing quality.

Table 4. 2. Mineralogical composition, total organic content and porosity percentage of two different kinds of shale from previous studies (Bourg, 2015; Amann et al., 2013; Bai et al., 2013; Busch et al., 2008; Chalmers et al., 2012; Josh et al., 2012; Swift et al., 2014; Nelson, 2009)

Shale Types	Tectosilicates %	Clay/ Phyllosilicates %	Carbonate and Other Minerals %	Total Organic Content %	Porosity %
Sealing shale- Caprock	33.6	52.6	12.1	1.6	18.5
Brittle shale- Hydrocarbon source rock	43.7	25.4	25.7	4.7	5.7

The mineralogical composition governs shale rock's susceptibility to distinct fracture fluids hence have a great impact on the mechanical characteristics of shale. The SEM live map (Figure 4.8a) shows the dominant phases present in shale while the microstructure of shale can be observed in the SEM BSE micrograph (Figure 4.8b). The EDS with elemental map and distribution maps of fundamental elements (Figure 4.8c and Figure 4.8d respectively), help identify the minerals present in the area of interest more accurately by showing the chemical concentration and distribution in the shale rock. Some of the minerals present in shale can be identified from the BSE micrograph, alone, examples being, larger size grains are tectosilicates i.e., quarts and K-feldspar, and carbonates, while the smaller amorphous minerals are clay particles. Besides the BSE

micrograph, distribution maps elements provide very useful information. The silicon distribution map indicates quartz and K-feldspar as bright (high concentration), big and clean spots, while the calcium distribution map shows the distribution of elongated particles in shale as mainly dolomite. The combination of oxygen sulphur and sodium maps indicates the locations of porosity in shale since oxygen is present in the composition of most of the minerals in sedimentary rocks with pyrite and halite as exception. Since the presence of both the elements, sulphur and sodium is negligible, the absence of oxygen in the oxygen map i.e., black pixels, indicates porosity, fractures or kerogen. The iron map in shale indicates iron rich mineral which was recognized in spot analysis as hematite. The combination of magnesium, aluminum and potassium maps show the location of phyllosilicates or clay minerals between the larger quartz, K-feldspar and dolomite grains.

The elemental percentage composition of three major phases present in shale and their relative peak intensities can be found in EDS elemental spectrum and quantification results (Figure 4.9, 4.10 and 4.11). The different minerals identified in the formation of shale are pointed out in BSE micrograph (Figure 4.12). The shale is identified as brittle shale based on the mineralogical composition, comprised predominantly of tectosilicates, more than 45 percent with lesser amount of clay and other oxide minerals.

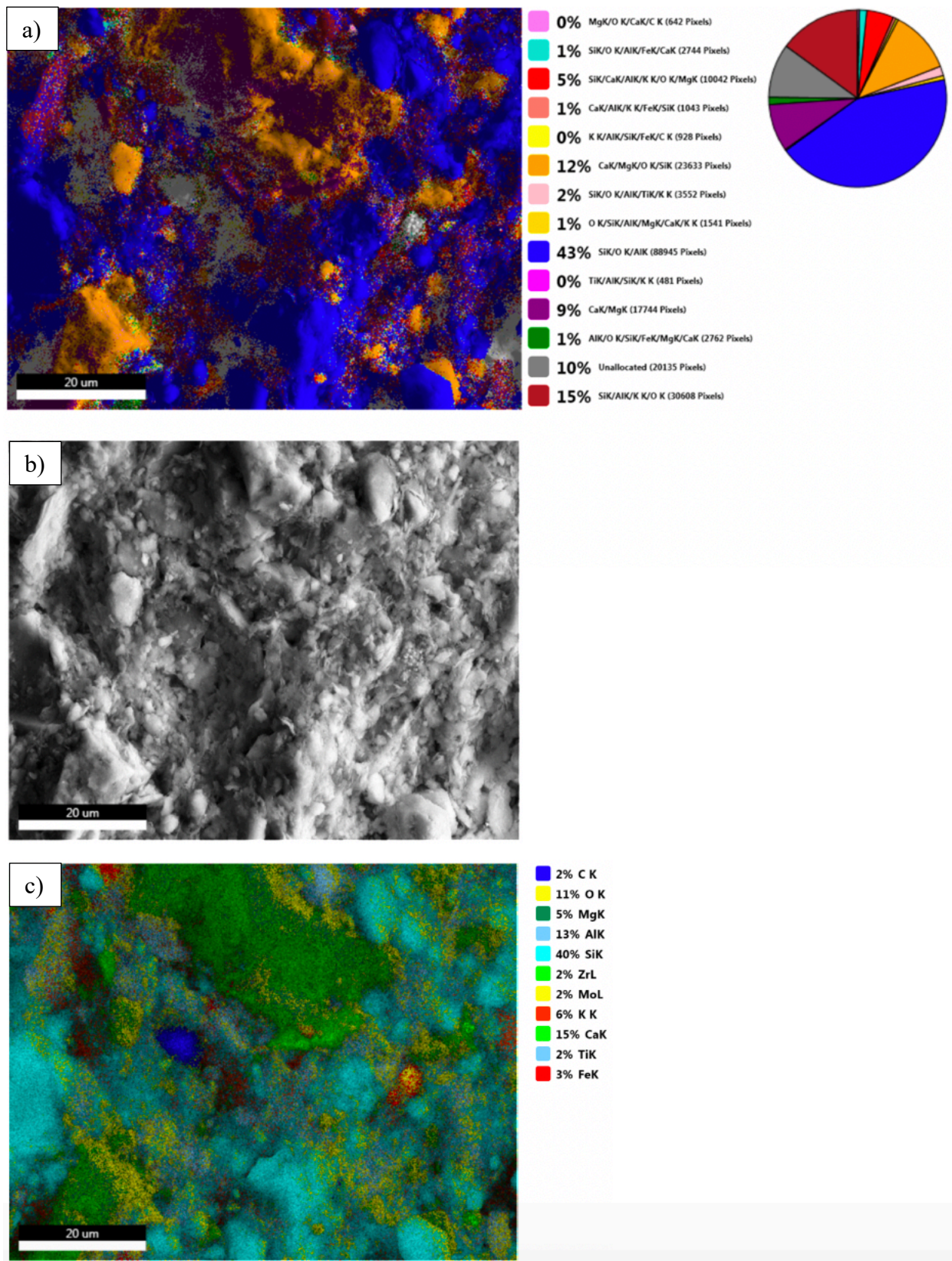


(figure cont'd)

(figure cont'd)

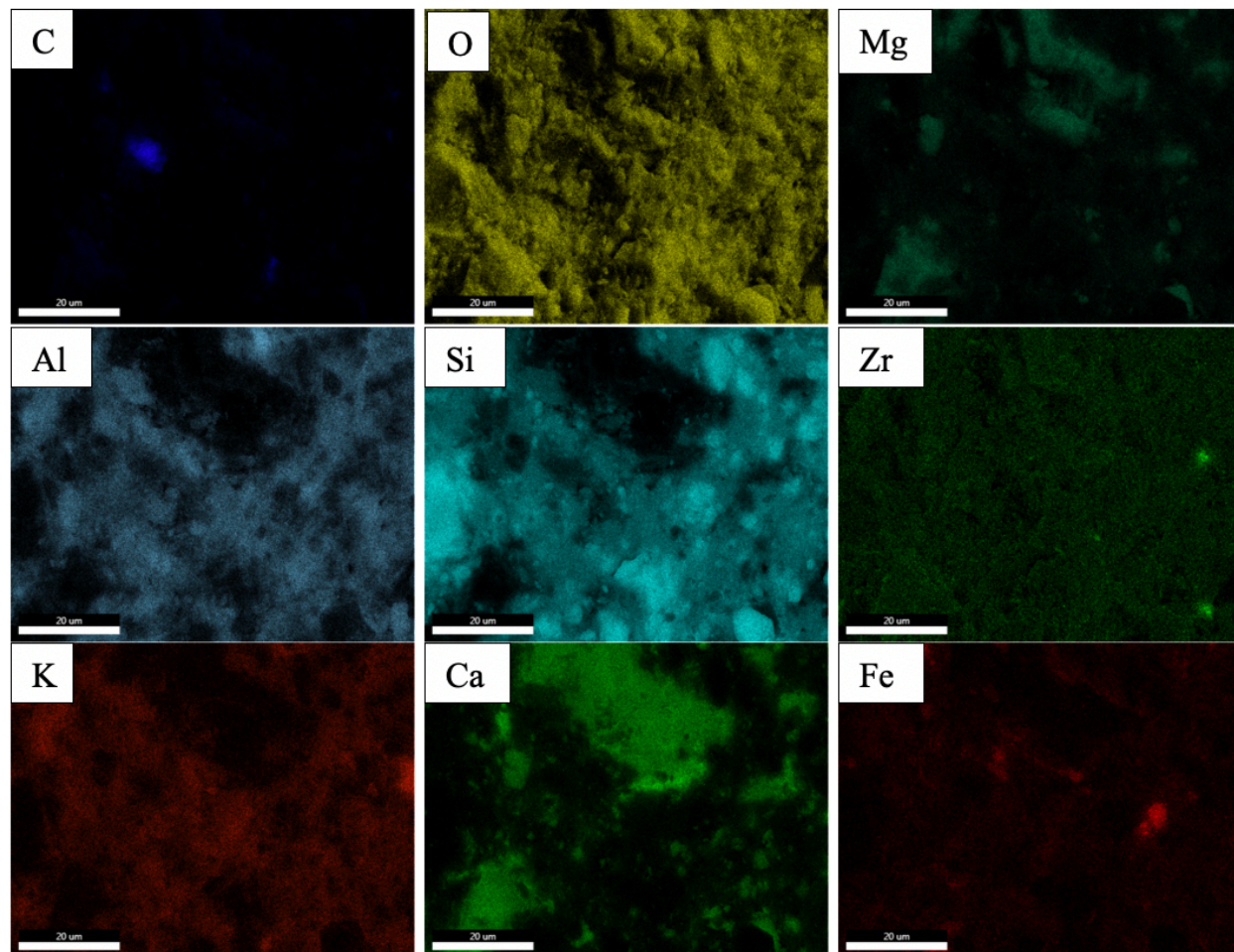
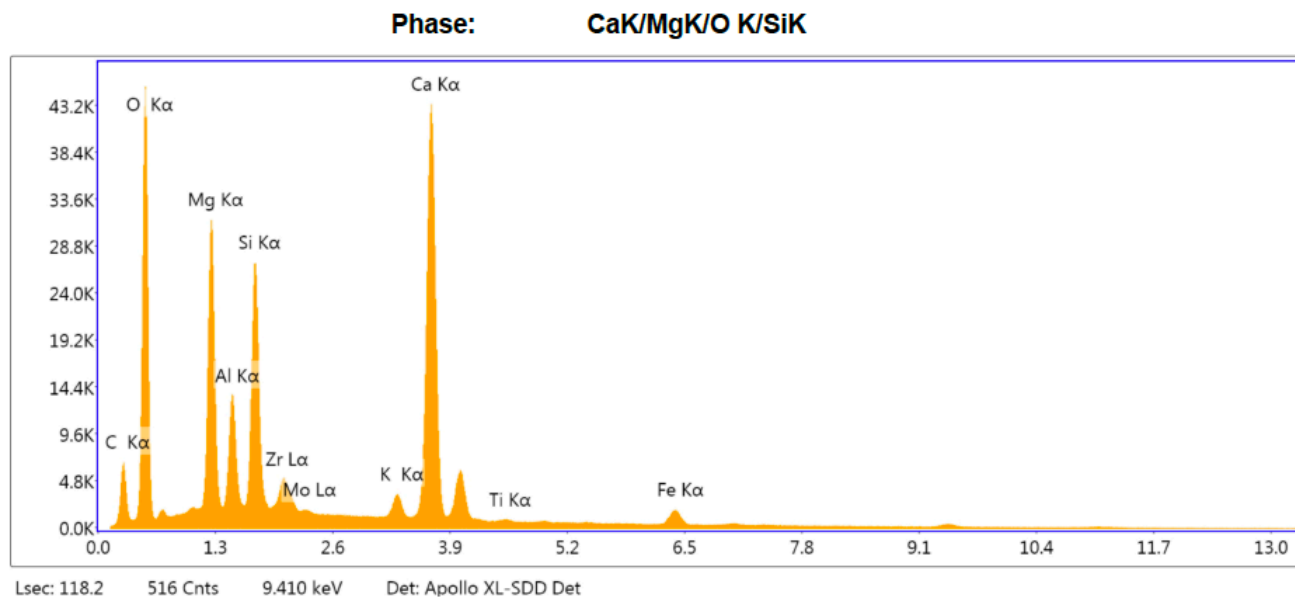
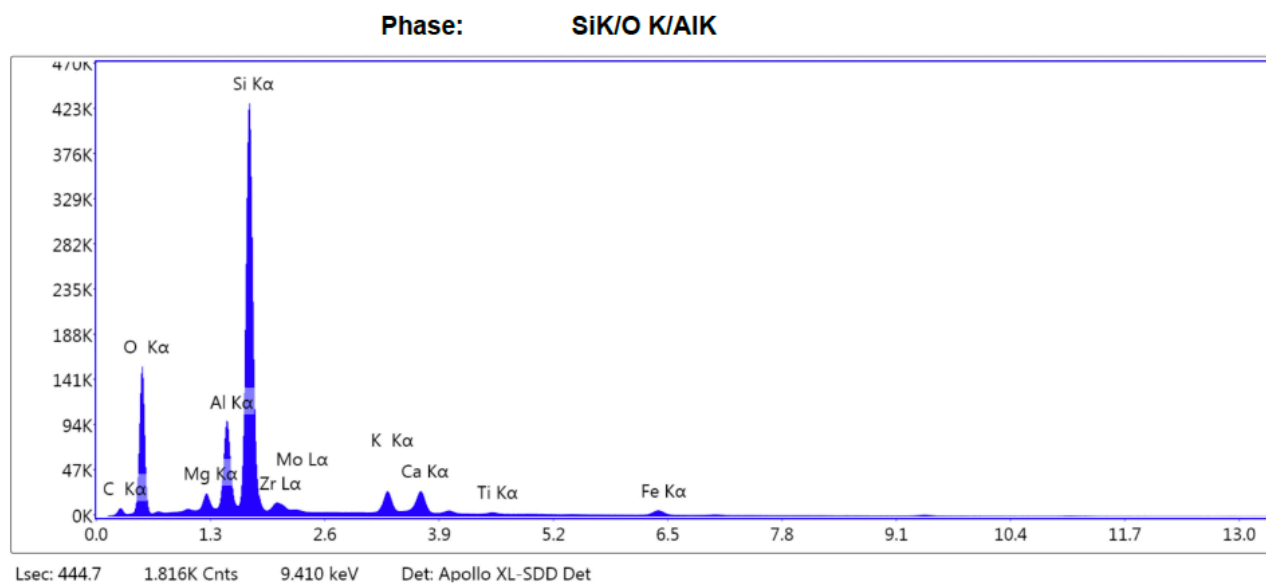


Figure 4. 6. Pure shale a) Live map at 2000x magnification obtained using FEI Quanta 3D FEG dual beam FIB/SEM at 20 kV b) Backscattered Electrons (BSE) micrograph at 2000x magnification c) EDS elemental map d) Distribution maps of fundamental elements



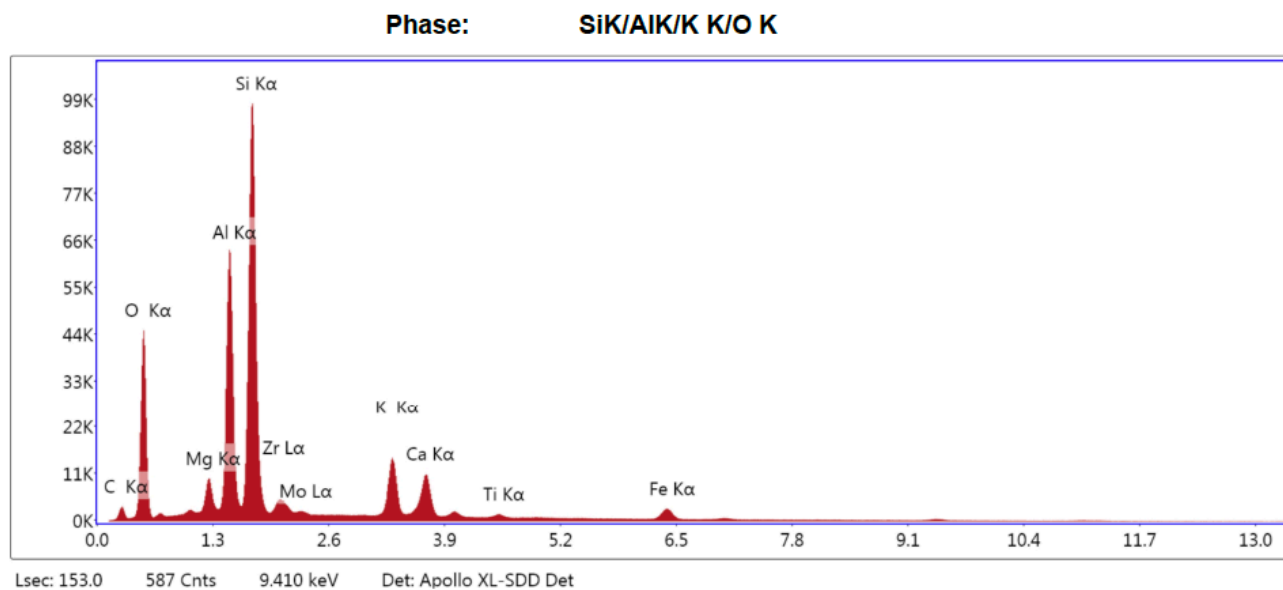
Element	Weight %	Atomic %	Net Int.
C K	7.03	12.84	330.80
O K	38.09	52.24	2683.40
MgK	9.21	8.31	2085.90
AlK	3.76	3.05	880.40
SiK	7.84	6.13	1996.60
ZrL	2.49	0.60	287.30
MoL	0.22	0.05	25.90
K K	1.25	0.70	237.50
CaK	27.40	15.00	4191.70
TiK	0.27	0.13	34.10
FeK	2.43	0.96	184.40

Figure 4. 7. Ca, Mg, O and Si dominant phase in shale a) SEM EDS elemental spectrum b) quantification results



Element	Weight %	Atomic %	Net Int.
C K	3.83	7.22	88.90
O K	32.54	46.10	2415.00
MgK	1.24	1.16	260.80
AlK	8.15	6.85	1855.40
SiK	38.84	31.34	8741.40
ZrL	2.60	0.65	213.80
MoL	0.54	0.13	45.70
K K	4.32	2.51	615.10
CaK	5.02	2.84	613.30
TiK	0.49	0.23	51.90
FeK	2.43	0.98	155.60

Figure 4. 8. Si, O and Al dominant phase in shale a) SEM EDS elemental spectrum b) quantification results



Element	Weight %	Atomic %	Net Int.
C K	4.23	8.21	104.70
O K	29.46	42.87	2044.80
MgK	1.76	1.69	362.70
AlK	15.60	13.46	3463.30
SiK	28.01	23.21	5883.50
ZrL	2.69	0.69	225.40
MoL	0.50	0.12	42.70
K K	7.15	4.26	1022.70
CaK	6.27	3.64	760.90
TiK	0.69	0.33	72.20
FeK	3.63	1.51	230.50

Figure 4. 9. Si, Al, K and O dominant phase in shale a) SEM EDS elemental spectrum b) quantification results

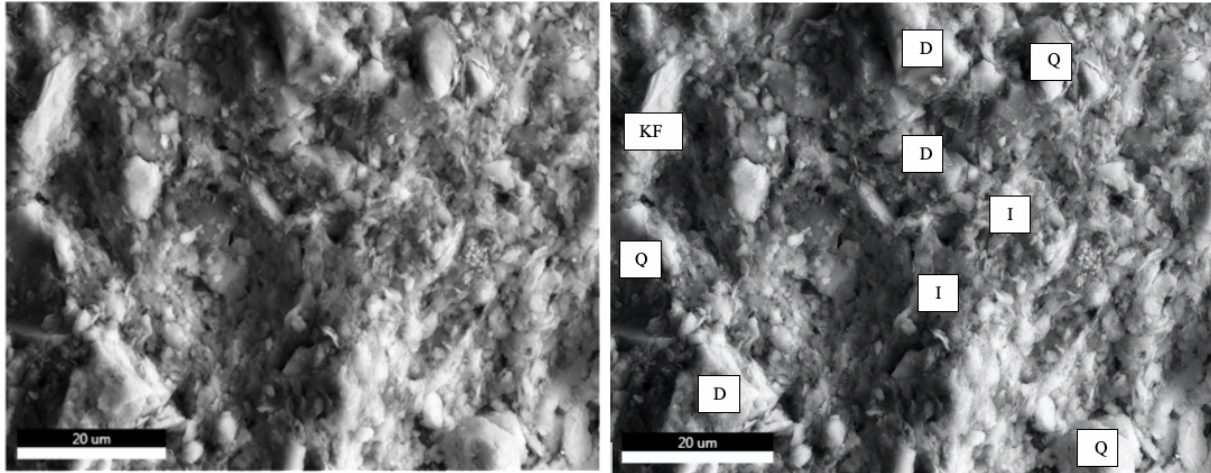


Figure 4. 10. SEM BSE image of pure shale at 2000x magnification. I is Illite (phyllosilicates i.e., clays). KF is K-Feldspar (tectosilicates). D is Dolomite. Q is quartz

4.2.3. LIMESTONE

The SEM Live map (Figure 4.13a) of limestone shows only one major phase, that makes up limestone, comprising of elements: calcium, oxygen and carbon. The EDS elemental map, (Figure 4.13c) of the same location as the BSE image (Figure 4.13b), identifies the percentage of calcium to be almost 80 % of the total elements present. The distribution map of fundamental elements (Figure 4.13d) reveals the spread of calcium, oxygen and carbon over the entire limestone with traces of silicon, potassium and chlorine. The tallest peak present in EDS spectrum of the only dominant phase in limestone is of calcium followed by oxygen and silicon (Figure 4.14a), the high concentration of these elements is confirmed by the quantitative results (Figure 4.14b). The microstructure of calcium carbonate can be seen in the SEM micrograph obtained at 2000x magnification (Figure 4.15), with traces of silica.

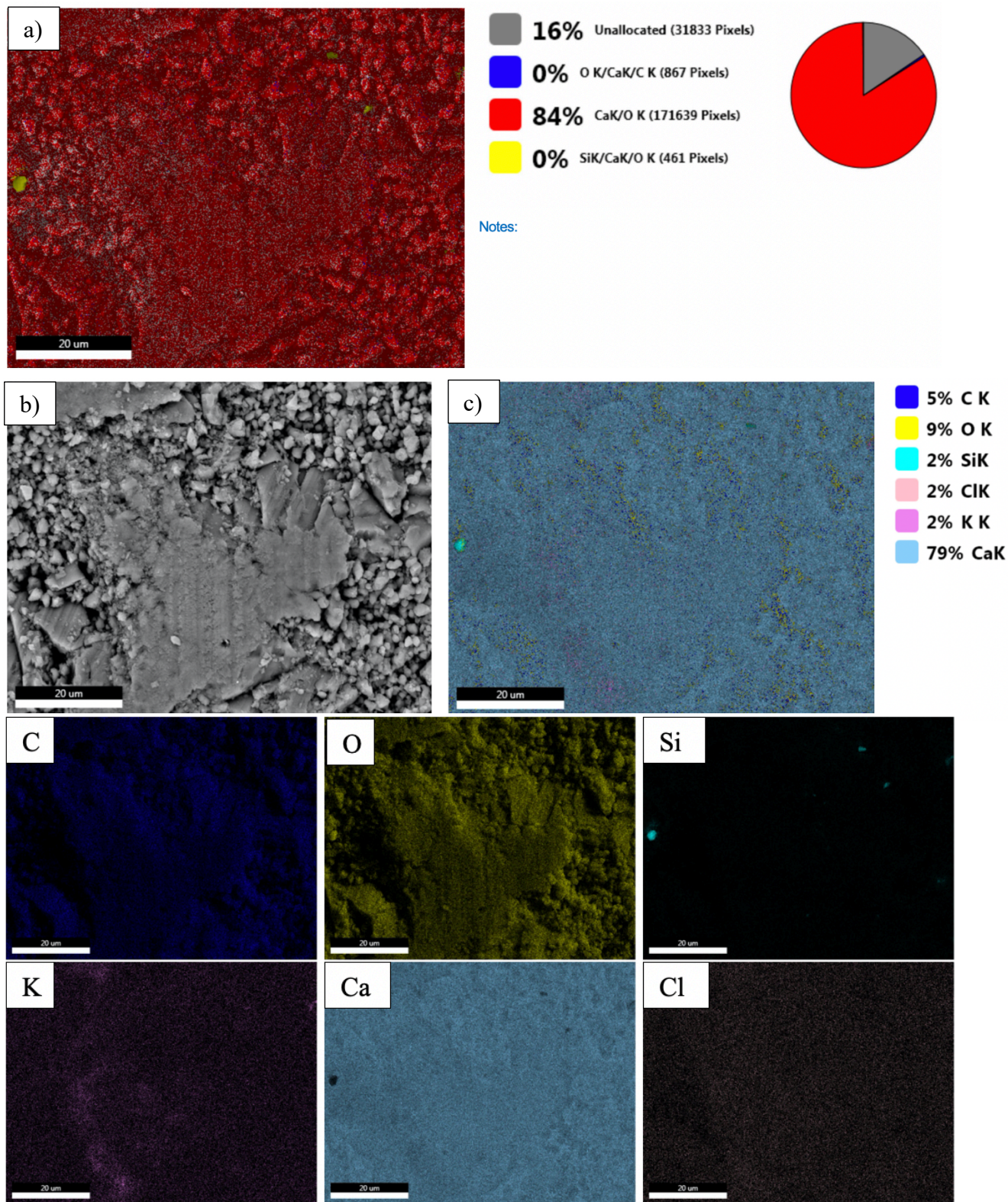
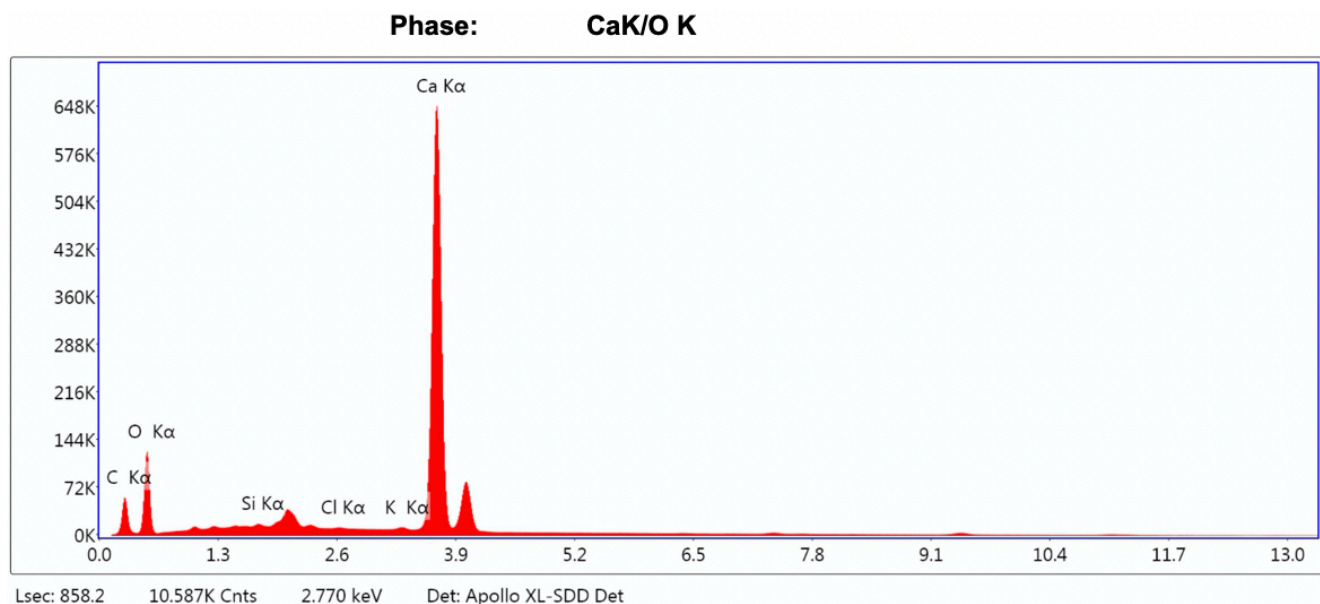


Figure 4. 11. Pure Limestone a) Live map at 2000x magnification obtained using FEI Quanta 3D FEG dual beam FIB/SEM at 20 kV b) Backscattered Electrons (BSE) micrograph at 2000x magnification c) EDS elemental map d) Distribution maps of fundamental elements



Element	Weight %	Atomic %	Net Int.
C K	5.3	11.5	344.1
O K	26.8	44.0	1025.5
SiK	0.1	0.1	21.9
ClK	0.1	0.1	25.6
K K	0.3	0.2	50.9
CaK	67.5	44.2	8800.6

Figure 4. 12. Ca and O dominant phase in limestone (a) SEM EDS elemental spectrum (b) quantification results

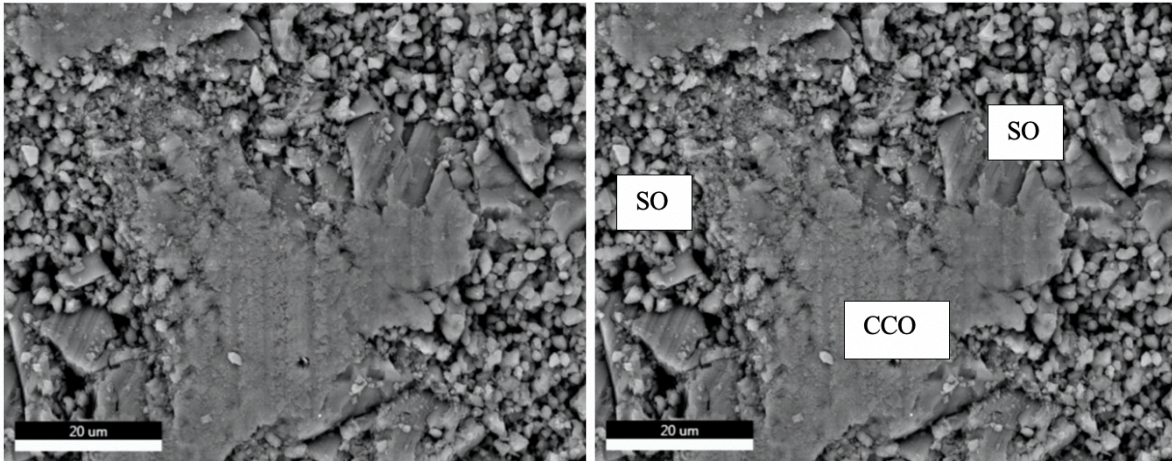


Figure 4. 13. SEM BSE image of pure limestone at 2000x magnification. SO is silicon oxide. CCO is calcium carbonate. There are traces of potassium oxide

4.2.4. SANDSTONE

For the Sandstone, the SEM live map shows tectosilicates as the majority minerals, predominantly quartz, with more than 50 % of all the phases present followed by the clay minerals (Figure 4.16a). The SEM BSE image, Figure 4.16b obtained at a 2000x magnification shows elongated detrital grain formed by quartz, covered with fine grains of calcite, the boundaries of which are very clearly visible. The intergranular clay particles, kaolinite, can also be seen in the SEM BSE image. The EDS elemental map and distribution maps of fundamental elements (Figure 4.16c and Figure 4.16d, respectively) indicate the presence of zirconia and pyrite as well as location of calcite particles spreading over the quartz minerals. Figure 4.17 and Figure 4.18 show EDS elemental spectrum and quantification results of two major phases in the sandstone. The silicon, aluminum and oxygen peaks confirm the identification of kaolinite particles in sandstone.

The four components that make the sandstone can be observed in SEM BSE image (Figure 4.19) the framework grains that are the larger particles, are quartz, along with K-feldspar and plagioclase, while the matrix (which is identified between framework grains) is kaolinite filling the interstitial pore space between quartz. The very small calcite crystals make up the cement

component. These small calcite crystals, sticking to quartz, bind the larger framework grains together.

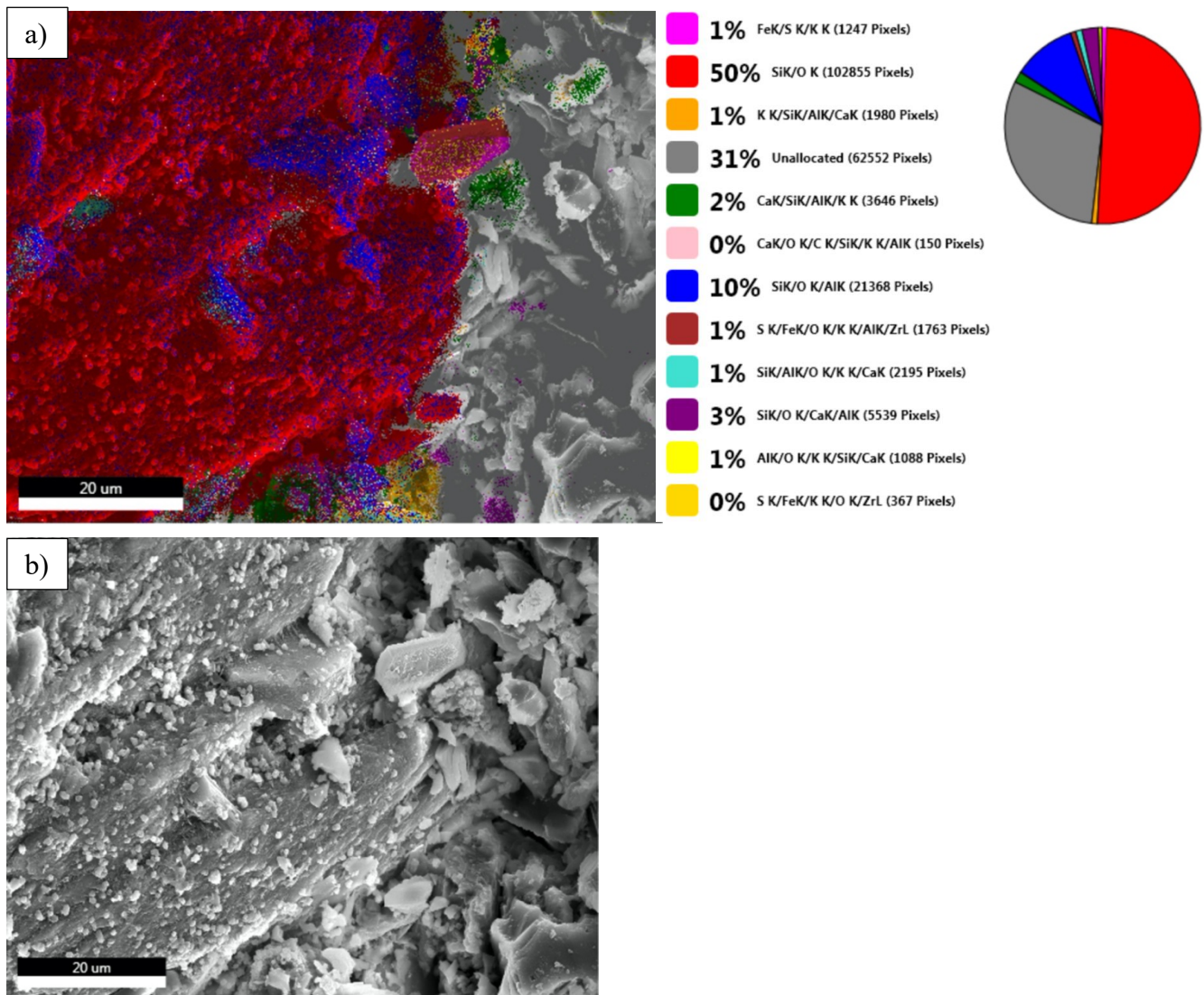


(figure cont'd)

(figure cont'd)

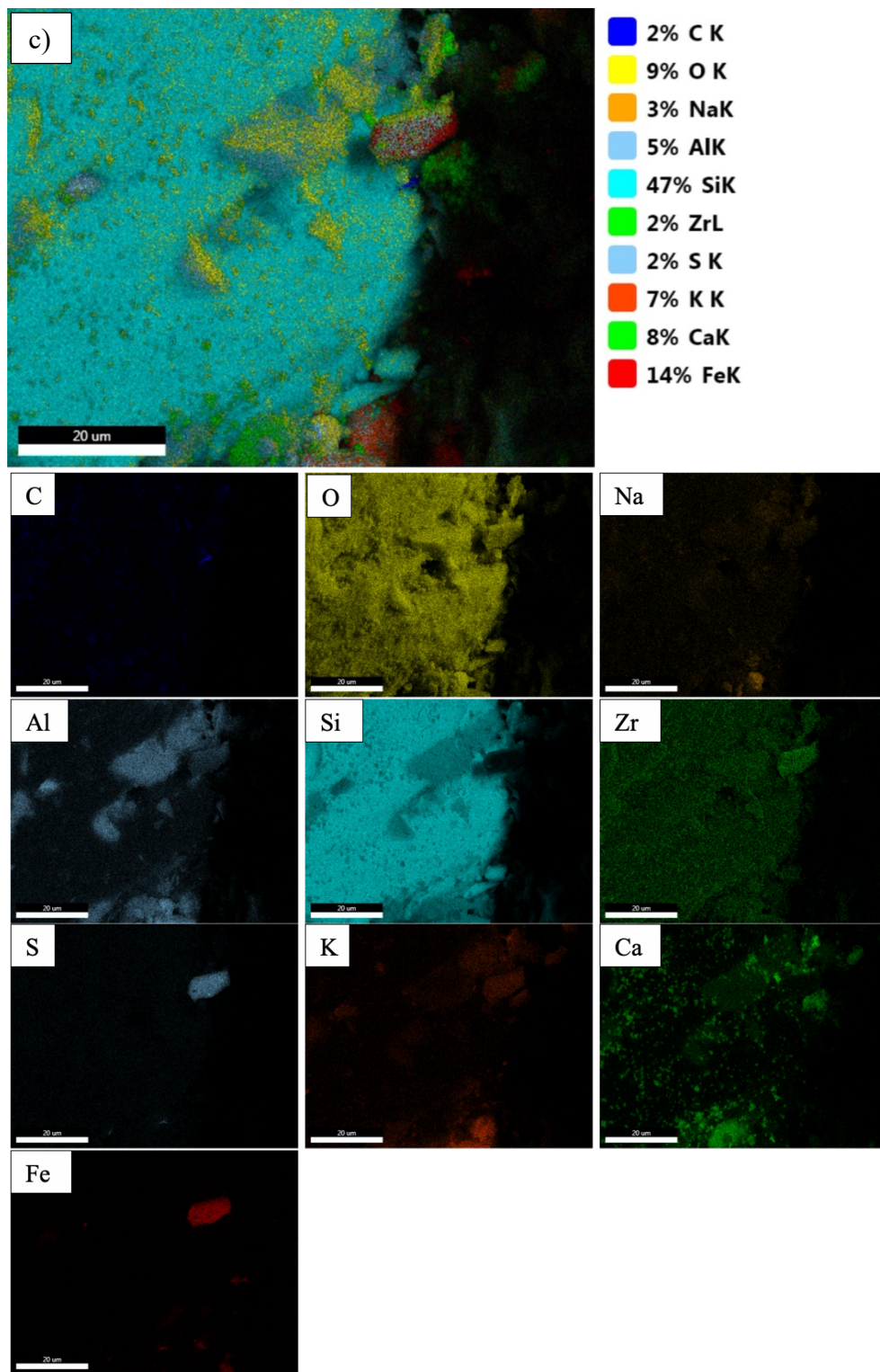
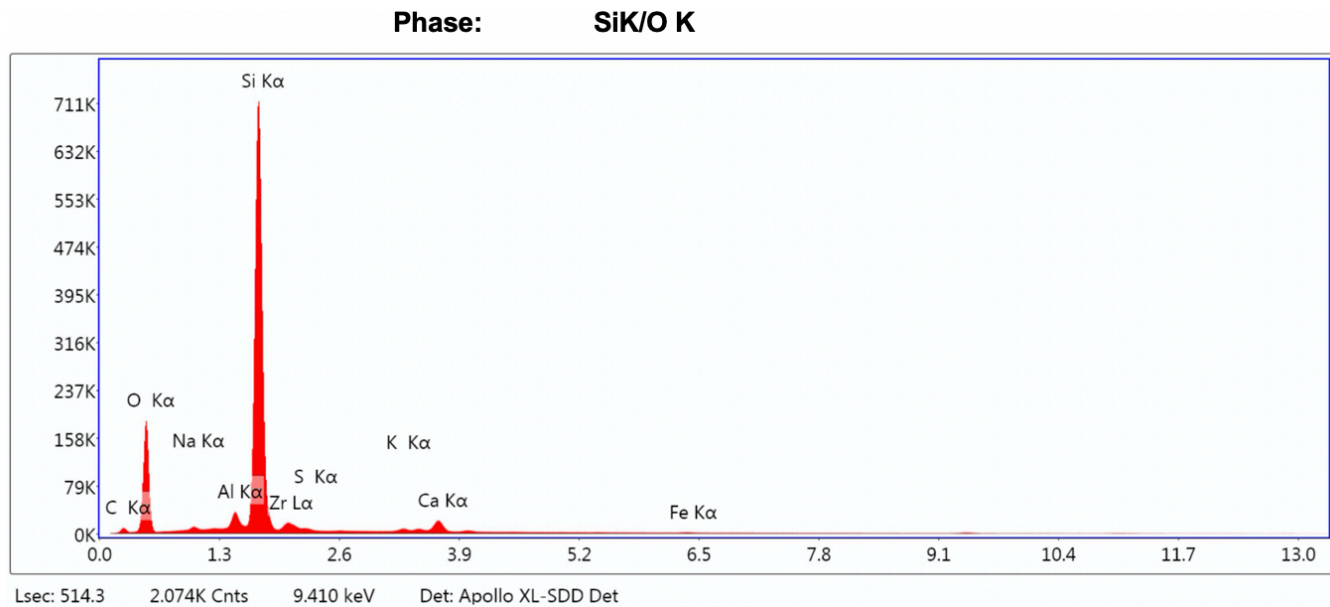


(figure cont'd)

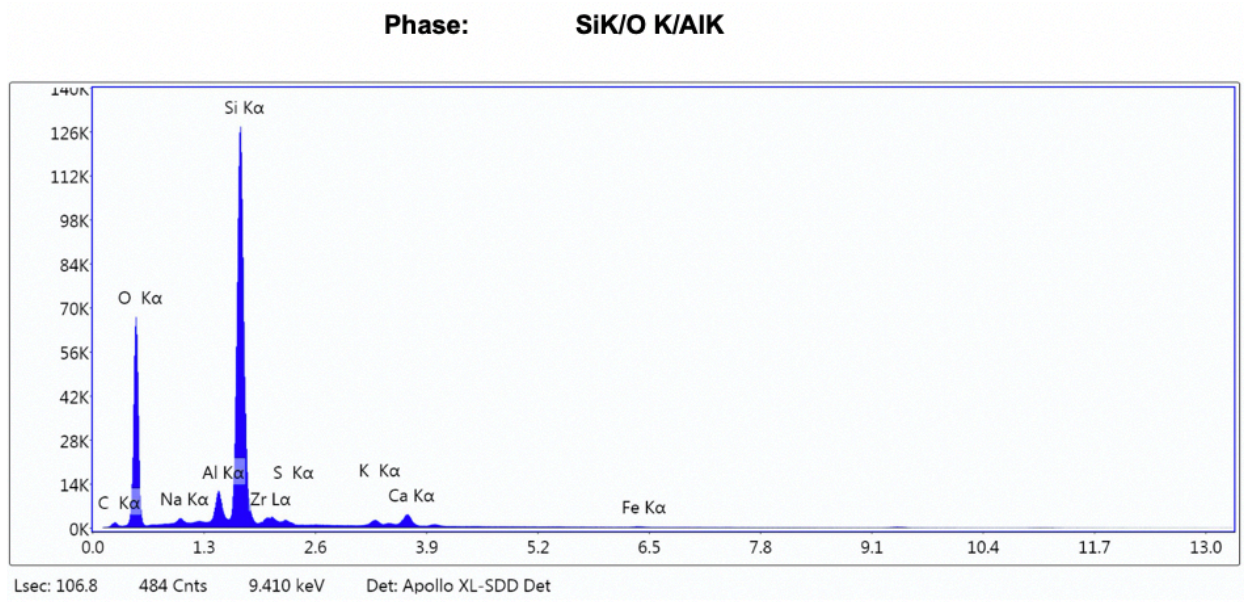
(figure cont'd)

Figure 4. 14. Pure Sandstone a) Live map at 2000x magnification obtained using FEI Quanta 3D FEG dual beam FIB/SEM at 20 kV b) Backscattered Electrons (BSE) micrograph at 2000x magnification c) EDS elemental map d) Distribution maps of fundamental elements



Element	Weight %	Atomic %	Net Int.
C K	4.39	8.07	91.20
O K	32.71	45.20	2548.60
NaK	0.15	0.14	21.10
AlK	2.00	1.64	478.90
SiK	52.40	41.25	12685.00
ZrL	3.03	0.73	240.80
S K	0.39	0.27	61.70
K K	1.11	0.62	154.80
CaK	3.51	1.93	427.10
FeK	0.33	0.13	21.20

Figure 4. 15. Si, and O dominant phase in sandstone a) SEM EDS elemental spectrum b) quantification results



Element	Weight %	Atomic %	Net Int.
C K	2.60	4.55	67.30
O K	43.68	57.43	4256.20
NaK	0.56	0.51	83.50
AlK	3.36	2.62	867.60
SiK	41.88	31.36	11014.90
ZrL	2.35	0.54	217.70
S K	0.74	0.49	135.70
K K	1.51	0.81	241.30
CaK	2.95	1.55	408.00
FeK	0.37	0.14	27.20

Figure 4. 16. Si, O and Al dominant phase in sandstone a) SEM EDS elemental spectrum b) quantification results

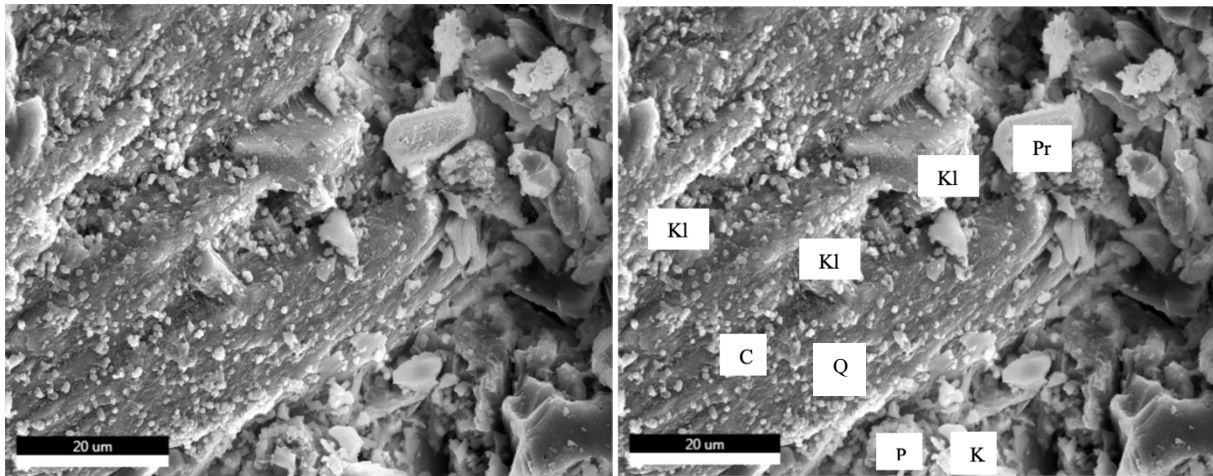


Figure 4. 17. SEM BSE image of pure sandstone at 2000x magnification. Pr is pyrite. K is K-feldspar. Q is Quartz. P is plagioclases. Kl is Kaolinite. C is Calcite. Traces of Zirconia also identified

4.2.4. CEMENT- LIMESTONE INTERFACE

The SEM live map of cement limestone (Figure 4.20a) shows the boundary between the bi-material, where the phase composed of calcium and oxygen (in blue) can be clearly separated from the rest of the phases present. The upper part of the Figure 4.20a shows the different phases that form the cement while single phase limestone can be seen spread over the majority of the live map. The porous calcium carbonate grains can be identified in the SEM BSE image obtained at a magnification of 2000x (Figure 4.20b) as well as the densely packed cement minerals.

The distribution of the elements like silicon, aluminum, potassium, sulphur and iron in only the top section of the SEM EDS elemental map and the distribution maps of fundamental elements (Figure 4.20c and Figure 4.20d, respectively) and calcium and carbon in the remaining part of the map further solidify the location of cement and limestone in the micrographs. The SEM EDS spectrum and quantification of a major phase in cement (Figure 4.21) is comprised of calcium, silicon, oxygen, sulphur, and aluminum. The identification of these elements indicate the presence of C-S-H, portlandite, ettringite and monosulphoaluminate minerals.

In Figure 4.21, the ration of sulphur to aluminum, greater than one, suggest the existence of ettringite since sulphur to aluminum ration less than one is suggestive of mononsulphoaluminate (Diamond, 2004). The observance of calcium carbonate in limestone region (bottom half of the SEM BSE image, Figure 4.23) is corroborated by the calcium and oxygen peaks in Figure 4.22a and elements atomic percentage in the quantification results (Figure 4.22b).

The cement-limestone interface boundary and the cement and limestone region are marked in Figure 4.23. The bright spots observed in the cement region of BSE image are identified as residual cement or unhydrated cement particles. The calcium silicate clinker comprises of an amalgam of different crystalline phases which includes dicalcium silicate (belite), tricalcium silicate (alite), tricalcium aluminate and tetracalcium alumino ferrite. The anhydrous particles of all these phases are retained in cement pastes because the grains that hydrate completely are the finer cement particles (Scrivener, 2004). C-S-H developed in phenograin morphology (Diamond, 2004) can be observed in the Figure 4.23. The C-S-H phenograin morphology appear as grains that are 10um or greater in size and are identified as soft rather than hard particles (Diamond and Bonen, 1993) and are relatively less porous as seen in the BSE image.

The irregular deposits of portlandite are of different sizes and can be up to several micros and precipitate as euhedral crystals These portlandite crystals evolve to agglomerates depending on several factors like hydration age, type of additives present and space present for crystallization. The cement paste with the passage of time transforms from thin inter-dispersed crystals to formless characteristics of mature paste (Franus et., al). The distinction between C-S-H and portlandite at times become difficult in BSE images (Diamond, 2004). Ettringite, having hexagonal needles morphology can also recrystallize and appear as large masses (Scrivener, 2004). One of the reasons it is difficult to locate ettringite in BSE image is because it intermixes with C-S-H and

portlandite (Evangelista and Guedes, 2019). Cracks expanding in the cement section seen in Figure 4.23 can be the associated with the ettringite's characteristic straight and curved shrinkage induced crack patterns (Diamond, 2004).

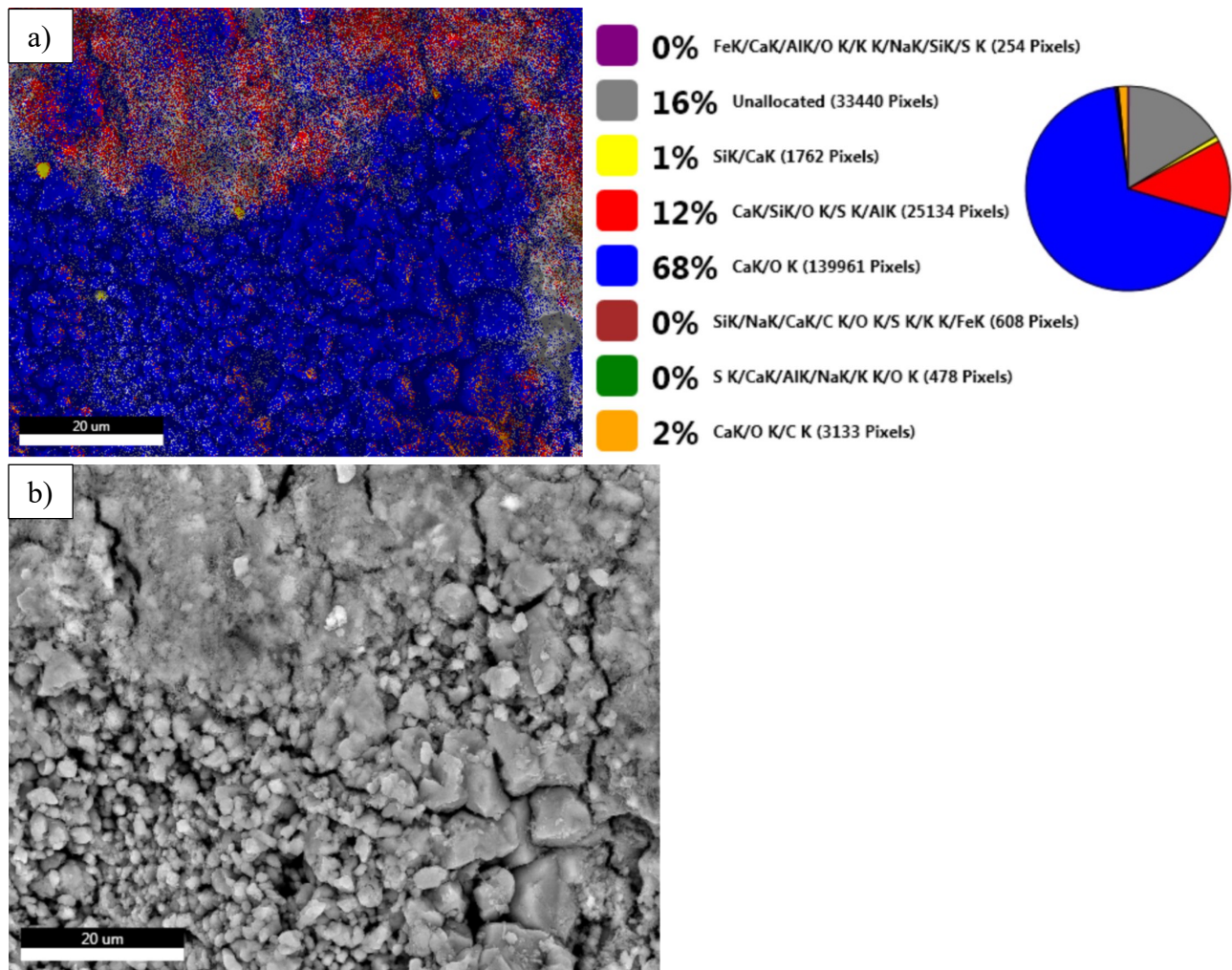


(figure cont'd)

(figure cont'd)

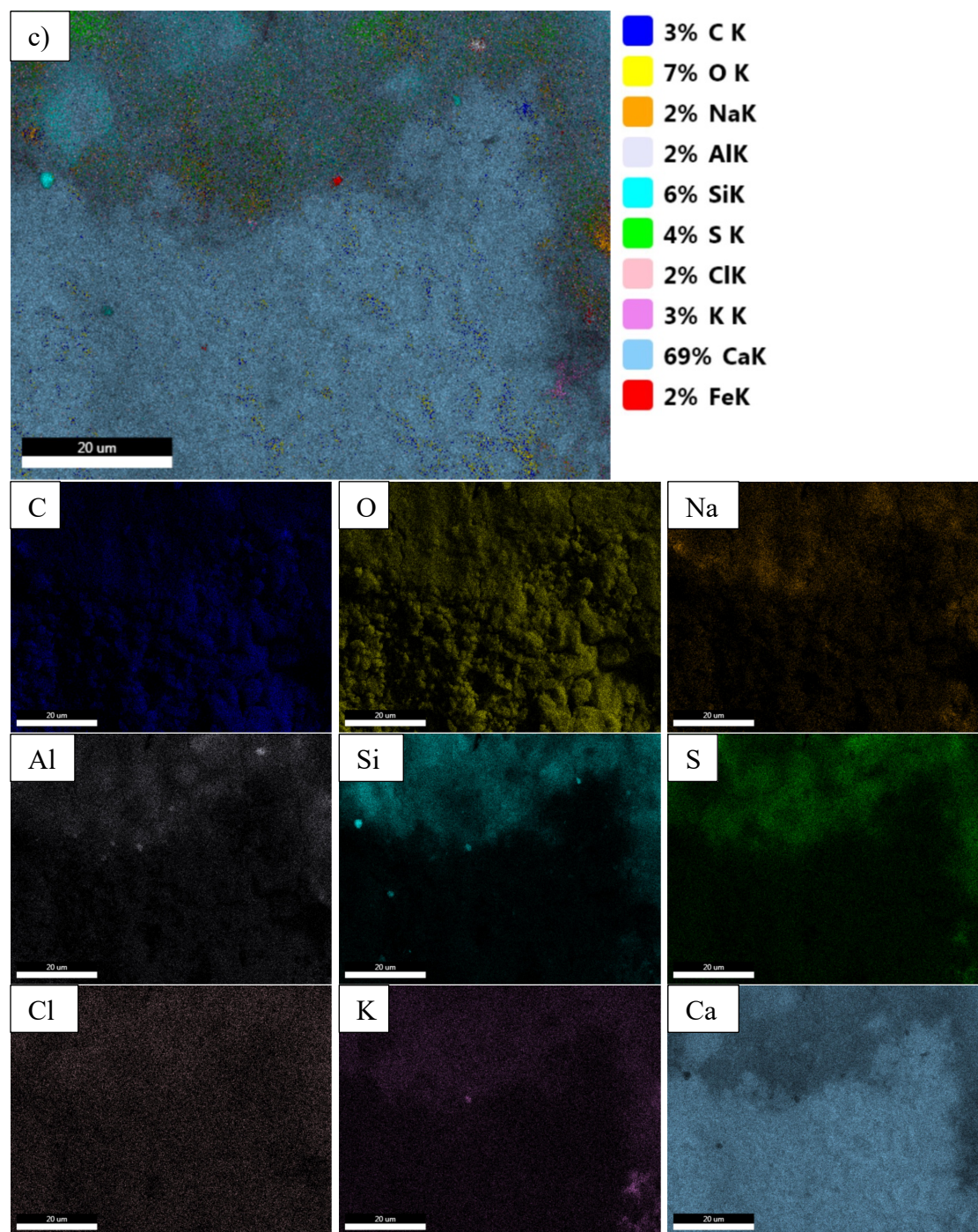


(figure cont'd)

(figure cont'd)

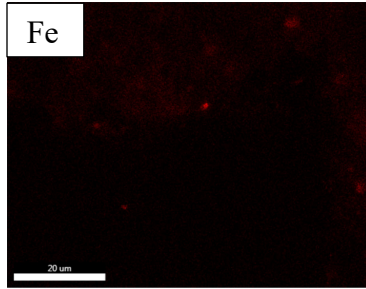
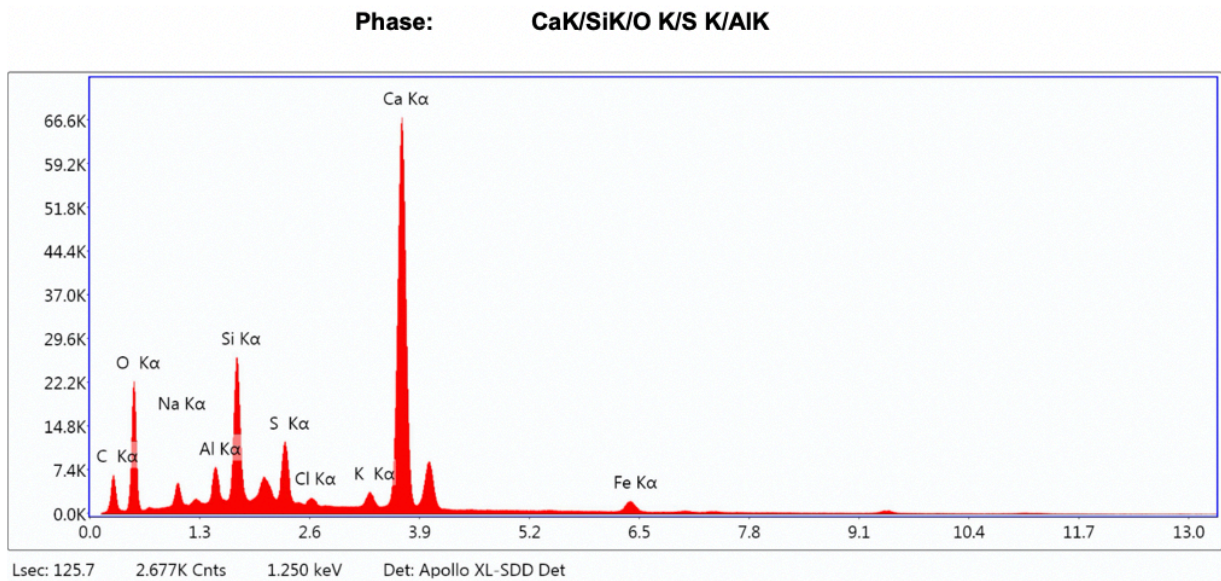


Figure 4. 18. Cement-Limestone a) Live map at 2000x magnification obtained using FEI Quanta 3D FEG dual beam FIB/SEM at 20 kV b) Backscattered Electrons BSE micrograph at 2000x magnification c) EDS elemental map d) Distribution maps of fundamental elements



(figure cont'd)

(figure cont'd)

Element	Weight %	Atomic %	Net Int.
C K	6.3	13.2	259.7
O K	25.8	40.6	1192.6
NaK	1.5	1.6	173.2
AlK	1.8	1.7	377.7
SiK	7.6	6.8	1774.4
S K	5.0	3.9	1014.4
ClK	0.6	0.4	114.6
K K	1.3	0.9	230.5
CaK	46.9	29.4	6187.2
FeK	3.2	1.5	205.5

Figure 4. 19. Ca, Si, O, S and Al dominant phase in cement-limestone interface a) SEM EDS elemental spectrum b) quantification results

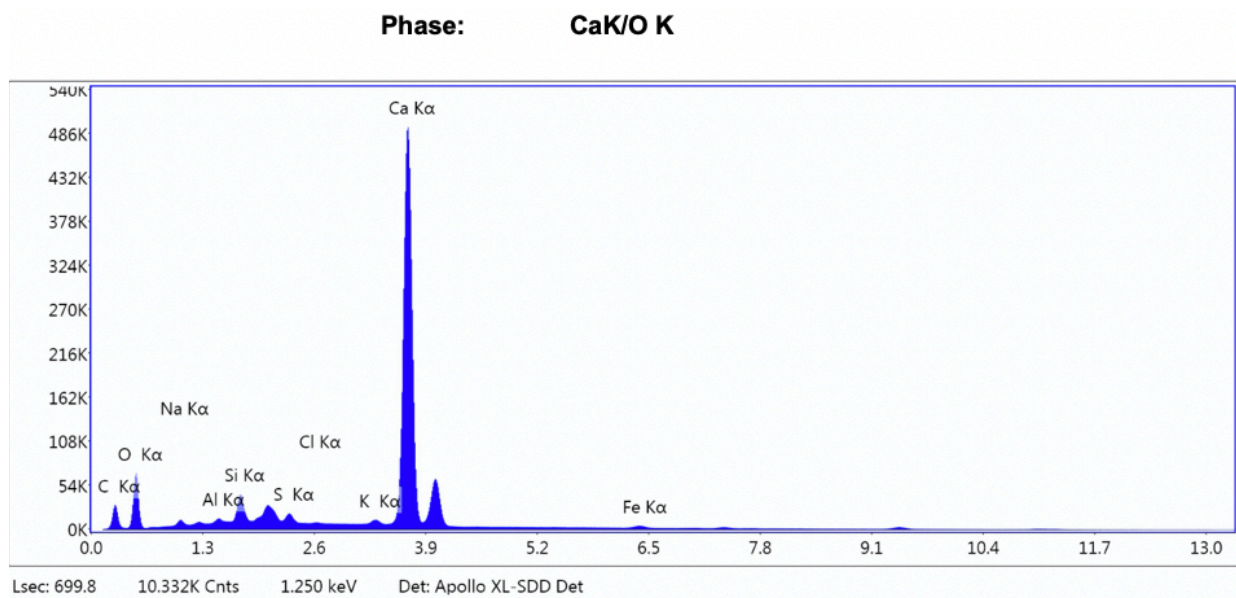


(figure cont'd)

(figure cont'd)

Element	Weight %	Atomic %	Net Int.
C K	4.3	10.2	225.8
O K	20.4	36.1	687.0
NaK	0.1	0.1	6.9
AlK	0.1	0.1	8.7
SiK	1.9	1.9	393.2
S K	1.6	1.4	297.5
ClK	0.1	0.1	18.7
K K	0.6	0.4	99.5
CaK	69.8	49.2	8223.3
FeK	1.1	0.6	63.2

Figure 4. 20. Ca and O dominant phase in cement-limestone interface a) SEM EDS elemental spectrum b) quantification results

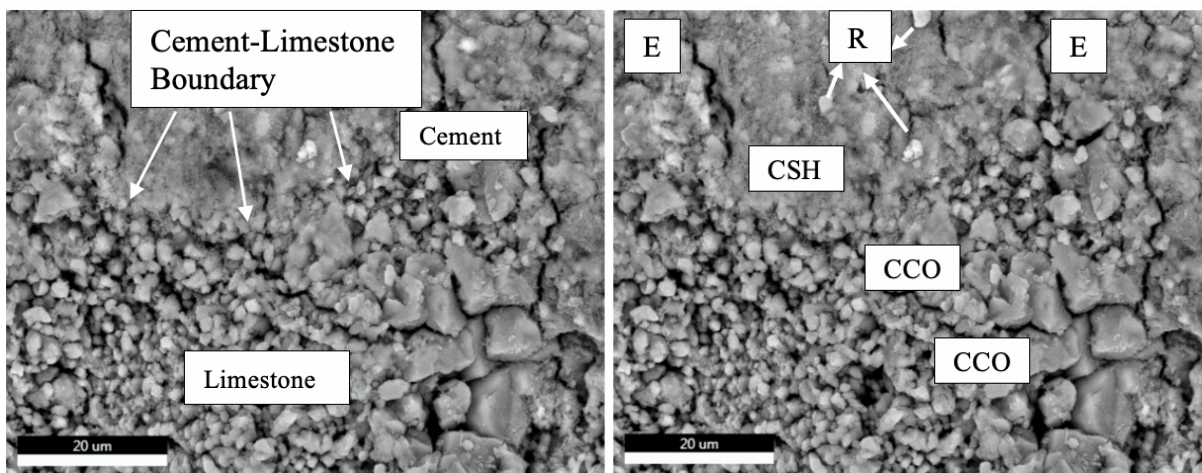
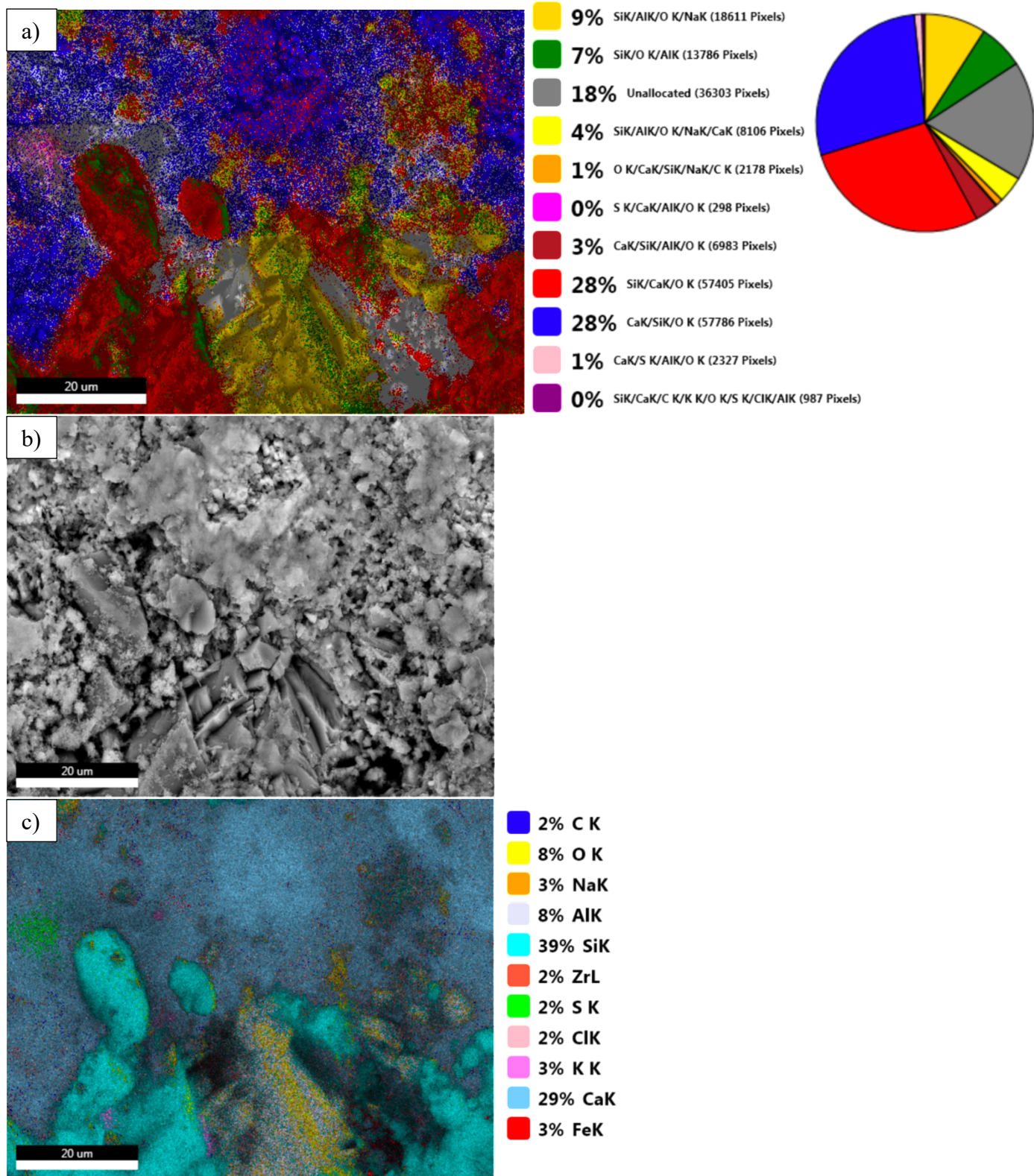


Figure 4. 21. BSE SEM image of cement-limestone interface at 2000x magnification. E is Ettringite. CCO is Calcium Carbonate. R is Residual cement

4.2.5. CEMENT-SANDSTONE INTERFACE

The SEM live map of cement-sandstone interface (4.24a) shows distinctively the silicon dominant phases in the bottom half of the map while calcium rich phase spread over the top half. The SEM BSE micrograph (Figure 4.24b), alone, gives an idea of the quartz and plagioclase crystals in sandstone located in the lower half the image. The SEM EDS elemental map and maps of fundamental elements (Figure 4.24c and Figure 4.24d respectively) confirm the distribution of tectosilicates in sandstone and the location of cement hydrated phases. The SEM EDS spectrum and quantitative results of the four dominant phases present can be seen in Figure 4.25, 4.26, 4.27 and 4.28. The tall peaks of silicon, oxygen, calcium and sodium and weight percent of these element in Figure 4.25a and Figure 4.25b confirm the presence of predominant tectosilicates. The EDS elemental spectrum and quantitative results (Figure 4.26) of silicon, oxygen and aluminum dominant phase is indicative of clay particles i.e., kaolinite. The SEM EDS spectrum and quantitative results (Figure 4.25) is validation of quartz whereas Figure 4.28 provides the elemental composition of the hydrated cement. Figure 4.29 shows the SEM BSE images of cement-sandstone interface at different resolutions. The cement-sandstone interface boundary appears clearly in SEM BSE image at 500x magnification (4.29a). The image also reveals the existence of several pores along the interface and cracks that extend to cement section. These shrinkage cracks observed along the interface grow in the cement due to the variation in the moisture as the cement shrinks upon drying while cement expansion occurs upon water absorption.



(figure cont'd)

(figure cont'd)

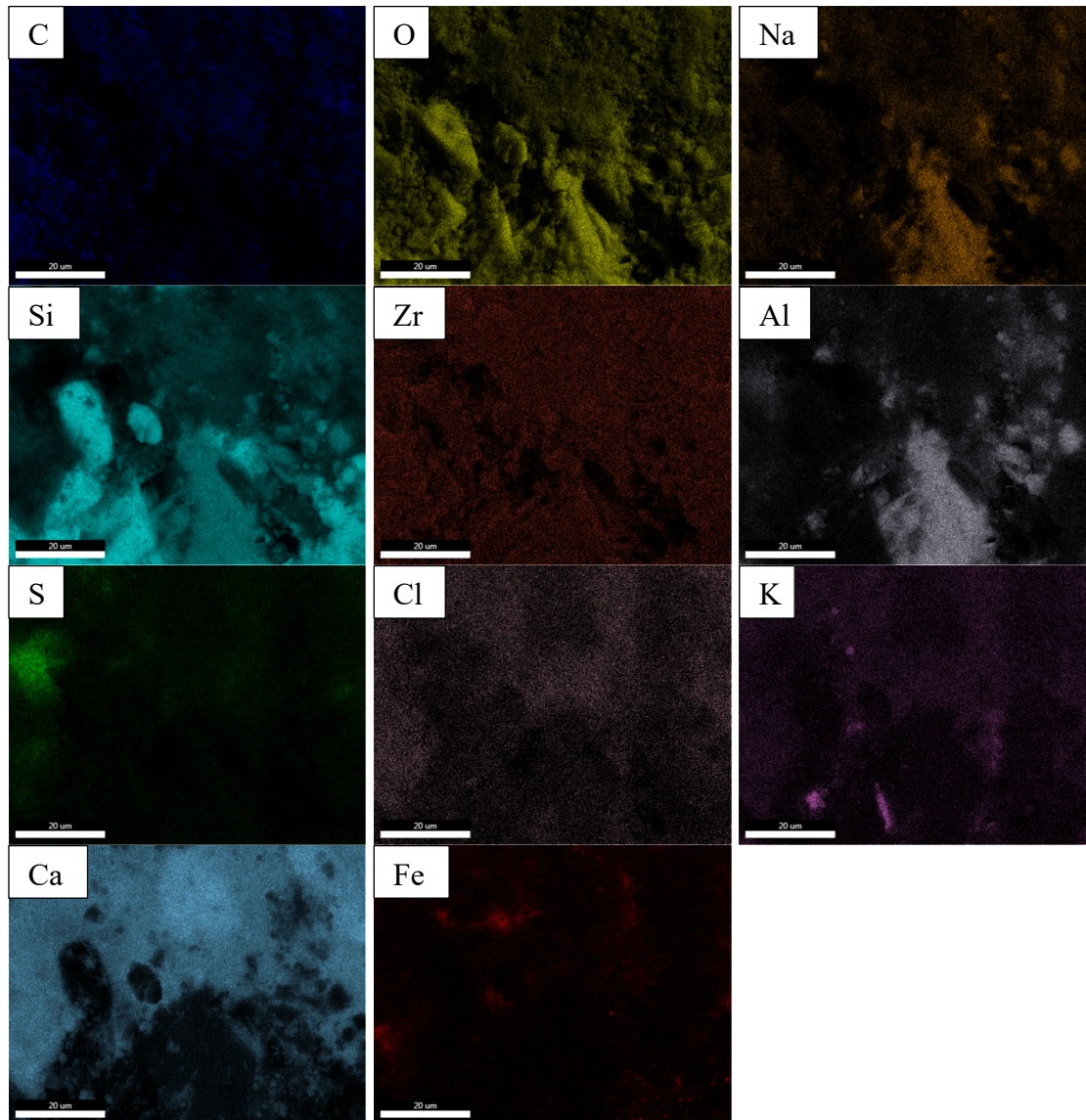
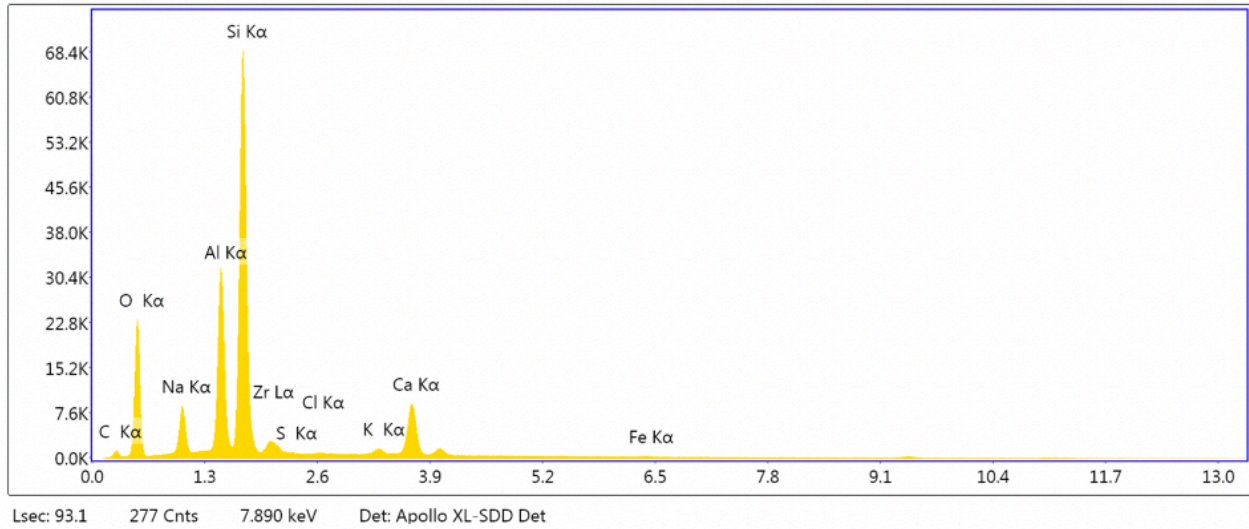


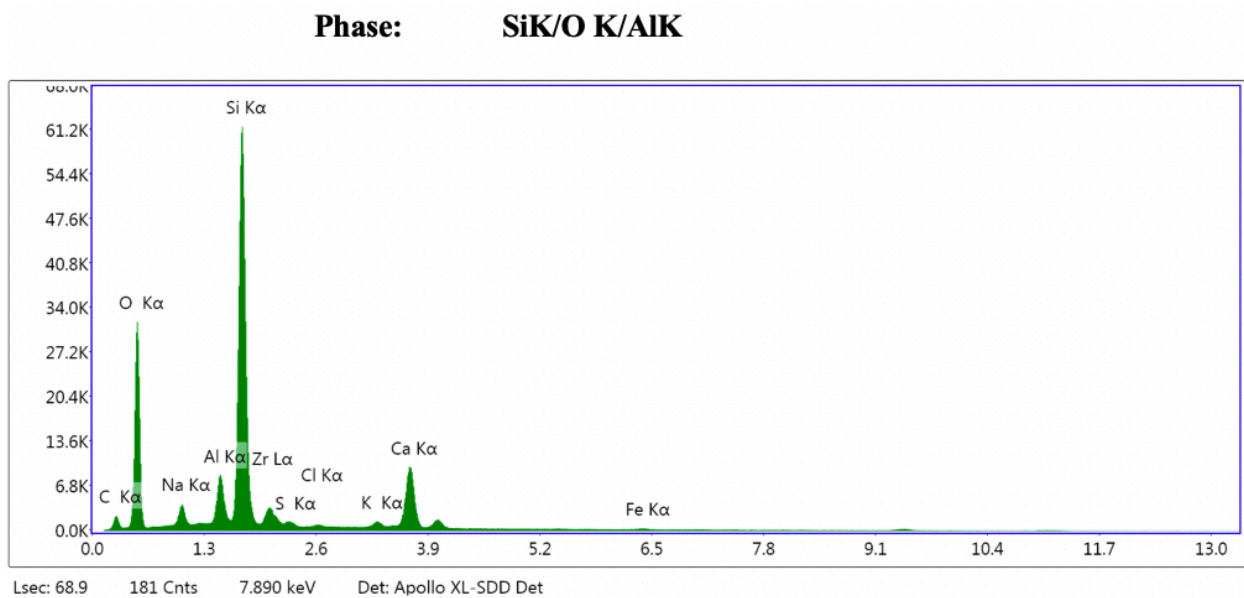
Figure 4. 22. Cement-Sandstone a) Live map at 2000x magnification obtained using FEI Quanta 3D FEG dual beam FIB/SEM at 20 kV b) Backscattered Electrons (BSE) micrograph at 2000x magnification c) EDS elemental map d) Distribution maps of fundamental elements

Phase: SiK/AlK/O K/NaK



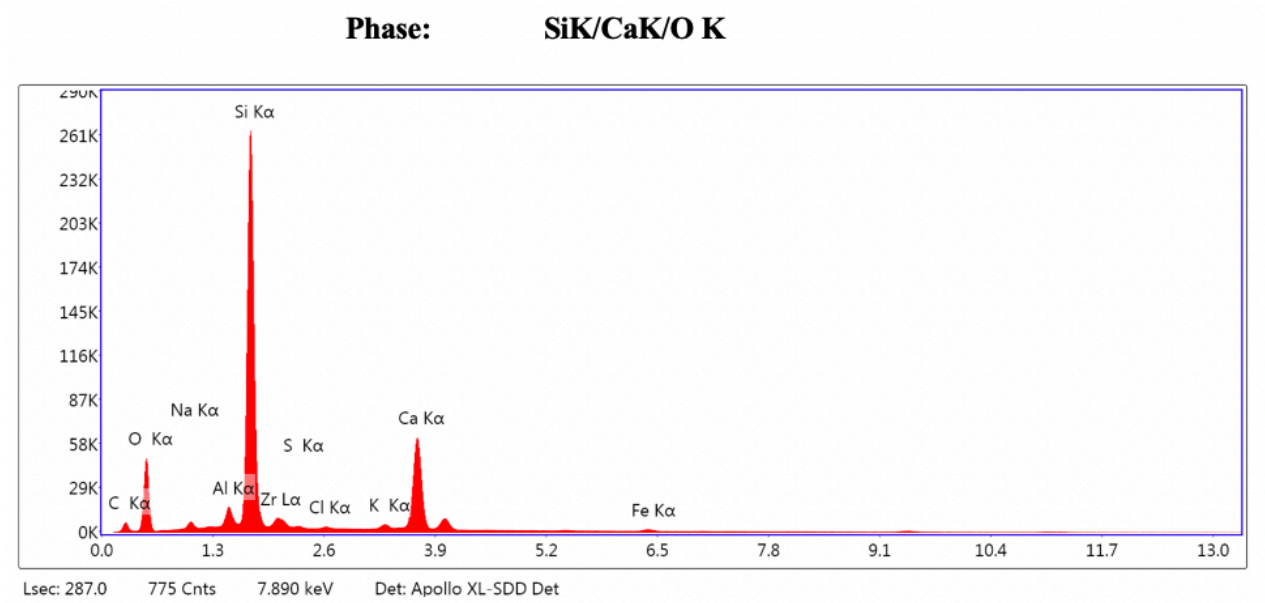
Element	Weight %	Atomic %	Net Int.
C K	3.5	6.8	69.8
O K	27.9	40.2	1730.8
NaK	4.6	4.6	564.2
AlK	14.3	12.2	2838.6
SiK	35.1	28.8	6599.3
ZrL	2.8	0.7	198.5
S K	0.0	0.0	4.7
ClK	0.1	0.1	12.5
K K	1.1	0.7	137.3
CaK	10.2	5.9	1096.4
FeK	0.4	0.2	24.9

Figure 4. 23. Si, Al, O and Na dominant phase in cement-sandstone interface a) SEM EDS elemental spectrum b) quantification results



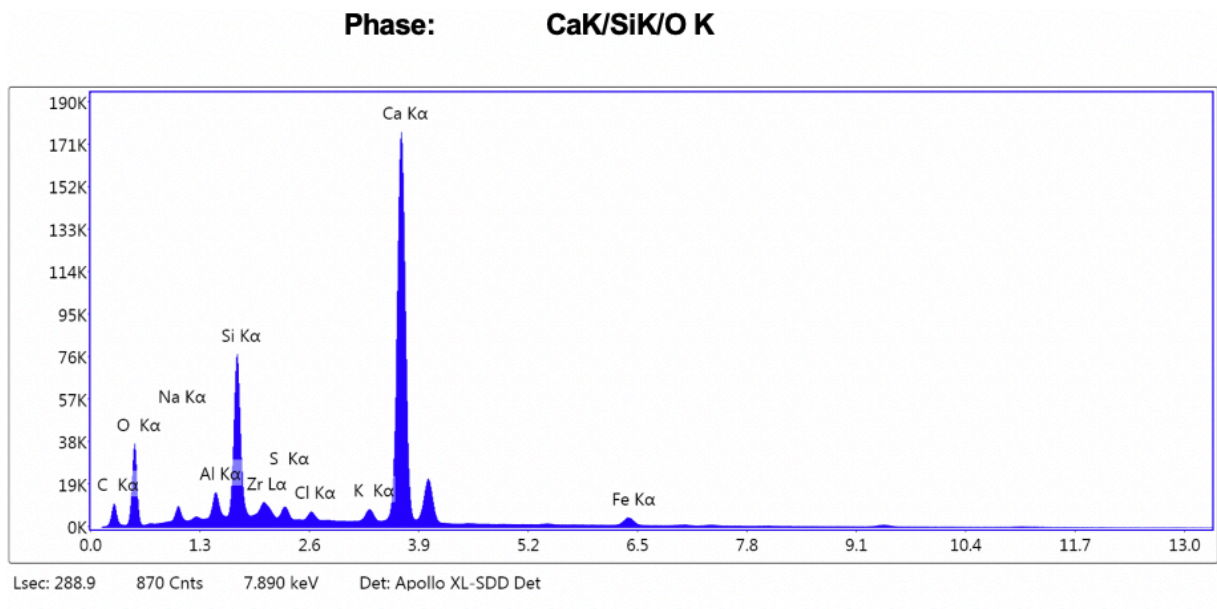
Element	Weight %	Atomic %	Net Int.
C K	4.5	8.1	129.7
O K	39.2	53.2	3121.7
NaK	2.2	2.1	310.0
AlK	4.0	3.2	996.2
SiK	32.0	24.7	8149.1
ZrL	4.0	0.9	380.4
S K	0.5	0.4	101.9
ClK	0.3	0.2	47.5
K K	1.1	0.6	171.9
CaK	11.9	6.4	1636.3
FeK	0.4	0.2	31.2

Figure 4. 24. Si, Al and O dominant phase in cement-sandstone interface a) SEM EDS elemental spectrum b) quantification results



Element	Weight %	Atomic %	Net Int.
C K	5.4	11.0	118.8
O K	23.9	36.3	1179.7
NaK	0.3	0.3	37.3
AlK	1.8	1.6	354.3
SiK	39.9	34.5	8280.9
ZrL	2.9	0.8	214.9
S K	0.3	0.2	42.8
ClK	0.3	0.2	39.6
K K	1.1	0.7	147.1
CaK	23.1	14.0	2493.7
FeK	1.1	0.5	57.9

Figure 4. 25. Si and O dominant phase in cement-sandstone interface a) SEM EDS elemental spectrum b) quantification results



Element	Weight %	Atomic %	Net Int.
C K	4.2	9.7	179.5
O K	21.1	36.3	883.2
NaK	0.8	1.0	91.2
AlK	1.4	1.4	282.3
SiK	10.1	9.9	2305.2
ZrL	2.3	0.7	229.9
S K	0.9	0.8	183.1
ClK	0.7	0.5	123.4
K K	1.2	0.9	206.5
CaK	54.6	37.6	7043.4
FeK	2.8	1.4	173.0

Figure 4. 26. Ca, Si and O dominant phase in cement-sandstone interface a) SEM EDS elemental spectrum b) quantification results

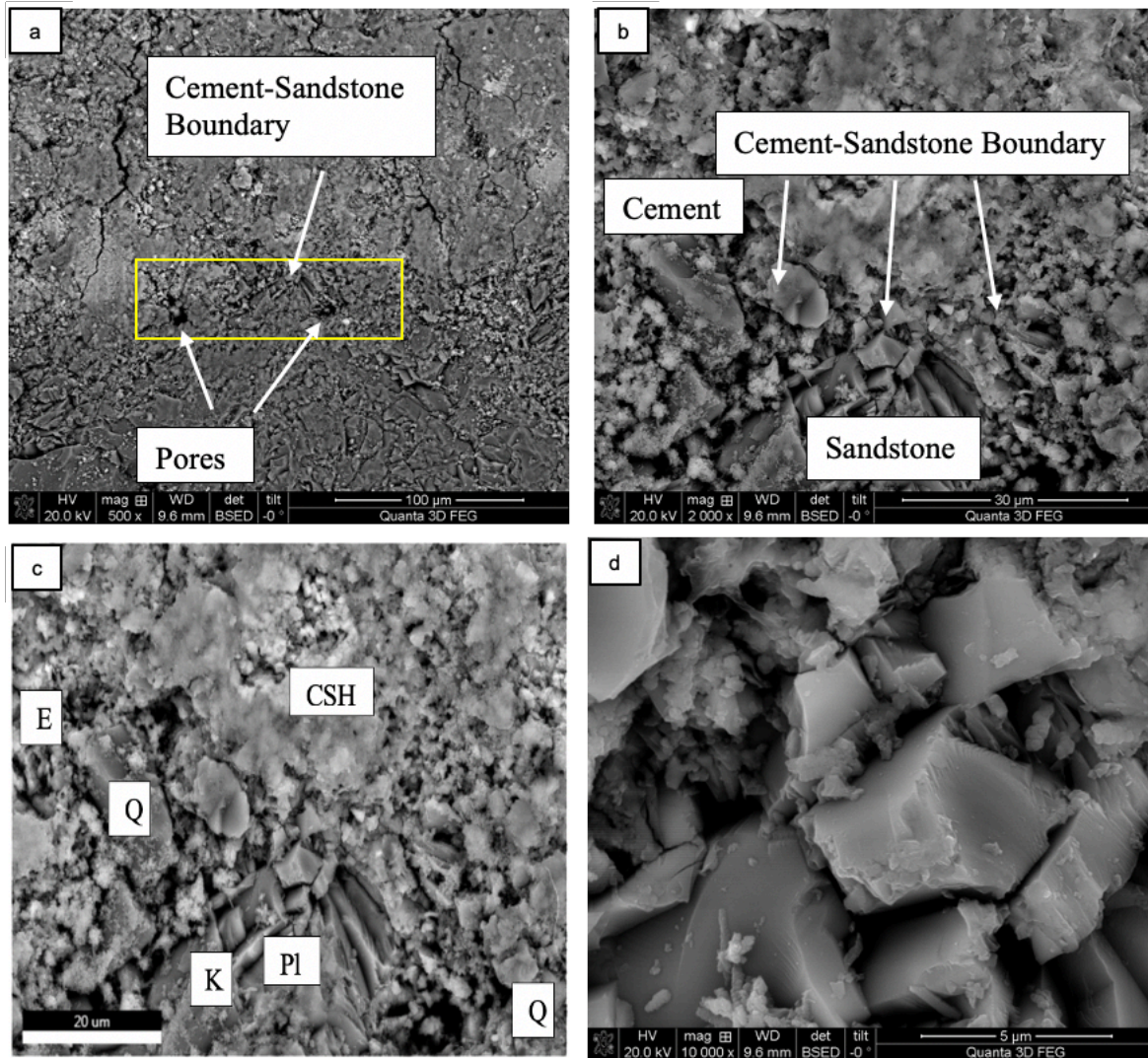


Figure 4. 27. SEM BSE micrograph at a) 500x b) 2000x c) 2000x d) 10000x magnification. E is Ettringite. Q is Quartz. CSH. K is K-feldspar. Pl is Plagioclases

4.2.6. CEMENT-SHALE INTERFACE

For the analysis of cement-shale interface, the SEM live map (Figure 4.30a), shows the different phases involved in the composition of the cement and rock but does not distinctively define the interface between the two. When compared to the SEM BSE images of cement-sandstone and cement-limestone the cement-shale SEM BSE micrograph obtained at 2000x magnification (Figure 4.30b) is not very helpful in distinguishing the two composites under study, although the large tectosilicate minerals in the shale can be observed on the bottom of the SEM image. However,

the SEM EDS elemental map and the distribution maps of fundamental elements play a significant part in determining the placement of shale and cement as well as the minerals present.

The SEM EDS elemental map of cement (Figure 4.4c) showed calcium as the dominant element, 59 percent, followed by silicon with 15 percent, while the SEM EDS elemental map of shale (Figure 4.9c) revealed higher percentage of silicon with calcium in second place, 40 and 15 percent respectively. It is evident from these maps that cement has higher calcium content while shale has greater amount of silicon. From the cement-shale elemental map its evident that the bottom center section of the map is rich in silicon, suggestive of quartz, plagioclase and or K-feldspar, while calcium is spread over the remaining part. The SEM analysis of cement i.e., live map (Figure 4.4a), EDS elemental distribution (Figure 4.4c) and distribution maps of fundamental elements (Figure 4.4d) showed no presence of magnesium while it appeared as one of the primary elements in the SEM analysis of shale (Figure 4.9a, Figure 4.9c and Figure 4.9d). Therefore, the appearance of magnesium in Figure 4.30c and Figure 4.30d is indicative of mineral dolomite in shale rock.

The SEM BSE image obtained at 250x magnification (Figure 4.34a) reveals the cement-shale boundary, and the microstructural characteristics of shale and cement can be seen in Figure 4.34b. The organized features observed in cement can be attributed to the fact that it is an engineered product as compared to the irregular features in shale rock. Porosities observed in both cement and shale had approximately same sizes and might have been augmented due to the drying process for SEM imaging, causing shrinkage of swelling clay particles.

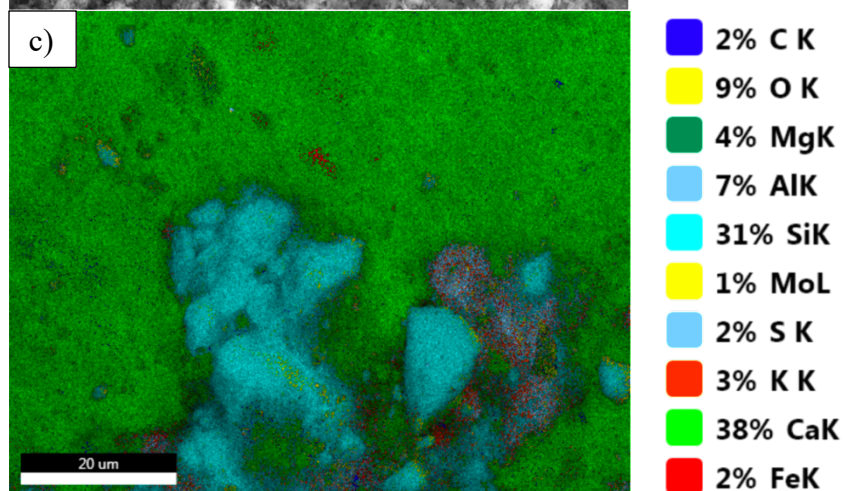
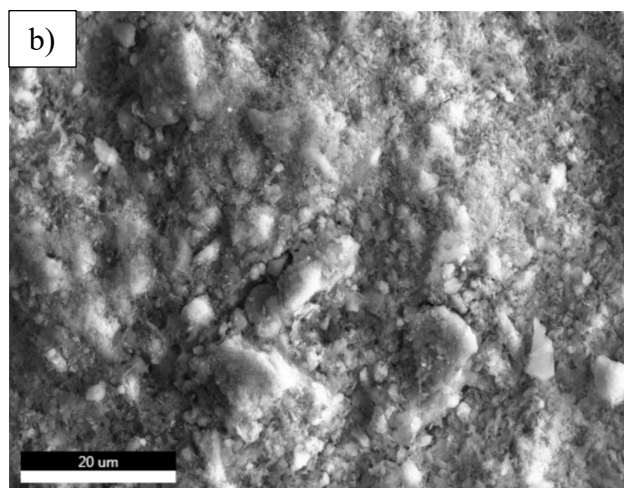
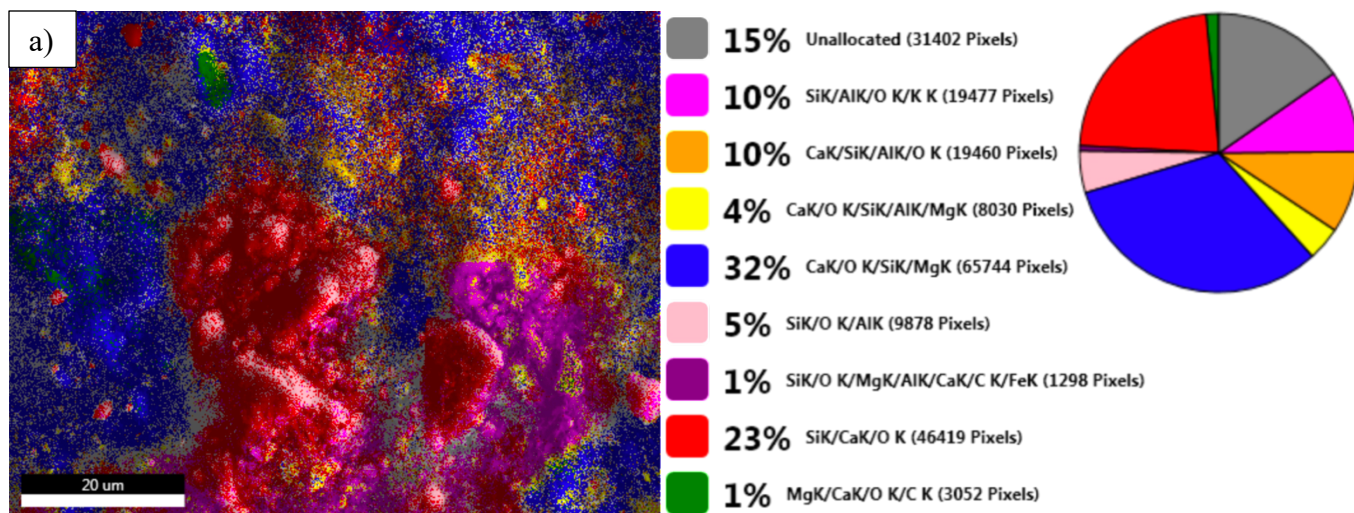


(figure cont'd)

(figure cont'd)

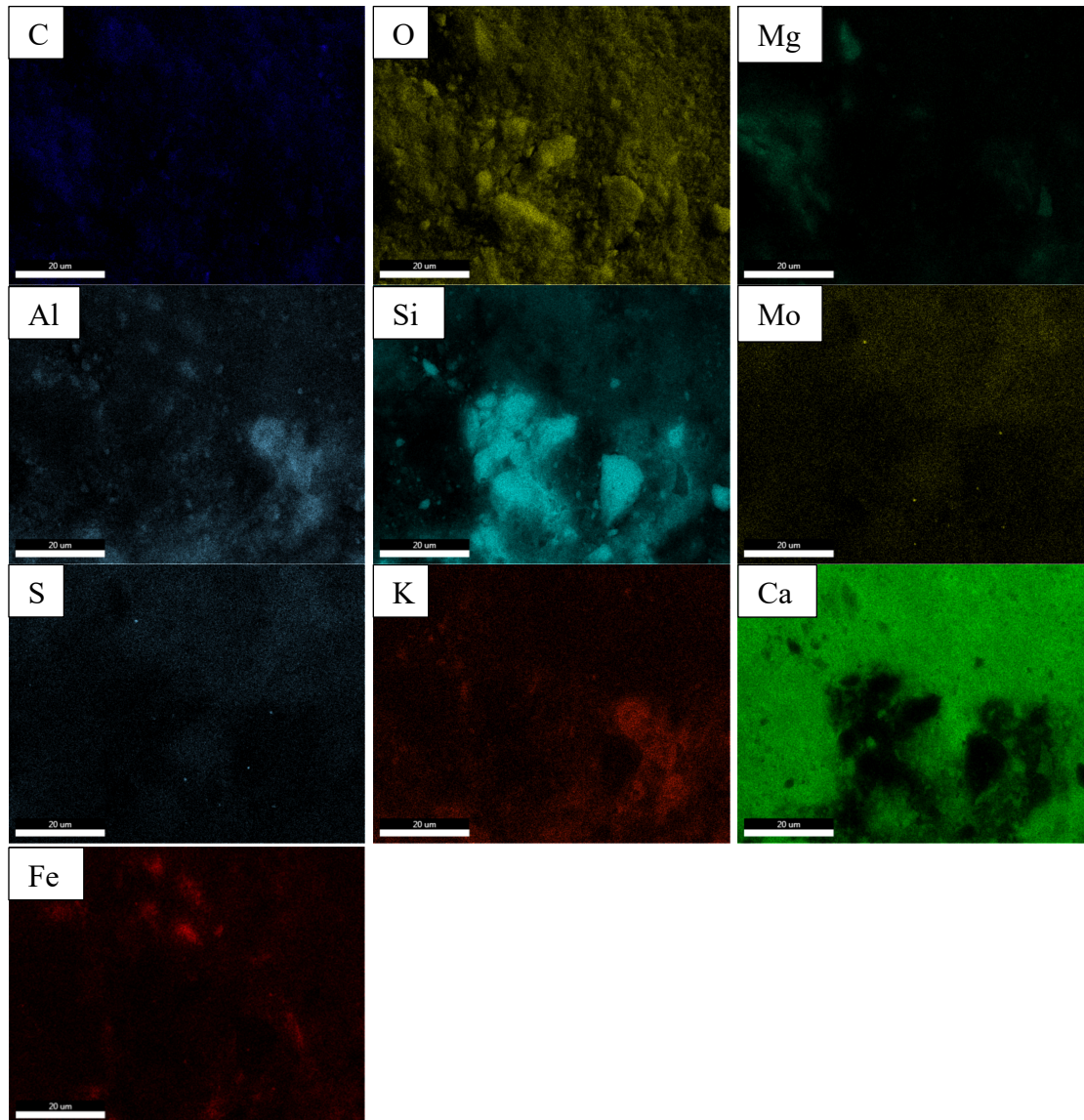
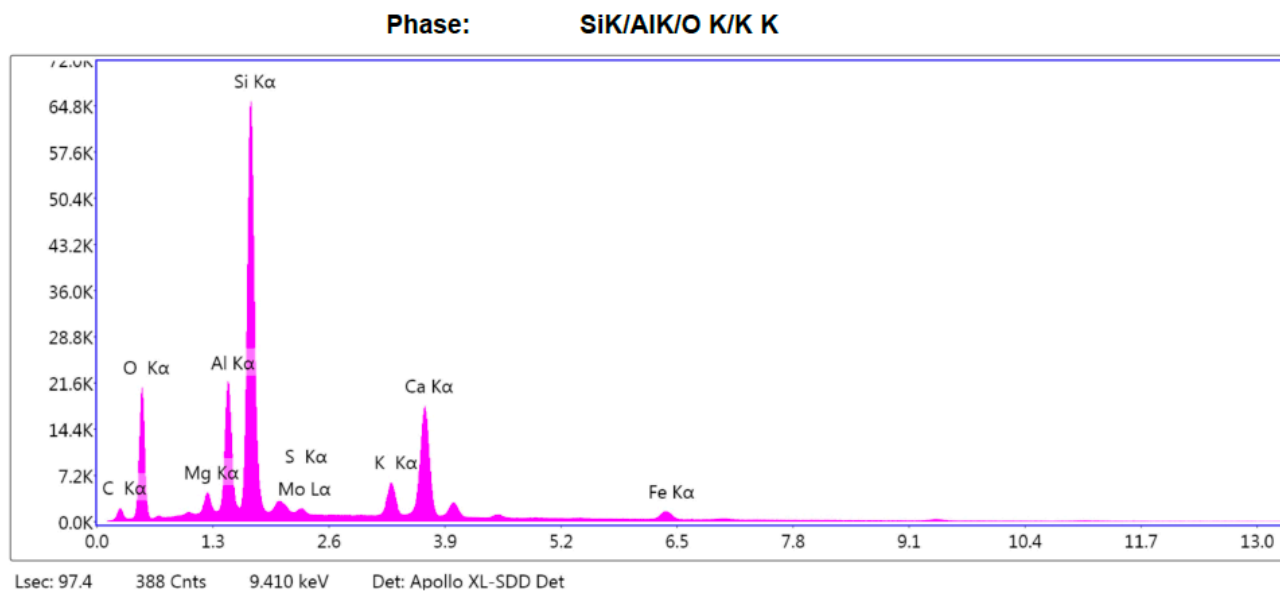
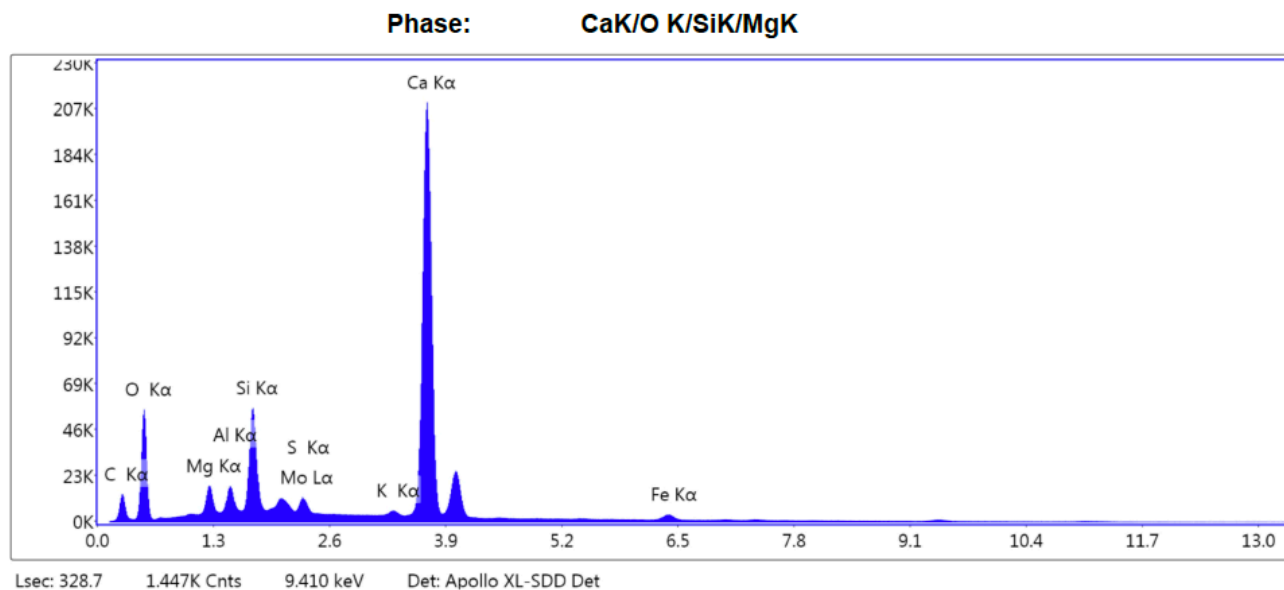


Figure 4. 28. Cement-Shale a) Live map at 2000x magnification obtained using FEI Quanta 3D FEG dual beam FIB/SEM at 20 kV b) Backscattered Electrons (BSE) micrograph at 2000x magnification c) EDS elemental map d) Distribution maps of fundamental elements



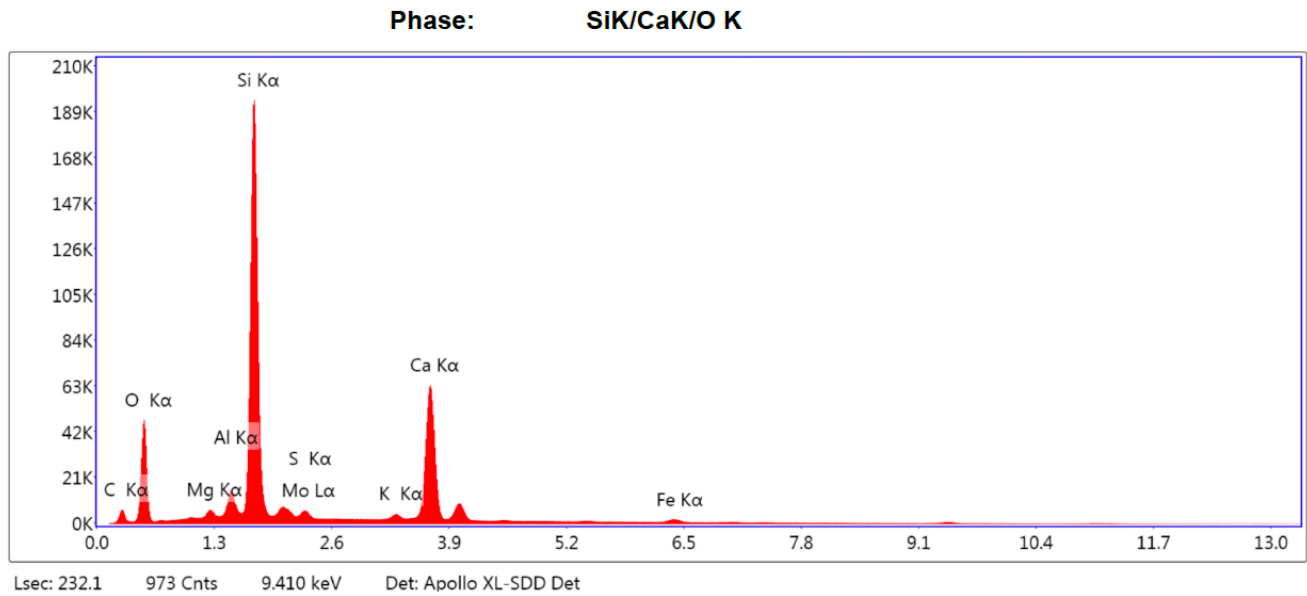
Element	Weight %	Atomic %	Net Int.
C K	4.25	8.46	102.10
O K	27.52	41.11	1478.20
MgK	0.94	0.93	170.00
AlK	8.81	7.81	1742.80
SiK	30.57	26.02	6031.50
MoL	1.35	0.34	106.30
S K	0.00	0.00	0.00
K K	4.49	2.74	594.40
CaK	18.81	11.22	2069.40
FeK	3.24	1.39	182.50

Figure 4. 29. Si, Al, O and K dominant phase in cement-shale interface a) SEM EDS elemental spectrum b) quantification results



Element	Weight %	Atomic %	Net Int.
C K	4.60	9.97	238.40
O K	27.10	44.08	1201.60
MgK	1.45	1.55	272.40
AlK	1.41	1.36	298.60
SiK	6.22	5.77	1451.20
MoL	2.28	0.62	243.90
S K	0.00	0.00	0.00
K K	0.47	0.31	84.60
CaK	54.71	35.52	7355.00
FeK	1.76	0.82	114.10

Figure 4. 30. Ca, O, Si and Mg dominant phase in cement-shale interface a) SEM EDS elemental spectrum b) quantification results



Element	Weight %	Atomic %	Net Int.
C K	5.80	11.51	157.30
O K	27.14	40.39	1440.30
MgK	0.27	0.27	52.70
AlK	2.05	1.81	439.60
SiK	33.68	28.56	7570.40
MoL	2.17	0.54	187.30
S K	0.00	0.00	0.00
K K	0.98	0.60	142.60
CaK	26.48	15.73	3174.00
FeK	1.41	0.60	85.60

Figure 4. 31. Si, Ca and O dominant phase in cement-shale interface a) SEM EDS elemental spectrum b) quantification results

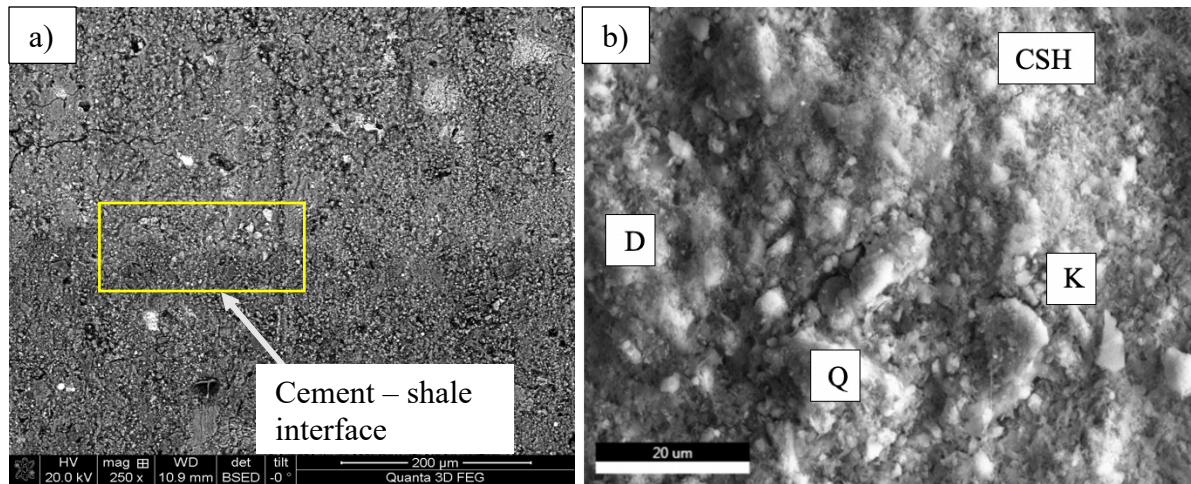


Figure 4. 32. SEM BSE image of cement-shale interface at a) 250x b) 2000x magnification. D is Dolomite. Q is quartz. K is K-Feldspar

4.3. MICROHARNESS

Vickers micro-hardness tests performed were performed on cement-shale, cement-limestone and cement-sandstone, for a total of six set of samples, two of each type. The test load used for determining the hardness values of cement, shale, sandstone and cement-sandstone interface was 500gf while a force of 300gf was used for limestone and cement-limestone. The dwell time for all the hardness tests performed was 15 seconds.

4.3.1. SANDSTONE

The hardness values for the two cement-sandstone samples are listed in table 4.3 and 4.7. For sandstone, the average of four hardness values of the first sample and second sample were: 9.86GPa and 9.90GPa respectively, while for the cement it was 0.82GPa and 0.72GPa. Average hardness values of 2.17GPa and 2.11GPa were acquired for the cement-sandstone interface. The measured indents' lengths for sandstone, cement and interface, used to calculate the hardness values for the cement-sandstone samples are listed in table 4.4, 4.5, 4.6, 4.8, 4.9 and 4.10.

4.3.2. SHALE

For the first cement-shale sample the average of four hardness values for the shale rock was 1.92GPa, while for the cement, average of four hardness values was 0.75GPa (table 4.11). Similarly for the second cement-shale sample the average hardness value of shale was 2.16GPa whereas for cement it was 0.65GPa (table 4.14). Two different loads, 500gf and 300gf, were used to obtain the cement-shale interface hardness values. The interface fractured for both the loads making it impossible to measure the indent diagonals' lengths. From the structural perspective, the primary component that governs the brittle and ductile nature of the rock are the minerals present composing it. The general understanding is that weak or ductile minerals normally have lower brittle characteristic of the rock while strong minerals enhance and promote the brittle nature. (Jarvie et al., 2007; Jin et al., 2014; Rybacki et al., 2016; Wang and Gale, 2009)) classified silicate minerals i.e., quartz and feldspar as strong minerals. In another attempt Du and Radonjic (2019), categorized shale minerals in three divisions, soft grain, medium grain and rigid grains, according to their mechanical strength. Clay minerals were grouped under the solid grains whereas silicates as well as calcite and illite under medium grains. Pyrite, chlorite and other metal oxide and sulfides were termed as rigid grains. The brittleness of the rocks may vary significantly despite having the same percentage of porosities and similar mineral content because of undergoing chemical and or physical diagenetic processes (Heidari et al., 2014; Vajdova et al., 2012; Yilamaz et al., 2009). This is suggestive of the fact that mineral composition, alone, cannot be a factor used to estimate the brittle characteristic and it might be important to also examine the rock minerals texture and environmental conditions. The measurements of indents' diagonals for shale and cement, used to calculate the hardness values for the cement-shale samples are listed in table 4.12, 4.13, 4.15 and 4.16.

4.3.3. LIMESTONE

The Vickers hardness values obtained for the two cement-limestone samples can be seen in table 4.18 and 4.21. Using test load of 300gf for the limestone the average micro-hardness values were 0.87GPa and 0.95Gpa while 0.77GPa and 0.71GPa was noted for cement. The indent diagonals on the interface of cement and limestone were not detected since the indent was too large and irregular in shape. The rock's chemical nature and surface can have an impact on the nature and development of cement hydrate products (Ollivier et al., 1995). Zimbelmann (1985) deduced that at cement-limestone interface an additional adhesion grows. This can be a possible causation of the plastic deformation observed at the interface leading to a large irregular indent. In addition, based on the geochemical interaction at cement limestone interface, Hussin and Poole (2010) determined that limestone promote the cement hydration process and diffusion of elements from both, cement and rock, at the interfacial transition zone. The length of diagonal used in calculation of cement-limestone hardness values are shown in table 4.19, 4.20, 4.22 and 4.23.

The common trend observed in all the cement-rock hardness values was when the average hardness value of a rock for one sample increased the corresponding cement hardness value decreased. For example, when the sandstone average hardness value increased from 9.86GPa in sample 1 to 9.9GPa in sample 2, the corresponding cement value decreased from 0.82GPa in sample 1 to 0.72GPa in sample 2. Likewise for shale, when the rock average hardness value increased from sample 1 to sample 2 i.e., from 1.92GPa to 2.16GPa, respectively, the corresponding cement values in the two samples decreased from 0.75GPa to 0.65GPa. The same relation exists between the average hardness values of the two cement and limestone samples.

Table 4. 3. Cement Sandstone sample 1 Vickers micro-hardness values

Sandstone-Cement						
<u>Surface</u>	<u>HV (H)</u>				<u>Average Hardness (HV)</u>	<u>Average Hardness (GPa)</u>
Rock	940.4	967.9	1016.6	1094.9	1004.95	9.86
Cement	81.4	105.4	75.3	72.9	83.75	0.82
Interface	209.3	246.6	214	191.1	215.25	2.17

Table 4. 4. Cement Sandstone sample 1 Vickers indent dimensions on sandstone and corresponding hardness value

Rock HV (H)		Hardness (MPa)	D1 (um)	D2 (um)
1.	940.4	9.22	29.5	33.3
2.	967.9	9.49	31.6	30.3
3.	1016.6	9.97	30.4	30
4.	1094.9	10.74	26.5	31.7
Avg	1004.95	9.86		

Table 4. 5. Cement Sandstone sample 1 Vickers indent dimensions on cement and corresponding hardness value

Cement HV (H)		Hardness (MPa)	D1 (um)	D2 (um)
1.	81.4	0.79	109.2	104.2
2.	105.4	1.03	102.6	85
3.	75.3	0.73	123.4	98.5
4.	72.9	0.72	112.1	113.5
Avg	83.75	0.82		

Table 4. 6. Cement Sandstone sample 1 Vickers indent dimensions on interface and corresponding hardness value

Interface HV (H)		Hardness (MPa)	D1 (um)	D2 (um)
1.	209.3	2.05	71.7	61.4
2.	246.6	2.41	57.8	64.8
3.	214	2.36	71.5	59.9
4.	191.1	1.87	63.9	75.3
Avg	215.25	2.17		

Table 4. 7. Cement Sandstone sample 2 Vickers micro-hardness values

Sandstone-Cement						
<u>Surface</u>	<u>HV (H)</u>				<u>Average Hardness (HV)</u>	<u>Average Hardness (GPa)</u>
Rock	925.6	990.2	1069	1054.6	1009.85	9.90
Cement	70.5	76.8	66.2	80.4	73.48	0.72
Interface	197.9	274.2	176.4	209.7	214.55	2.11

Table 4. 8. Cement Sandstone sample 2 Vickers indent dimensions on sandstone and corresponding hardness value

Rock HV (H)		Hardness (MPa)	D1 (um)	D2 (um)
1.	925.6	9.08	31.7	31.6
2.	990.2	9.71	30.2	31
3.	1069	10.48	29.8	29.1
4.	1054.6	10.34	30.9	28.4
Avg	1009.85	9.90		

Table 4. 9. Cement Sandstone sample 2 Vickers indent dimensions on cement and corresponding hardness value

Cement HV (H)		Hardness (MPa)	D1 (um)	D2 (um)
1.	70.5	0.69	110.6	122.3
2.	76.8	0.75	113.9	105.8
3.	66.2	0.65	114.2	122.4
4.	80.4	0.79	102.2	102.2
Avg	73.48	0.72		

Table 4. 10. Cement Sandstone sample 2 Vickers indent dimensions on interface and corresponding hardness value

Interface HV (H)		Hardness (MPa)	D1 (um)	D2 (um)
1.	197.9	1.94	59.7	77.2
2.	274.2	2.69	60.2	56.1
3.	176.4	1.73	64.5	80.5
4.	209.7	2.06	60.4	72.6
Avg	214.55	2.11		

Table 4. 11. Cement Shale sample 1 Vickers micro-hardness values

Shale-Cement						
<u>Surface</u>	<u>HV (H)</u>				<u>Average Hardness (HV)</u>	<u>Average Hardness (GPa)</u>
Rock	237	162.4	205	178.4	195.7	1.92
Cement	80.8	71.3	81.1	71.7	76.2	0.75
Interface	Fractures the surface at 300 & 500 gf					

Table 4. 12. Cement Shale sample 1 Vickers indent dimensions on shale and corresponding hardness value

Rock HV (H)		Hardness (MPa)	D1 (um)	D2 (um)
1.	237	2.32	66.4	58.7
2.	162.4	1.593	79.1	72
3.	205	2.01	73.2	61.3
4.	178.4	1.75	73.1	71.1
Avg	195.7	1.92		

Table 4. 13. Cement Shale sample 1 Vickers indent dimensions on cement and corresponding hardness value

Cement HV (H)		Hardness (MPa)	D1 (um)	D2 (um)
1.	80.8	0.79	132.1	82.8
2.	71.3	0.70	133.7	114.4
3.	81.1	0.8	114.2	99.6
4.	71.7	0.70	119.8	107.7
Avg	76.22	0.75		

Table 4. 14. Cement Shale sample 2 Vickers micro-hardness values

Shale-Cement						
<u>Surface</u>	<u>HV (H)</u>				<u>Average Hardness (HV)</u>	<u>Average Hardness (GPa)</u>
Rock	175	261.9	211.2	231.8	220.0	2.16
Cement	68.4	61.8	64.1	72.1	66.6	0.65
Interface	Fractures the surface at 300 & 500 gf					

Table 4. 15. Cement Shale sample 2 Vickers indent dimensions on shale and corresponding hardness value

Rock HV (H)		Hardness (MPa)	D1 (um)	D2 (um)
1.	175	1.72	62.7	82.5
2.	261.9	2.57	60.6	58.4
3.	211.2	2.07	63.1	69.4
4.	231.8	2.27	64	62.5
Avg	220.0	2.16		

Table 4. 16. Cement Shale sample 2 Vickers indent dimensions on cement and corresponding hardness value

Cement HV (H)		Hardness (MPa)	D1 (um)	D2 (um)
1.	68.4	0.67	111.3	120.9
2.	61.8	0.61	113.3	130.7
3.	64.1	0.63	107.9	132.1
4.	72.1	0.71	122	140.6
Avg	66.6	0.65		

Table 4. 17. Cement Limestone sample 1 Vickers micro-hardness values

Limestone-Cement						
Surface	HV (H)				Average Hardness (HV)	Average Hardness (GPa)
Rock (300 gf)	109	85.4	99.2	61.6	88.8	0.87
Cement (500gf)	80.2	79	66.2	87.8	78.3	0.77
Interface	Indent very large and irregular at 300 gf and 500 gf on interface					

Table 4. 18. Cement Limestone sample 1 Vickers indent dimensions on limestone and corresponding hardness value

Rock HV (H)		Hardness (MPa)	D1 (um)	D2 (um)
1.	109	1.07	74.7	68.2
2.	85.4	0.84	84.2	77.2
3.	99.2	0.97	76.1	73.7
4.	61.6	0.60	100	90
Avg	88.8	0.87		

Table 4. 19. Cement Limestone sample 1 Vickers indent dimensions on cement and corresponding hardness value

Cement HV (H)		Hardness (MPa)	D1 (um)	D2 (um)
1.	80.2	0.79	108.9	106.1
2.	79.0	0.77	109.1	107.6
3.	66.2	0.65	114.3	122.4
4.	87.8	0.86	105.4	99.9
Avg	78.3	0.77		

Table 4. 20. Cement Limestone sample 2 Vickers micro-hardness values

Limestone-Cement						
Surface	HV (H)				Average Hardness (HV)	Average Hardness (GPa)
Rock (300 gf)	95.3	87.4	101.7	104.7	97.3	0.95
Cement (500gf)	65.7	79.2	61.5	82.7	72.3	0.71
Interface	Indent very large and irregular at 300 gf and 500 gf on interface					

Table 4. 21. Cement Limestone sample 2 Vickers indent dimensions on limestone and corresponding hardness value

Rock HV (H)		Hardness (MPa)	D1 (um)	D2 (um)
1.	95.3	0.94	103.5	92.7
2.	87.4	0.86	112.0	93.6
3.	101.7	0.99	99.3	92.3
4.	104.7	1.00	135.9	108.1
Avg	97.3	0.95		

Table 4. 22. Cement Limestone sample 2 Vickers indent dimensions on cement and corresponding hardness value

Cement HV (H)		Hardness (MPa)	D1 (um)	D2 (um)
1.	65.7	0.79	113.5	100.9
2.	79.0	0.77	110.5	106.9
3.	61.5	0.65	122.4	114.0
4.	82.7	0.86	110.1	95.7
Avg	72.28	0.71		

4.4. DISCUSSION

The primary goal of this study was to enhance the understanding of high-density cement bonding with three rock types i.e., shale, sandstone and limestone, using different mechanical and analytical techniques. The extensive microstructural and mechanical characterization of the rock-cement interface helped in evaluating the bond strength of high-density cement with different rocks, consequently revealing the compatibility of cement with each rock type. The results of this work, providing information on the nature and adequateness of cement bond with different rocks, can be utilized in plug and abandonment (P&A) and carbon capture and sequestration (CCS) processes.

A good cement-rock bond is required in, both, P&A and CCS, to prevent creation of any leakage path at the rock-cement interface. In P&A the apprehension of the cement bonding with subsurface formation rock is vital for the improvement of cement performance in plugged and abandoned wells. A weak cement bond with subsurface rock will cause a microannulus at the interface leading to poor zonal isolation and impacts on the environment. Similarly, in geological sequestration of carbon dioxide, poor bonding between cement and rock will result in a compromised seal causing carbon dioxide to leak into upper formations. Therefore, the findings of this study are relevant to, both, P&A of wells and storing carbon dioxide securely in geologic formations, in order to attain zonal isolation by achieving an adequate cement-rock bond.

5. CONCLUSION

The conclusion and observations of this work are:

1. The SCBT mode I fracture toughness calculated using the stress intensity factor was higher for the cured cement-sandstone bi-material, as compared to cement-shale and cement limestone samples. Significant variance was observed in the fracture toughness of the cement-shale samples. The peak load at which cement-limestone sample fractured was lower than the cement-sandstone and fell in the wide range of the cement-shale maximum load values.
2. SEM analysis of pure cement showed that C-S-H was the major phase in cement followed by portlandite, also observed was a fair distribution of iron ettringite. Calcium was the most dominant element, distributed throughout the cement.
3. Mineralogical composition obtained from SEM results for shale revealed higher silicon, aluminum and oxygen content. This indicated a greater number of tectosilicates (quartz, plagioclases and K-feldspar) minerals as compared to clay minerals, identifying shale as a brittle hydrocarbon source rock and not a sealing cap rock.
4. SEM elemental map and phase analysis live map for limestone reported almost 90 percent calcium and oxygen while for sandstone over 50 percent of the composition contained silicon and oxygen. The higher number of calcium and oxygen implied calcite majority in limestone. Sandstone, apart from silicon rich minerals, also included rigid grains such as pyrite.
5. The cement-rock boundary was clearly identified in SEM BSE images at 2000x magnification, for cement-sandstone and cement-limestone samples due to the several factors which include, difference in grain size in the two bonded materials, degree of grains

packing and the difference in minerals morphology of the two composites. The cement-shale interface was indistinguishable at lower SEM BSE image resolutions. Amongst the three rocks, shale resembled cement the most in terms of, the grains arrangement and network distribution, porosity and microstructure of the material.

6. The hardness values of sandstone were the largest amongst the three rocks while that of limestone were the smallest. The most difference in the hardness values of the three rocks with the cement was of sandstone whereas limestone and cement had the least difference in the hardness values. The cement-shale interface fractured at different micro-hardness testing loads. In contrast, the cement-limestone interface was ductile, and the indent produced was very large and of irregular shape.
7. The interdependence of rock and cement hardness was observed. Increased rock hardness from one sample to another showed a decrease in cement hardness from one sample to another. This trend was observed in all three bi-material samples i.e., cement-sandstone, cement-shale and cement-limestone.
8. The observed difference in micro-hardness characteristics/behavior between single material (i.e., cement or rock) and bi-material region (cement-rock interface) is demonstrative of the fact that cement interacts with the surrounding rock causing chemical and mineralogical changes at the interface, hence, the difference between hardness results at the cement-rock interface and the single material.
9. Mineral composition, alone, is not sufficient to determine the ductile/brittle nature of the rock and other factors e.g., environmental conditions (physical or chemical diagenesis), porosity or voids' percentage, preexisting fractures and minerals' textures also contribute.

10. The interdependence of the microstructural features and the geomechanical and geochemical variations is observed with the combination of micro-hardness testing and SEM/EDS/BSE.

REFERENCES

- Adepehin, E. (2014, March 14). Petrophysical effect of clay heterogeneity on reservoirs properties. <https://www.morebooks.de/store/us/book/petrophysical-effect-of-clay-heterogeneity-on-reservoirs-properties/isbn/978-3-659-52363-2>.
- Ajayi, T., & Gupta, I. (2019). A review of reactive transport modeling in wellbore integrity problems. *Journal of Petroleum Science and Engineering*, 175, 785–803. doi: 10.1016/j.petrol.2018.12.079
- Bagrintseva, K. I. (2015). Carbonate Reservoir Rocks. <https://doi.org/10.1002/9781119084006>
- Bai, B., Elgmati, M., Zhang, H., & Wei, M. (2013). Rock characterization of Fayetteville shale gas plays. *Fuel*, 105, 645–652. <https://doi.org/10.1016/j.fuel.2012.09.043>
- Balendran, R., Pang, H., & Wen, H. (1998). Use of scanning electron microscopy in concrete studies. *Structural Survey*, 16(3), 146–153. doi: 10.1108/02630809810232718
- Bentz, D. P., Feng, X., Haecker, C.-J., & Stutzman, P. E. (2000). Analysis of CCRL proficiency cements 135 and 136 using CEMHYD3D. <https://doi.org/10.6028/nist.ir.6545>
- Bentz, D. P., Hwang, J. T. G., Hagwood, C., Garboczi, E. J., Snyder, K. A., Buenfeld, N., & Scrivener, K. L. (1994). Interfacial Zone Percolation in Concrete: Effects of Interfacial Zone Thickness and Aggregate Shape. *MRS Proceedings*, 370. <https://doi.org/10.1557/proc-370-437>
- Bourg, I. C. (2015). Sealing Shales versus Brittle Shales: A Sharp Threshold in the Material Properties and Energy Technology Uses of Fine-Grained Sedimentary Rocks. *Environmental Science & Technology Letters*, 2(10), 255–259. <https://doi.org/10.1021/acs.estlett.5b00233>
- Broni-Bediako, E. (2016). Oil Well Cement Additives: A Review of the Common Types. *Oil & Gas Research*, 02(02). <https://doi.org/10.4172/2472-0518.1000112>
- Bu, Y., Du, J., Guo, S., Liu, H., & Huang, C. (2016). Properties of oil well cement with high dosage of metakaolin. *Construction and Building Materials*, 112, 39–48. doi: 10.1016/j.conbuildmat.2016.02.173
- Busch, A., Alles, S., Gensterblum, Y., Prinz, D., Dewhurst, D., Raven, M., ... Krooss, B. (2008). Carbon dioxide storage potential of shales. *International Journal of Greenhouse Gas Control*, 2(3), 297–308. <https://doi.org/10.1016/j.ijggc.2008.03.003>
- Carey, J. W., Wigand, M., Chipera, S. J., Woldegabriel, G., Pawar, R., Lichtner, P. C., ... Guthrie, G. D. (2007). Analysis and performance of oil well cement with 30 years of CO₂ exposure from the SACROC Unit, West Texas, USA. *International Journal of Greenhouse Gas Control*, 1(1), 75–85. doi: 10.1016/s1750-5836(06)00004-1

Carragher, P. J., & Fulks, J. (2018). Well Abandonment Solutions Utilizing Bismuth and Thermite. Day 4 Thu, May 03, 2018. <https://doi.org/10.4043/28897-ms>

Carroll, S. A., McNab, W. W., & Torres, S. C. (2011). Experimental Study of Cement - Sandstone/Shale - Brine - CO₂ Interactions. *Geochemical Transactions*, 12(1). doi: 10.1186/1467-4866-12-9

Carroll, S., McNab, W., Torres, S., Singleton, M., & Zhao, P. (2011). Wellbore integrity in carbon sequestration environments: 1. Experimental study of Cement–Sandstone/Shale–Brine–CO₂. *Energy Procedia*, 4, 5186–5194. doi: 10.1016/j.egypro.2011.02.496

Cerasi, & Stroisz. (2015, November 13). Experimental Investigation of Cement to Rock Bonding. <https://www.onepetro.org/download/conference-paper/ARMA-2015-237?id=conference-paper/ARMA-2015-237>

Chalmers, G. R., Bustin, R. M., & Power, I. M. (2012). Characterization of gas shale pore systems by porosimetry, pycnometry, surface area, and field emission scanning electron microscopy/transmission electron microscopy image analyses: Examples from the Barnett, Woodford, Haynesville, Marcellus, and Doig units. *AAPG Bulletin*, 96(6), 1099–1119. <https://doi.org/10.1306/10171111052>

Chapter 14. Sample Preparation for and Examination with The Scanning Electron Microscope. (n.d.). <https://www.fhwa.dot.gov/publications/research/infrastructure/pavements/pccp/04150/chapt14.cfm>

Daniel B. Shaw (2), Charles E. Weav. (1965). The Mineralogical Composition of Shales. *SEPM Journal of Sedimentary Research*, Vol. 35. <https://doi.org/10.1306/74d71221-2b21-11d7-8648000102c1865d>

Diamond, S. (2004). The microstructure of cement paste and concrete—a visual primer. *Cement and Concrete Composites*, 26(8), 919–933. <https://doi.org/10.1016/j.cemconcomp.2004.02.028>

Diamond, S., & Bonen, D. (1993). Microstructure of Hardened Cement Paste-A New Interpretation. *Journal of the American Ceramic Society*, 76(12), 2993–2999. <https://doi.org/10.1111/j.1151-2916.1993.tb06600.x>

Díaz-Pérez, A., Cortés-Monroy, I., & Roegiers, J. C. (2007). The role of water/clay interaction in the shale characterization. *Journal of Petroleum Science and Engineering*, 58(1-2), 83–98. <https://doi.org/10.1016/j.petrol.2006.11.011>

Du, H., & Radonjic, M. (2019, June). The Mechanism of Fracture Initiation in Shale Rocks: Pottsville cap-rock-shale vs. Marcellus unconventional reservoir-shale. https://www.researchgate.net/publication/344122880_The_Mechanism_of_Fracture_Initiation_in_Shale_Rocks_Pottsville_cap-rock-shale_vs_Marcellus_unconventional_reservoir-shale

- Du, H., Radonjic, M., & Olabode, A. O. (2017, June 25). Impact of Clay Mineralogy on Geomechanics of Shale Caprocks. <https://onepetro.org/ARMAUSRMS/proceedings/ARMA17/All-ARMA17/ARMA-2017-0700/124364>.
- Duguid, A., & Scherer, G. W. (2010). Degradation of oilwell cement due to exposure to carbonated brine. *International Journal of Greenhouse Gas Control*, 4(3), 546–560. <https://doi.org/10.1016/j.ijggc.2009.11.001>
- Evangelista, L., & Guedes, M. (2019). Microstructural studies on recycled aggregate concrete. *New Trends in Eco-Efficient and Recycled Concrete*, 425–451. <https://doi.org/10.1016/b978-0-08-102480-5.00014-2>
- Fischer, S., Liebscher, A., De Lucia, M., & Hecht, L. (2013). Reactivity of sandstone and siltstone samples from the Ketzin pilot CO₂ storage site-Laboratory experiments and reactive geochemical modeling. *Environmental Earth Sciences*, 70(8), 3687–3708. <https://doi.org/10.1007/s12665-013-2669-4>
- Gherardi, F., & Audigane, P. (2013). Modeling geochemical reactions in wellbore cement: assessing pre-injection integrity in a site for CO₂ geological storage. *Greenhouse Gases: Science and Technology*, 3(6), 447–474. <https://doi.org/10.1002/ghg.1357>
- Handbook of Clay Science, Volume 5. Handbook of Clay Science, Volume 5 - 2nd Edition. (2013, May 24). <https://www.elsevier.com/books/handbook-of-clay-science/bergaya/978-0-08-099364-5>.
- Hanson, K. F., Dam, T. J. V., Peterson, K. R., & Sutter, L. L. (2003). Effect of Sample Preparation on Chemical Composition and Morphology of Alkali–Silica Reaction Products. *Transportation Research Record: Journal of the Transportation Research Board*, 1834(1), 1–7. doi: 10.3141/1834-01
- Heidari, M., Khanlari, G. R., Torabi-Kaveh, M., Kargarian, S., & Saneie, S. (2013, March 28). Effect of Porosity on Rock Brittleness. *Rock Mechanics and Rock Engineering*. <https://link.springer.com/article/10.1007%2Fs00603-013-0400-0>.
- Hewlett, P. C. (2003). *Lea's Chemistry of Cement and Concrete*. ScienceDirect. <https://www.sciencedirect.com/book/9780750662567/leas-chemistry-of-cement-and-concrete>.
- Hussain, S. A., Demirci, Ş., & Özbayoğlu, G. (1996). Zeta Potential Measurements on Three Clays from Turkey and Effects of Clays on Coal Flotation. *Journal of Colloid and Interface Science*, 184(2), 535–541. <https://doi.org/10.1006/jcis.1996.0649>
- Hussin, A., & Poole, C. (2010). The geochemical features of the interfacial transition zone. *Advances in Cement Research*, 22(1), 21–28. <https://doi.org/10.1680/adcr.2008.22.1.21>

- Jackson, M. L. (1963). An Introduction to Clay Colloid Chemistry. Soil Science Society of America Journal, 27(6), iv-iv. <https://doi.org/10.2136/sssaj1963.03615995002700060002x>
- Jarvie, D. M., Hill, R. J., Ruble, T. E., & Pollastro, R. M. (2007). Unconventional shale-gas systems: The Mississippian Barnett Shale of north-central Texas as one model for thermogenic shale-gas assessment. AAPG Bulletin, 91(4), 475–499. <https://doi.org/10.1306/12190606068>
- Jennings, H. M., Thomas, J. J., Gevrenov, J. S., Constantinides, G., & Ulm, F.-J. (2007). A multi-technique investigation of the nanoporosity of cement paste. Cement and Concrete Research, 37(3), 329–336. <https://doi.org/10.1016/j.cemconres.2006.03.021>
- Jin, X., Shah, S. N., Roegiers, J.-C., & Zhang, B. (2014). Fracability Evaluation in Shale Reservoirs - An Integrated Petrophysics and Geomechanics Approach. All Days. <https://doi.org/10.2118/168589-ms>
- Josh, M., Esteban, L., Delle Piane, C., Sarout, J., Dewhurst, D. N., & Clennell, M. B. (2012). Laboratory characterisation of shale properties. Journal of Petroleum Science and Engineering, 88-89, 107–124. <https://doi.org/10.1016/j.petrol.2012.01.023>
- Jung, H. B., & Um, W. (2013). Experimental study of potential wellbore cement carbonation by various phases of carbon dioxide during geologic carbon sequestration. Applied Geochemistry, 35, 161–172. doi: 10.1016/j.apgeochem.2013.04.007
- Jung, H. B., Jansik, D., & Um, W. (2012). Imaging Wellbore Cement Degradation by Carbon Dioxide under Geologic Sequestration Conditions Using X-ray Computed Microtomography. Environmental Science & Technology, 47(1), 283–289. doi: 10.1021/es3012707
- Jung, H. B., Kabilan, S., Carson, J. P., Kuprat, A. P., Um, W., Martin, P., ... Fernandez, C. A. (2014). Wellbore cement fracture evolution at the cement–basalt caprock interface during geologic carbon sequestration. Applied Geochemistry, 47, 1–16. doi: 10.1016/j.apgeochem.2014.04.010
- Kaiser, M. J. (2017). Rigless well Abandonment remediation in the shallow water U.S. Gulf of Mexico. Journal of Petroleum Science and Engineering, 151, 94–115. <https://doi.org/10.1016/j.petrol.2017.01.004>
- Katende, A., Krishna, S. V. V., & Radonjic, M. (2019). Contamination of Drilling Fluids on Wellbore Plugs. doi: 10.1002/essoar.10501284.1
- Katsube, T. J., Klassen, R. A., Das, Y., Ernst, R., Calvert, T., Cross, G., ... Connell, S. (2003). Prediction and validation of soil electromagnetic characteristics for application in landmine detection. Detection and Remediation Technologies for Mines and Minelike Targets VIII. <https://doi.org/10.1117/12.486983>
- Katz, B. J., Dittmar, E. I., & Ehret, G. E. (2000). A GEOCHEMICAL REVIEW OF CARBONATE SOURCE ROCKS IN ITALY. Journal of Petroleum Geology, 23(4), 399–424.

<https://doi.org/10.1111/j.1747-5457.2000.tb00494.x>

King, H. M. (n.d.). Shale. <https://geology.com/rocks/shale.shtml>.

Labus, M., & Lorek, A. (2015). CO₂-rock Interaction on the Example of Permian Sedimentary Rocks. 77th EAGE Conference and Exhibition 2015. doi: 10.3997/2214-4609.201413369

Labus, M., & Such, P. (2016). Microstructural characteristics of wellbore cement and formation rocks under sequestration conditions. *Journal of Petroleum Science and Engineering*, 138, 77–87. doi: 10.1016/j.petrol.2015.12.010

Labus, M., & Wertz, F. (2017). Identifying geochemical reactions on wellbore cement/caprock interface under sequestration conditions. *Environmental Earth Sciences*, 76(12). doi: 10.1007/s12665-017-6771-x

Ladva, H. K. J., Craster, B., Jones, T. G. J., Goldsmith, G., & Scott, D. (2005). The Cement-to-Formation Interface in Zonal Isolation. *SPE Drilling & Completion*, 20(03), 186–197. <https://doi.org/10.2118/88016-pa>

Lai, J., Wang, G., Ran, Y., & Zhou, Z. (2015). Predictive distribution of high-quality reservoirs of tight gas sandstones by linking diagenesis to depositional facies: Evidence from Xu-2 sandstones in the Penglai area of the central Sichuan basin, China. *Journal of Natural Gas Science and Engineering*, 23, 97–111. <https://doi.org/10.1016/j.jngse.2015.01.026>

Lavrov, A., Todorovic, J., & Torsæter, M. (2016). Impact of Voids on Mechanical Stability of Well Cement. *Energy Procedia*, 86, 401–410. doi: 10.1016/j.egypro.2016.01.041

Liu, J.-yi, Qiu, Z.-song, & Huang, W. (2015). Novel latex particles and aluminum complexes as potential shale stabilizers in water-based drilling fluids. *Journal of Petroleum Science and Engineering*, 135, 433–441. <https://doi.org/10.1016/j.petrol.2015.10.003>

Lorek, A., Labus, M., & Bujok, P. (2016). Wellbore cement degradation in contact zone with formation rock. *Environmental Earth Sciences*, 75(6). doi: 10.1007/s12665-015-5114-z

Lota, J. S. (1993). The hydration of class G oilwell cement (dissertation)

Ma, Y., Zhou, S., Li, J., Li, Y., Chen, K., Zhang, Y., & Fu, D. (2017). Pyrolysis characteristics analysis of Chang-7 oil shale using thermal analysis and pyrolysis-gas chromatograph-mass spectrometry. *Energy Exploration & Exploitation*, 36(5), 1006–1021. <https://doi.org/10.1177/0144598717744066>

Marusin, S. L. (1999, December 28). Sample preparation - the key to SEM studies of failed concrete <https://www.sciencedirect.com/science/article/pii/S095894659500020D>

Morad, S., Al-Aasm, I. S., Nader, F. H., Ceriani, A., Gasparri, M., & Mansurbeg, H. (2012, August). Impact of diagenesis on the spatial and temporal distribution of reservoir quality in the

Jurassic Arab D and C Members, offshore Abu Dhabi oilfield, United Arab Emirates.
https://www.researchgate.net/publication/236016831_Impact_of_diagenesis_on_the_spatial_and_temporal_distribution_of_reservoir_quality_in_the_Jurassic_Arab_D_and_C_Members_offshore_Abu_Dhabi_oilfield_United_Arab_Emirates.

Murray, J. W. (1983). DREVER, J. I. 1982. The geochemistry of natural waters. Prentice-Hall, Inc., Englewood Cliffs, N.J. 388 p. \$31.95. *Limnology and Oceanography*, 28(3), 600–600.
<https://doi.org/10.4319/lo.1983.28.3.0600a>

Nasvi, M. C. M., Rathnaweera, T. D., & Padmanabhan, E. (2016). Geopolymer as well cement and its mechanical integrity under deep down-hole stress conditions: application for carbon capture and storage wells. *Geomechanics and Geophysics for Geo-Energy and Geo-Resources*, 2(4), 245–256. doi: 10.1007/s40948-016-0034-2

Nelson, E. B., Baret, J.-F., & Michaux, M. (1990). Cement Additives and Mechanisms of Action. *Developments in Petroleum Science*. [https://doi.org/10.1016/s0376-7361\(09\)70301-2](https://doi.org/10.1016/s0376-7361(09)70301-2)

Nelson, P. H. (2009). Pore-throat sizes in sandstones, tight sandstones, and shales. *AAPG Bulletin*, 93(3), 329–340. <https://doi.org/10.1306/10240808059>

Nelson, S. A. (2015). Phyllosilicates (Micas, Chlorite, Talc, & Serpentine).
<https://www.tulane.edu/~sanelson/eens211/phyllosilicates.pdf>.

Newbury, D. E., & Ritchie, N. W. M. (2013, April 19). Elemental mapping of microstructures by scanning electron microscopy-energy dispersive X-ray spectrometry (SEM-EDS): extraordinary advances with the silicon drift detector (SDD).
<https://pubs.rsc.org/en/content/articlelanding/2013/ja/c3ja50026h/unauth#!divAbstract>

Nichols, G. (2001, November 28). SELLEY, R. C. 2000. *Applied Sedimentology*, 2nd ed. x + 523 pp. San Diego, San Francisco, New York, Boston, London, Sydney, Tokyo: Academic Press. ISBN 0 12 636375 7.: *Geological Magazine*.
<https://www.cambridge.org/core/journals/geological-magazine/article/selley-r-c-2000-applied-sedimentology-2nd-ed-x-523-pp-san-diego-san-francisco-new-york-boston-london-sydney-tokyo-academic-press-price-us-8250-hard-covers-isbn-0-12-636375-7/242987915DE0510447A4699E1B38E117>.

Odler, I. (1998). Hydration, Setting and Hardening of Portland Cement. *Lea's Chemistry of Cement and Concrete*, 241–297. <https://doi.org/10.1016/b978-075066256-7/50018-7>

Ollivier, J. P., Maso, J. C., & Bourdette, B. (1995). Interfacial transition zone in concrete. *Advanced Cement Based Materials*, 2(1), 30–38. [https://doi.org/10.1016/1065-7355\(95\)90037-3](https://doi.org/10.1016/1065-7355(95)90037-3)

Olphen, H. V., & Fripiat, J. J. (1979). Data handbook for clay materials and other non-metallic minerals: providing those involved in clay research and industrial application with sets of authoritative data describing the physical and chemical properties and mineralogical composition of the available reference materials.

Rybacki, E., Meier, T., & Dresen, G. (2016). What controls the mechanical properties of shale rocks? – Part II: Brittleness. *Journal of Petroleum Science and Engineering*, 144, 39–58. <https://doi.org/10.1016/j.petrol.2016.02.022>

Scrivener, K. L., Crumbie, A. K., & Laugesen, P. (2004). The Interfacial Transition Zone (ITZ) Between Cement Paste and Aggregate in Concrete. *Interface Science*, 12(4), 411–421. <https://doi.org/10.1023/b:ints.0000042339.92990.4c>

Smith, I., & Shu, D. (2013). A Strategic Shift in Well Abandonment Services. *Oil and Gas Facilities*, 2(01), 19–21. <https://doi.org/10.2118/0213-0019-ogf>

Tasong, W. A., Lynsdale, C. J., & Cripps, J. C. (1998). Aggregate-cement paste interface. ii: influence of aggregate physical properties. *Cement and Concrete Research*, 28(10), 1453–1465. [https://doi.org/10.1016/s0008-8846\(98\)00126-4](https://doi.org/10.1016/s0008-8846(98)00126-4)

Thomas, J. J., & Jennings, H. M. (2003). Changes in the size of pores during shrinkage (or expansion) of cement paste and concrete. *Cement and Concrete Research*, 33(11), 1897–1900. [https://doi.org/10.1016/s0008-8846\(03\)00167-4](https://doi.org/10.1016/s0008-8846(03)00167-4)

Tissot, B. P., & Welte, D. H. (1984). In *Petroleum formation and occurrence: a new approach to oil and gas exploration* (pp. 33–61). essay.

Torsæter, M., Todorovic, J., & Lavrov, A. (2015). Structure and debonding at cement–steel and cement–rock interfaces: Effect of geometry and materials. *Construction and Building Materials*, 96, 164–171. doi: 10.1016/j.conbuildmat.2015.08.005

Tournassat, C., Bourg, I. C., Steefel, C. I., & Bergaya, F. (2015). Surface Properties of Clay Minerals. *Natural and Engineered Clay Barriers*, 5–31. <https://doi.org/10.1016/b978-0-08-100027-4.00001-2>

Vajdova, V., Baud, P., Wu, L., & Wong, T.-fong. (2012). Micromechanics of inelastic compaction in two allochemical limestones. *Journal of Structural Geology*, 43, 100–117. <https://doi.org/10.1016/j.jsg.2012.07.006>

Vielstädte, L., Karstens, J., Haeckel, M., Schmidt, M., Linke, P., Reimann, S., ... Wallmann, K. (2015). Quantification of methane emissions at abandoned gas wells in the Central North Sea. *Marine and Petroleum Geology*, 68, 848–860. <https://doi.org/10.1016/j.marpetgeo.2015.07.030>

Vrålstad, T., Saasen, A., Fjær, E., Øia, T., Ytrehus, J. D., & Khalifeh, M. (2019). Plug & abandonment of offshore wells: Ensuring long-term well integrity and cost-efficiency. *Journal of Petroleum Science and Engineering*, 173, 478–491. doi: 10.1016/j.petrol.2018.10.049

Walsh, S. D., Du Frane, W. L., Mason, H. E., & Carroll, S. A. (2013). Permeability of Wellbore-Cement Fractures Following Degradation by Carbonated Brine. *Rock Mechanics and Rock Engineering*, 46(3), 455–464. <https://doi.org/10.1007/s00603-012-0336-9>

Wertz, F., Gherardi, F., Blanc, P., Bader, A.-G., & Fabbri, A. (2013). Cement CO₂-alteration propagation at the well–caprock–reservoir interface and influence of diffusion. *International Journal of Greenhouse Gas Control*, 12, 9–17. doi: 10.1016/j.ijggc.2012.10.019

Williams, S. M., Carlsen, T., Constable, K. C., & Guldahl, A. C. (2009). Identification and Qualification of Shale Annular Barriers Using Wireline Logs During Plug and Abandonment Operations. *All Days*. <https://doi.org/10.2118/119321-ms>

Xu, J., Qiu, Z., Zhao, X., Zhang, Y., Li, G., & Huang, W. (2018, February 21). Application of Nano-Polymer Emulsion for Inhibiting Shale Self-Imbibition in Water-Based Drilling Fluids. <https://aocs.onlinelibrary.wiley.com/doi/full/10.1002/jsde.12019>.

Yilmaz, I. (2009). A new testing method for indirect determination of the unconfined compressive strength of rocks. *International Journal of Rock Mechanics and Mining Sciences*, 46(8), 1349–1357. <https://doi.org/10.1016/j.ijrmms.2009.04.009>

Zhao, L., Wang, S.-Q., Zhao, W.-Q., Luo, M., Wang, C.-G., Cao, H.-L., & He, L. (2016). Combination and distribution of reservoir space in complex carbonate rocks. *Petroleum Science*, 13(3), 450–462. <https://doi.org/10.1007/s12182-016-0117-2>

Zimbelmann, R. (1985). A contribution to the problem of cement-aggregate bond. *Cement and Concrete Research*, 15(5), 801–808. [https://doi.org/10.1016/0008-8846\(85\)90146-2](https://doi.org/10.1016/0008-8846(85)90146-2)

VITA

Zahid Farid received his Bachelor's degree in Petroleum Engineering from Ghulam Ishaq Khan University (GIKI). He was accepted into the Louisiana State University Petroleum Engineering program where he anticipates graduating with his Master's degree in August 2021.